

On Micro Optical Elements for Efficient Light Diffusion

THÈSE N° 5530 (2013)

PRÉSENTÉE LE 25 JANVIER 2013

À LA FACULTÉ DES SCIENCES ET TECHNIQUES DE L'INGÉNIEUR
INSTITUT DE MICROTECHNIQUE
PROGRAMME DOCTORAL EN PHOTONIQUE

ÉCOLE POLYTECHNIQUE FÉDÉRALE DE LAUSANNE

POUR L'OBTENTION DU GRADE DE DOCTEUR ÈS SCIENCES

PAR

Roland Andreas BITTERLI

acceptée sur proposition du jury:

Prof. N. de Rooij, président du jury
Prof. H. P. Herzig, Dr T. Scharf, directeurs de thèse
Dr F.-J. Haug, rapporteur
Dr A. Schilling, rapporteur
Dr R. Voelkel, rapporteur



ÉCOLE POLYTECHNIQUE
FÉDÉRALE DE LAUSANNE

Suisse
2013

To my parents, my wife and our daughter

Abstract

Efficient light management is one of the key issues in modern energy conversion systems, be it to collect optical power or to redistribute light generated by high power light emitters.

This thesis touches mainly on the subject of efficient light redistribution for high power sources by means of refractive and reflective micro optical elements. Refractive micro optical elements have dimensions that are big enough to neglect diffraction phenomena and small enough to be still manufactured by the methods used in micro fabrication, typically above 50 micron for visible light but below or of the order of one millimeter. The advantage of this limitation that could be called the “refraction limit” is that the design and performance predictions can be based on simple methods such as ray tracing or the edge ray principles for non-imaging optics. In contrary to many studies on engineered diffusers we concentrate here on optical surface where the functional is given by concave shapes!

The first part of the thesis treats the development and fabrication of one dimensional small angle diffusers for collimated high power and potentially coherent light sources. The generation of high power laser lines with a uniform intensity distribution is useful for the optimization of laser manufacturing applications such as annealing of amorphous silicon on large surfaces. This is typically needed for the fabrication of TFT's or thin film solar cells.

The one dimensional diffusers discussed in this thesis are based on an array of concave cylindrical microlenses with a typical lens width of 200 μm and a radius of curvature ranging from 300 μm to 1500 μm . In order to avoid diffraction grating effects due to the regular nature of the array a statistical variation of the lens width was introduced.

The proposed fabrication process is based on isotropic etching of fused silica in hydrofluoric acid. The fabrication and design parameters were explored and their influence on the final performance determined. Extensive computer simulations based on ray tracing and diffractive beam propagation were compared with the measured performance of fabricated devices. Design rules based on an analytical model were also developed and verified. The performance under real world conditions were tested with good results for the smoothing of laser lines at the Bayrisches Laserzentrum in Erlangen, Germany.

The subject of the second part are compact large angle transformers and their possible applications. A short introduction to non-imaging optics and its basic design tools are followed by development of the compound parabolic concentrator (CPC) based on work known for thermal solar concentration. This non-imaging light funnel is concentrating light and has the ability to efficiently transform the angle of an incoming bundle of rays into large angles up to the full half sphere. If inverted, the CPC works as a collimator.

The novelty of the approach presented in this thesis lies in the reduced dimensions of the design and the use of the concentrator not as such but rather as an angle transformer with very high efficiency. When the dimensions of the classical solar concentrators are usually of the order of a few 10 cm or more the design developed in this thesis has dimensions of a few mm or less.

Different possible applications for a compact CPC array are discussed such as LED collimation at chip level, fiber coupling with large numerical aperture and improved light management for thin film solar cells.

The fabrication of a prototype of a compact dielectric filled CPC array as a proof of concept is described and first attempts at its characterization are discussed.

Keywords: micro optics, high power laser, beam shaping, micro fabrication, concave microlens array, non imaging optics, ray tracing, compound parabolic concentrator, diffuser, angle transformer

Zusammenfassung

Effizientes Management von Licht ist einer der zentralen Punkte moderner Systeme zur Energieumwandlung, sei es zum sammeln der optischen Leistung oder deren Umverteilung. Diese These behandelt hauptsächlich die effiziente Umverteilung von Licht mit Hilfe von refraktiven und reflektiven mikro-optischen Elementen. Die Dimensionen refraktiver mikro-optischer Elemente sind gross genug um die diffraktiven Effekte vernachlässigen zu können und doch klein genug um noch in den Vorzug der Methoden zur Mikroherstellung zu kommen. Typischerweise sind die Dimensionen bei Verwendung von sichtbarem Licht also über 50 Mikrometer und kleiner als einige Millimeter. Der untere Limit, den man auch als "Brechungsgrenze" bezeichnen könnte, führt dazu, dass der Entwurf und die Vorhersage der optischen Eigenschaften mit den einfachen Mitteln der geometrischen Optik und dem Randstrahlprinzip der nicht-abbildenden Optik vorgenommen werden kann. Im Gegensatz zu vielen Studien zu "engineered diffusers" legen wir hier das Augenmerk auf optische Oberflächen deren Funktionalität durch konkave Formen gegeben ist

Im ersten Teil der These geht es um die Entwicklung und Herstellung eindimensionaler Diffusoren mit kleinem Diffusionswinkel für kollimierte und potentiell kohärente Hochleistungsquellen. Die Verteilung der Intensität in einer homogenen Linie findet ihre Anwendung für die Optimierung von Fabrikationsschritten wie etwa dem Rekrystallisieren von amorphem Silizium mittels Laser bei der Herstellung von TFTs.

Die in dieser These behandelten eindimensionalen Diffusoren basieren auf einem Feld von konkaven, zylindrischen Mikrolinsen mit einer typischen Breite der Linsen von $200\ \mu\text{m}$ und einem Krümmungsradius zwischen $300\ \mu\text{m}$ und $1500\ \mu\text{m}$. Ein statistisch variierende Linsenweite wurde eingeführt um den Gittereffekt aufgrund des regelmässigen Linsenfelds zu vermeiden. Der beschriebene Fabrikationsprozess basiert auf einem isotropischen Ätzverfahren von Quarzglas in Flusssäure. Die Fabrikations- und Designparameter wurden ermittelt und ihr Einfluss auf die finalen Eigenschaften untersucht. Ausführliche Computersimulationen basierend auf Raytracing und diffraktiver Strahlpropagation wurden mit den gemessenen Eigenschaften verglichen. Auf einem analytischen Modell basierende Designregeln wurden ebenfalls entwickelt und überprüft. Die Eigenschaften wurden auch unter realistischen Bedingungen im Bayrischen Laserzentrum Erlangen getestet und bestätigten den gewünschten glättenden Einfluss auf das Intensitätsprofil.

Der zweite Teil dieser These behandelt kompakte Weitwinkelumwandler und ihre möglichen Anwendungen. Auf eine kurze Einführung in das Gebiet der nicht-abbildenden Optik und ihrer grundlegenden Prinzipien und Werkzeuge folgt die Diskussion des Compound Parabolic

Concentrator (zu Deutsch etwa “Konzentrator aus zusammengesetzten Parabola”) wie er von Roland Winston und weiteren Autoren in den 1970er für thermische Solaranwendungen entwickelt und beschrieben wurde. Dieser nicht-abbildende Lichttrichter konzentriert das Licht und hat gleichzeitig die Eigenschaft den Winkel des einfallenden Strahlenbündel effizient aufzuweiten und dies bis zur kompletten Halbkugel. In umgekehrter Richtung funktioniert er auch als Kollimator.

Die Innovation, die in dieser These diskutiert wird, basiert auf den kleinen Dimensionen des Designs und der Verwendung des Konzentrators nicht als solcher sondern als effizienter Winkeltransformator. Während die Dimensionen klassischer Solarkonzentratoren bei der Grössenordnung von einigen zehn Zentimetern oder mehr liegen, ist das kompakte Design, das in dieser These vorgestellt wird nur einige Millimeter gross.

Verschieden Anwendungsmöglichkeiten für ein kompaktes Feld von CPCs werden diskutiert. So etwa die Verwendung als Kollimator auf Chipebene von Hochleistungs LEDs, die Kopplung von divergentem Licht in Wellenleiterbündel oder verbessertes Lichtmanagement photovoltaischer Solarzellen.

Die Herstellung eines Prototypen eines mit Dielektrikum gefüllten kompakten CPC Feldes wird beschrieben und erste Methoden zur Bestimmung der Winkelumformcharakteristik werden diskutiert.

Stichwörter: Mikro Optik, Hochleistungslaser, Strahlformung, Mikrofabrikation, konkave Mikrolinsfelder, nicht-abbildende Optik, Raytracing, Compound Parabolic Concentrator, Diffusor, Winkeltransformator

Contents

Abstract (English/Deutsch)	v
List of figures	xi
List of tables	xiii
I One dimensional small angle diffuser	1
1 Introduction	3
1.1 Figures of merit	4
2 Line pattern generation	5
2.1 Basic concept of one dimensional diffusers and state of the art	5
2.2 Concept for a refractive micro optics one dimensional diffuser	6
3 Simulation	9
3.1 Analytical model	9
3.2 Isotropic etch model for etching of fused silica in hydrofluoric acid	11
3.3 Diffractive beam propagation model	13
3.4 Gaussian Beam Decomposition Algorithm ray tracing	19
3.5 Discussion	21
4 Fabrication	23
4.1 Process flow	23
4.2 Photomask design	25
4.3 Wet etching of fused silica in hydrofluoric acid	27
5 Results	29
5.1 Inspection	29
5.2 Goniophotometer measurements	31
5.3 Transmission efficiency	33
5.4 Summary of the linear diffuser properties	34
5.5 Performance evaluation with an Excimer laser	34
	ix

Contents

6 Conclusion	37
II Compact large angle transformers	39
7 Introduction	41
8 Non imaging optics	43
8.1 Basic design principles	43
8.2 The Compound Parabolic Concentrator	44
8.3 The generalized Etendue or Lagrange invariant and its implications for the use of a CPC as a diffuser	46
8.4 The dielectric filled CPC design and the θ_1/θ_0 converter	51
8.5 The simple cone concentrator	53
9 Applications for a compact CPC array design	55
9.1 LED collimator	56
9.2 Fiber bundle coupler	57
9.3 Micro concentrated solar cells	58
10 Implementation of a compact dielectric CPC array	65
10.1 Concept	65
10.2 Simulation	67
10.3 Fabrication	71
10.4 Characterization and discussion of the result	75
11 Conclusion	79
Appendix	83
A Proc. SPIE 7062, 70620P (2008)	83
B Opt. Express 18, 14251-14261 (2010)	93
Bibliography	114
Acknowledgements	115
List of publications	117
Curriculum Vitae	119

List of Figures

2.1	Truncated ellipse	5
2.2	Light pipe schematics	6
2.3	Schematics of a fly's eye condenser setup.	7
2.4	Linear diffuser	7
2.5	Linear diffuser profile	7
3.1	Analytical diffusion angle estimation	10
3.2	Isotropic etch process	11
3.3	Evolution of the lens profile in the course of the etch duration	12
3.4	Illustration of the diffraction model	13
3.5	Height function of the diffuser	14
3.6	Simulated intensity profile of the gaussian source	15
3.7	Diffraction model normal distribution	16
3.8	Diffraction model, zero order	17
3.9	Deviation from a circular cross section	18
3.10	Illustration of Gaussian parameters and secondary rays used by FRED	19
3.11	FRED simulation normal distribution	21
3.12	FRED simulation uniform distribution	21
4.1	Illustration of the process flow	24
4.2	Photomask design parameters	25
4.3	Etch control structures	28
5.1	Profilometer measurements	29
5.2	Mach-Zehnder interferometer profile measurements	30
5.3	SEM micrograph of a linear diffuser	30
5.4	Schematics of the goniophotometer setup	31
5.5	Goniophotometer profile normal distribution	31
5.6	Goniophotometer measurements of design LinDif 4.2	32
5.7	Schematics of the test setup with an Excimer laser source	35
5.8	Traces in PMMA of linear diffuser	36
7.1	Schematic illustration of an angle transformer	41
7.2	SEM micro graph of micro CPC array	42

List of Figures

8.1	Illustration of an imaging and a non imaging system	44
8.2	String method	44
8.3	CPC concept	45
8.4	Parametric CPC construction	45
8.5	Ray tracing of a CPC with an acceptance angle of 30° and a source with $\pm 20^\circ$	47
8.6	Ray tracing of a CPC with an acceptance angle of 30° and a source with $\pm 30^\circ$. Few single rays are rejected.	47
8.7	Ray tracing of a CPC with an acceptance angle of 30° and a source with $\pm 31^\circ$. A sharp increase in the number of rejected rays can be observed	48
8.8	Ray tracing of a CPC with an acceptance angle of 30° and a source with $\pm 90^\circ$. A great number of rays are rejected.	48
8.9	Patterns of accepted and rejected rays at the entry face of a CPC	50
8.10	Schematic illustration of a dielectric filled CPC	51
8.11	Refractive index as a function of acceptance angle	51
8.12	Angle converter CPC concept	52
8.13	Simple cone concentrator	53
8.14	Simple cone concentrator design method	53
9.2	RXI free form LED collimator.	56
9.3	High power LED	57
9.4	LED collimation: comparison between dome lens, CPC and CPC array	57
9.5	Illustration of a CPC fiber coupler	58
9.6	Two examples of solar cells	59
9.7	Illustration of a PV cell with a compact 2D CPC array	59
9.8	Illustration of a cone micro concentrator array	59
9.9	Illustration of a tapered waveguide concentrator.	60
9.10	The sun elevation angle	61
9.11	Transmission coefficient at a silicon nitride - PDMS interface	62
9.12	Crystalline silicon solar cell and HIT cell.	63
9.13	Microlens concentrated thin film solar cell.	63
10.1	Dispersion relation of PDMS	66
10.2	Illustration of a truncated CPC of length L'	66
10.3	Simulation of the truncation effect on the angular intensity distribution	68
10.4	Transmission coefficient for a PDMS to air interface.	69
10.5	Coupling light from a dielectric CPC to air	69
10.6	Coupling light from a dielectric θ_1/θ_2 converter to air	70
10.7	Process flow for the direct replication in PDMS of a negative master.	71
10.8	Cross section of the diamond turned drill tool and surface roughness	72
10.9	Brass mold and replicated CPC array made of transparent PDMS	72
10.10	Process flow with a positive master	73
10.11	Cross section of a single CPC shaped pin	74
10.12	Optical microscope images of a miniaturized CPC array.	74

10.13	Illustration of the illumination and measurement setup.	75
10.14	Measurement setup for the characterization of the CPC arrays	75
10.15	Visual comparison between an illuminated CPC array and a flat layer of PDMS 76	76
10.16	Image of the illuminated screen	76
10.17	Measured intensity distribution	78

List of Tables

3.1	Simulated FWHM comparison	22
4.1	Mask Parameter LinDif 1.0	26
4.2	Mask Parameter LinDif 2.0	27
4.3	Mask Parameter LinDif 4.2	27
5.1	FWHM - σ	33
5.2	FWHM comparison	33
8.1	Comparison of the simple cone concentrator and the CPC	54
9.1	Concentration ratio and Length for a 2D dielectric CPC	62

Part I

One dimensional small angle diffuser

1 Introduction

Laser lines with a uniform intensity profile have many applications. An example would be the use of a high power excimer laser for amorphous silicon annealing for the fabrication of TFT's [1, 2, 3]. To obtain a maximum in throughput and uniformity it is desirable to have a line with a profile as uniform as possible. A possible concept to generate the necessary flat-top profile uses multi-aperture elements followed by a lens to recombine separated beamlets (fly's eye condenser) [4]. The advantage of this concept is the independence from entrance intensity profile. However, the periodic structure and the overlapping of beamlets produce interference effects especially when highly coherent light is used. Random optical elements that diffuse only in one direction reduce the contrast of the interference pattern [5]. To maintain a good quality and high efficiency of beam shaping losses due to undesired diffusion in large angles have to be minimized. For high power applications it is interesting to have concave structures that avoid the formation of undesired hot spots.

There are different fabrication methods for diffusers proposed in literature. They can be divided into two groups: etching of ground glass to obtain two dimensional diffusers only [6, 7, 8, 9] and "engineered" diffusers that allow also to fabricate one dimensional diffusers [10]. The engineered diffusers are in general based on holographic [11, 12] or photo fabricated [13, 14] structures (e.g. from RPC Photonics).

In this part of the thesis I propose a fabrication method that offers similar degrees of freedom as the engineered diffusers combined with the limited fabrication complexity offered by etching of ground glass. I propose a fabrication process to obtain statistical arrays of concave cylinder micro structures in fused silica that diffuse light only in one direction. For simplicity the concave micro structures are called lenses even though they do not fulfill the requirements for diffraction limited lenses.

1.1 Figures of merit

A short list of the main desired and undesired characteristics of a one dimensional diffuser for collimated sources:

- Small diffusion angle $< 10^\circ$
- No central transmission peak (zero order)
- No transmission losses
- Diffusion only in one direction
- Micro optics compatibility (dimensions, in particular thickness $\lesssim 1$ mm)
- Functionality based on refraction (*refraction limited*)

2 Line pattern generation

2.1 Basic concept of one dimensional diffusers and state of the art

The intuitive answer to the question of how to transform a laser beam into a line shape is to use a cylindrical lens. The fact that the lens is cylindrical makes sure that the laser beam is only extended in one direction. Unfortunately a single cylinder lens will simply stretch the beam profile, so that a circular Gaussian beam profile will simply turn into an elliptic Gaussian beam profile (see Figure 2.1). To increase the uniformity of the line intensity profile it is possible to truncate the Gaussian with an appropriate window [15, 16, 17]. For power critical applications this is not suitable since a lot of the initial power is lost by truncation.

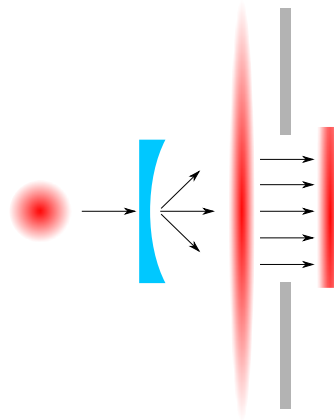


Figure 2.1: Schematics of a line shaping setup with a concave cylinder lens and an aperture window to truncate the Gaussian profile.

One possible way to obtain a desired intensity distribution - e.g. a flat top - by refractive optics is to use a free form lens [18, 19]. For a known source the profile of the lens can be calculated to obtain the desired output profile. Free-form lenses are mainly fabricated by diamond turning and thus miniaturization and arrangements in arrays are difficult to achieve.

Diffractive optical elements (DOE) provide a different micro optics approach to generate

lines or other shapes by mapping the input field into the desired output field [20, 21]. The disadvantage of both, free-form lens and DOE is the direct dependence on the field distribution and the spectra of the source.

Light pipes belong to the beam integrating type of beam shapers. They can also be used for laser beam shaping and specifically for uniform line pattern generation [22]. The light is injected into a pipe with reflective walls and gets mixed and reshaped by multiple reflections (see Figure 2.2). The final pattern is influenced by the shape of the light pipe's cross section and the length of the pipe. Usually the longer the pipe, the more homogeneous is the resulting light field. Chen et al. [22] mention typical lengths of the order of a few centimeters. The most important drawback of this technique is the multiple reflections since they can lead to problems with efficiency and thermal management for high power laser applications.

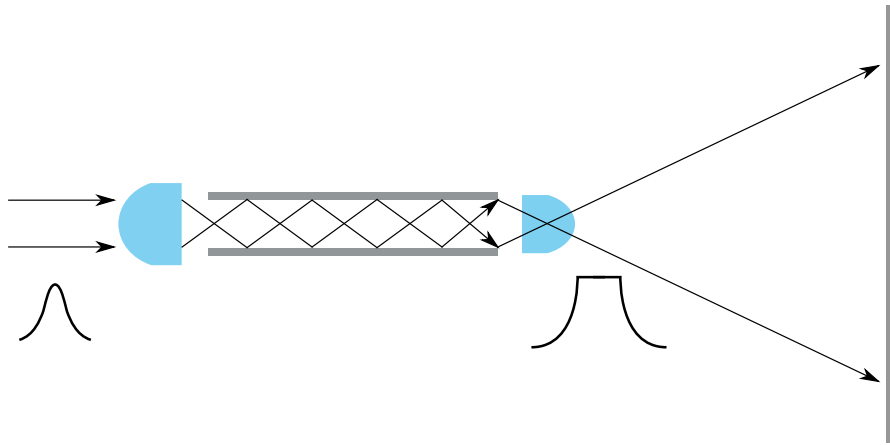


Figure 2.2: Schematics of a light pipe setup with a coupling and relay lens.

Another possibility is to use refractive micro optics. The standard configuration for beam shaping with microlens arrays is the so called fly's eye condenser [23, 24, 25, 26]. For line shaping two cylindrical lens arrays are put one behind the other in a tandem configuration (see Figure 2.3). The distance between the two arrays is equal to the focal distance f_A of the microlenses. An additional condenser lens (Fourier lens) can be used to adjust the imaging area to the requirements [27].

2.2 Concept for a refractive micro optics one dimensional diffuser

One disadvantage of microlens arrays is their regular arrangements. The periodicity together with highly coherent light sources such as lasers lead to strong interference patterns in the intensity profiles. Wippermann et al. [28, 29, 30] propose to use chirped microlens arrays to introduce some randomness in the otherwise regular array.

In this section I will discuss a concept to achieve the same goal as Wippermann obtained with his chirped microlens arrays: a microlens array with a statistical component, in this case the

2.2. Concept for a refractive micro optics one dimensional diffuser

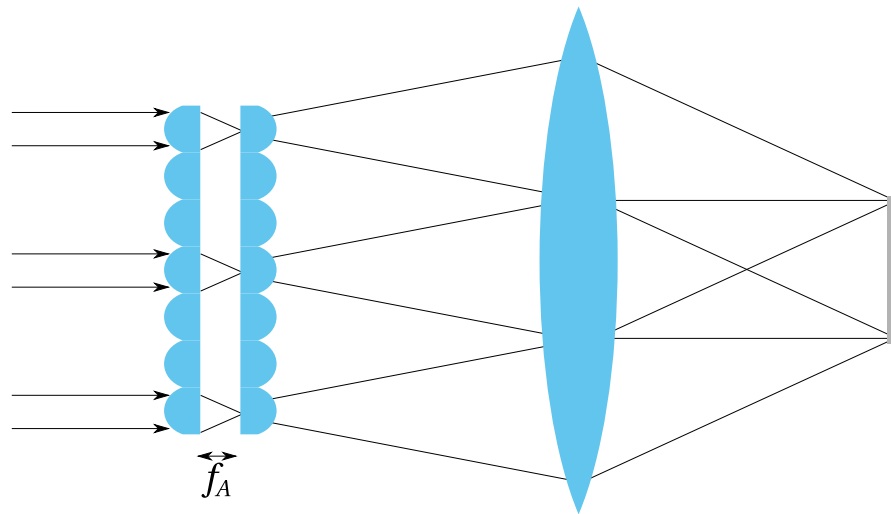


Figure 2.3: Schematics of a fly's eye condenser setup.

distribution of lens width [5, 31, 24]. The width of the lens is distributed following a chosen distribution around a certain mean value but the radius of curvature (ROC) is the same for all lenses in an array. The microlens structures are concave since one of the target applications involves high power lasers in transmission. The concave lens has the advantage that there are no real foci that could lead to undesired hot spots. For the same reason the material of choice is fused silica which has good transmission properties and high damage threshold over a large spectral range from deep UV to NIR.

The fabrication is based on wet etching of fused silica in hydrofluoric acid. For more details on the fabrication process see chapter 4. Figure 2.4 gives an impression of the desired surface shape. It illustrates the the randomness of the lens width while the lens ROC is kept constant.

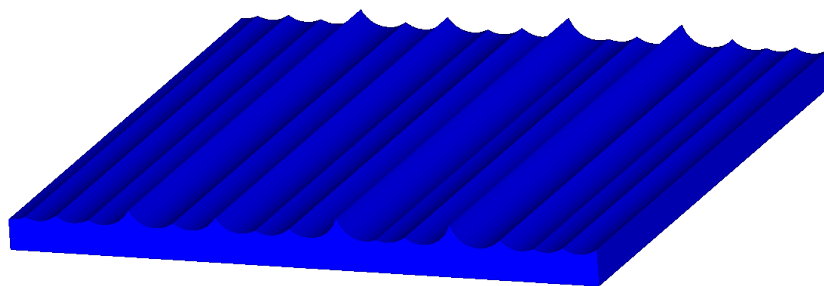


Figure 2.4: Artistic representation of a statistical concave microlens array.



Figure 2.5: Profile of the statistical lens array.

3 Simulation

Computer simulations allow us to predict and optimize the performance of a certain optical system. In this chapter different models for the simulation of a microlens array based diffuser are introduced and discussed. An analytical model for a fast and simple prediction of the optical performances of a diffuser with a given set of parameters is developed first. A model for the etch process of fused silica in hydrofluoric acid (HF) is presented next. The resulting profile of the one dimensional diffuser is then used to obtain the optical properties of the system. The optical properties of the diffusers are also simulated numerically using a purely diffractive model based on the Rayleigh-Sommerfeld diffraction formula and a ray tracing model based on the Gaussian Beam Decomposition Algorithm. The results of the two numerical methods are compared with each other and with the results of the analytical model.

3.1 Analytical model

The average numerical aperture NA of the lens array can be used as a “rule of thumb” prediction of the diffusion full width half maximum (FWHM) angle. Equation (3.1) gives the angular spread (from now on: diffusion angle) as a function of average lens width D , refractive index n and the lens radius of curvature ROC :

$$\theta_{diff} = 2 \arctan \left(\frac{D(n-1)}{2ROC} \right) \quad (3.1)$$

Figure 3.1 shows the diffusion angle according to Equation (3.1) as a function of mean NA, respectively of lens ROC and mean lens width D for fused silica. It shows that the practical range of diffusion angles for this technology is between 0.1° and 20° FWHM.

The lower limit on the ROC and the mean width D is imposed by diffraction. For dimensions too close to the order of the wavelength diffraction is dominating refractive effects. The maximum limit of the ROC is given by the fabrication method. For mechanical stability the

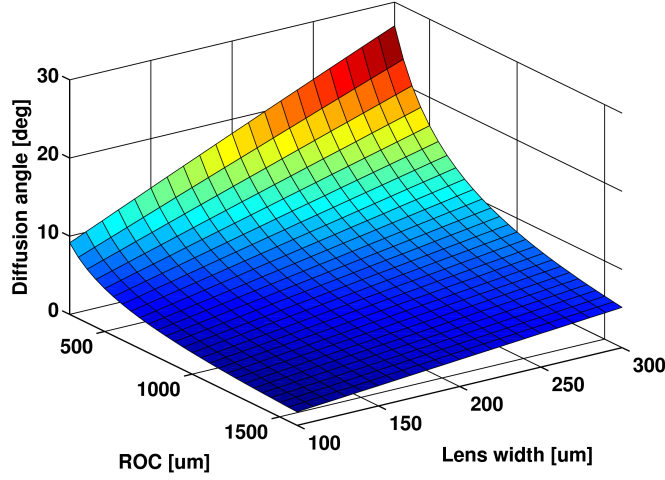


Figure 3.1: Diffusion angle (ROC) estimation using the average NA of the lens array. Refractive index for fused silica $n = 1.48$ at $\lambda = 633$ nm.

original fused silica wafer needs to be at least $500\ \mu\text{m}$ thicker than the desired ROC . Not only the thickness of the substrate is limiting the ROC but also the etch time. Etch speed is about $1\ \mu\text{m}\ \text{min}^{-1}$ resulting in very long etch times for large ROC .

The use of refraction only to predict the diffusion angle is justified for as long as the diffraction angle of a grating with a period equal to the average lens width is small in comparison. For an average lens width of $200\ \mu\text{m}$ and light in the visible range the diffraction angle is less than 0.2°

For coherent light sources the diffused intensity profile is modulated by a speckle pattern. The pattern resembles a high frequency noise signal of small, very bright variations. The average width of the speckles depends in a first approximation only on the size of the source D_s , the wavelength λ and the distance z to the detector[32]. The formula for the speckle diameter s is

$$s = \frac{4\lambda z}{\pi D_s} \quad (3.2)$$

For a laser source with beam diameter $8\ \text{mm}$, wavelength $633\ \text{nm}$ and a propagation distance of $2\ \text{m}$ the expected average speckle size is about $200\ \mu\text{m}$. Speckles are an inherent part of passive or static diffusers [29]. Speckle removal is an interesting and vast field of optics that is beyond the scope of this thesis. The interested reader is referred to Goodman [32] as a reference on speckles or the papers by Masson et al. [33, 34] on speckle reduction with dynamic diffusers.

3.2 Isotropic etch model for etching of fused silica in hydrofluoric acid

Hydrofluoric acid (HF) is etching fused silica isotropically [35]. Etching through an opening in an etch stop mask can be modeled as circles propagating from each point inside of the mask opening into the the material. Figure 3.2 displays the isotropic etching through an etch opening with width g . The superposition of the circles form a flat at the bottom of the structure. The width of that flat part is equivalent to the width of the etch opening g in the mask.

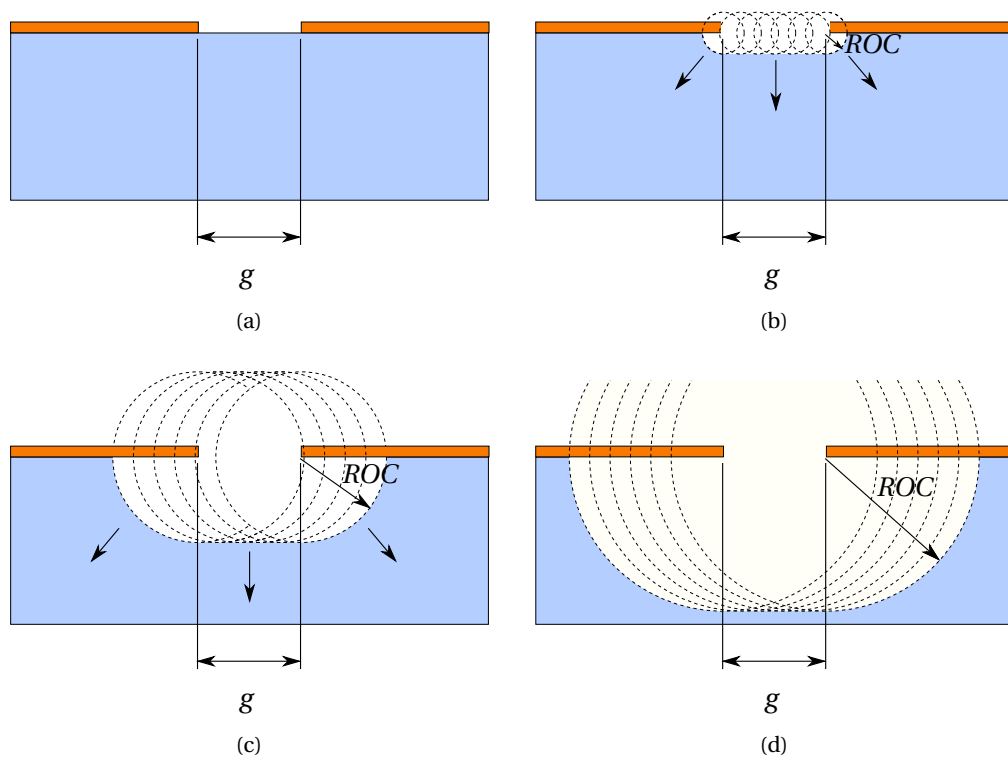


Figure 3.2: Schematic representation of the isotropic etch process through an etch opening in an etch stop mask. The width of the etch opening is g . The isotropic etch process is approximated by concentric circles that propagate from each point in the etch opening.

In order to approximate a circular lens cross section as much as possible the etch opening has to be chosen small compared to the lens' desired radius of curvature (ROC). During the etch process the lenses will start to overlap after a certain time, creating an array of concave microlenses with a 100% fill factor. Figure 3.3 shows how the lens array profile evolves over the etch process duration.

The etch model was implemented in a Matlab script with as parameters the statistical distri-

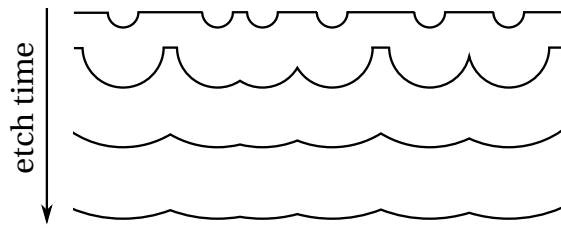


Figure 3.3: Evolution of the lens profile for a statistical array in the course of the etch duration. With time the *ROC* of the lenses increases and the lenses eventually overlap create a lens array of concave lenses with a 100% fill factor.

bution of the mask (mean width, deviation), the width of the etch opening, the total width of the structure and the etch depth respectively the radius of curvature *ROC*. The output of the script is a list of (x/y) coordinates that describe the etched surface structure's profile. This profile data can then be reused by other programs to simulate its optical properties.

3.3 Diffractive beam propagation model

The linear diffuser can be seen as a diffracting, lossless and absorption free aperture that adds a certain phase shift depending on the position where the light wave passes through it. Since the diffuser is one dimensional the model used is also restricted to only one transverse axis x . Figure 3.4 illustrates the principle and the involved parameters

$$U_2(x_2) = \frac{z}{j\lambda} \int_{L_1} U_1(x_1) \frac{e^{ikr}}{r^2} dx_1 \quad (3.3)$$

Using the Rayleigh-Sommerfeld diffraction formula all the phase contributions are summed together and allow to calculate the expected intensity and phase in the detector plane for a given diffuser (Equation (3.3))[36]. r is the free space distance traveled by each wave and is given by

$$r = \sqrt{z^2 + (x_2 - x_1)^2}$$

x_1 is the transverse axis in the source respectively the diffuser plane and x_2 the transverse axis in the detector plane. z is the distance between source and detector plane and k is the wave number given by

$$k = \frac{2\pi}{\lambda}$$

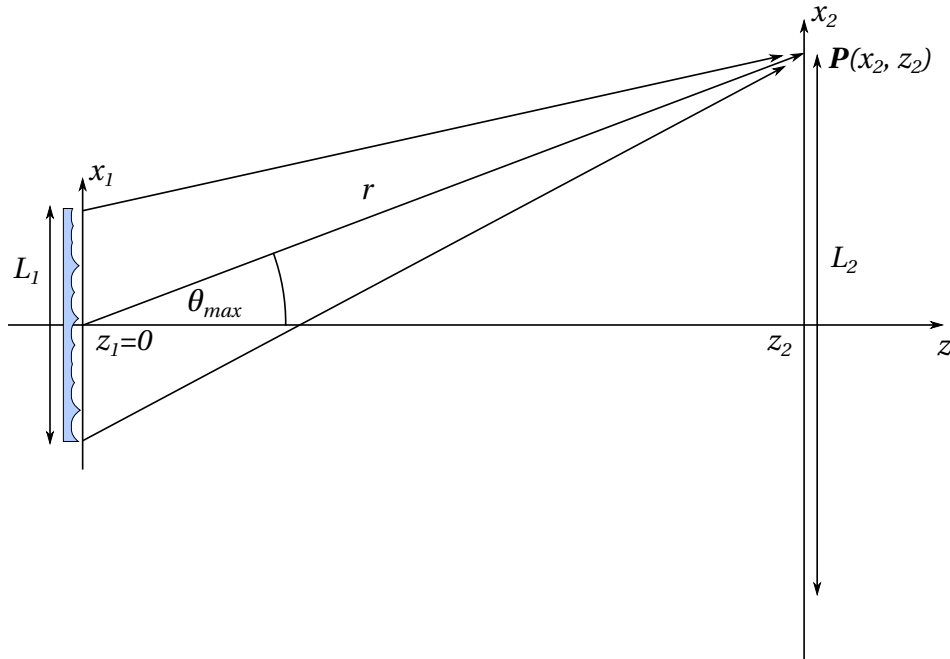


Figure 3.4: Illustration of the diffraction model and the involved parameters.

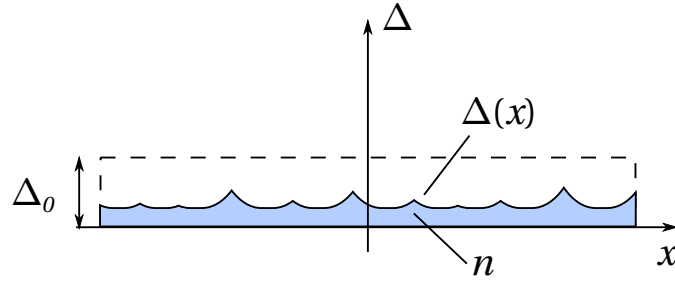


Figure 3.5: Illustration of the diffuser cross section with the parameters for the phase shift according to Equation (3.4)

The phase shift introduced by the diffuser is calculated with the help of a thickness function $\Delta(x_1)$ (Equation (3.4) and Figure 3.5). This is done with a paraxial approximation where only the normal incidence is included [36, 37]. The thickness function that describes the profile of the diffuser is given by the etch process simulation described in Section 3.2. Δ_0 is the initial thickness of the wafer. One finds for the phase delay $\Phi(x_1)$:

$$\Phi(x_1) = kn\Delta(x_1) + k(\Delta_0 - \Delta(x_1)) = k\Delta_0 + k(n-1)\Delta(x_1) \quad (3.4)$$

Equivalently the diffuser may be represented by a multiplicative phase transformation of the form

$$e^{j\Phi(x_1)} = e^{jk\Delta_0} \cdot e^{jk(n-1)\Delta(x_1)} \quad (3.5)$$

The complex field $U_1(x_1)$ immediately behind the diffuser is then related to the complex field $U_0(x_1)$ incident on the diffuser by Equation (3.6).

$$U_1(x_1) = U_0(x_1)e^{j\Phi(x_1)} = U_0(x_1)e^{jk\Delta_0} \cdot e^{jk(n-1)\Delta(x_1)} \quad (3.6)$$

For the numerical implementation in Matlab the detector and source plane need to be sampled. The numerical approximation of the Rayleigh-Sommerfeld integral (Equation (3.3)) is given in Equation (3.7) where s_{max} is the number of samples in the source plane and δx_1 is the distance between the samples. The source plane sampling s influences the minimum geometrical features of the diffuser that are taken into account. The sampling of the detector plane m decides on the resolution of the diffraction pattern.

$$U_2(m) = \frac{z}{j\lambda} \sum_{s=1}^{s_{max}-1} \frac{U_1(s) + U_1(s+1)}{2} \cdot \frac{e^{ikr}}{r^2} \cdot \delta x_1 \quad (3.7)$$

The intensity in the detector plane is finally given as

$$I_2 = U_2 \cdot U_2^* \quad (3.8)$$

Since the goal of the simulation is to compare the theoretical model later on with the measured data it is an obvious choice to use parameters for the simulation that closely resemble the experimental setup described in Section 5.2. The angular resolution of the measurement system is about 0.01° resulting in a detector sampling distance δx_2 for a propagation distance of $z = 2\text{ m}$:

$$\delta x_2 = z \cdot \tan(0.01^\circ) \approx 350\ \mu\text{m}$$

Similarly the detector range L_2 is given by the maximum angle of interest θ_{max}

$$L_2 = 2 \cdot z \cdot \tan(\theta_{max})$$

The source sampling distance is chosen to be

$$\delta x_1 = 0.5\ \mu\text{m}$$

giving a good surface smoothness resolving also the flat at the bottom of the lenslets for an etch opening of $1\ \mu\text{m}$. The width of the diffuser respectively the source L_1 is $8\ \text{mm}$ according to the experimental setup. The experimental source is a HeNe monomode laser that was expanded to a beam diameter of $30\ \text{mm}$ clipped with an aperture to $8\ \text{mm}$. This can be modeled as

$$A(x_1) = e^{-\frac{x_1^2}{w^2}}$$

where w is the beam waist. According to the experimental setup this is half the beam diameter $w = 30/2 = 15\ \text{mm}$. See Figure 3.6 for the propagation simulation of this source without any diffuser. The ripples in the intensity profile are introduced by the clipping aperture.

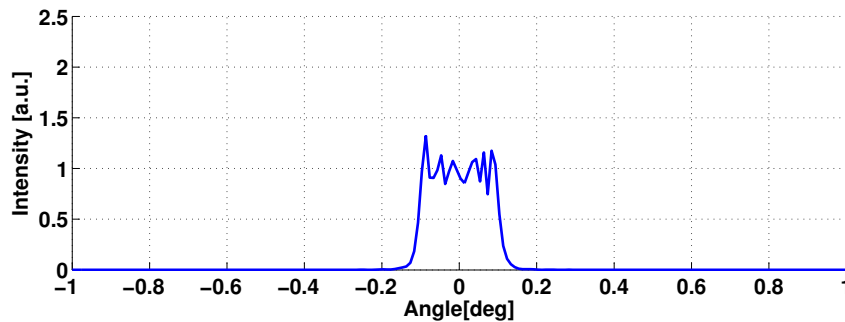


Figure 3.6: Simulated intensity profile of the gaussian source propagated over 2 m. The gauss has a beam waist of 15 mm and is truncated to a beam diameter of 8 mm.

Chapter 3. Simulation

A set of linear diffuser with normal distribution of the lens width and a variation of their width σ ranging from $0\ \mu\text{m}$ to $60\ \mu\text{m}$ was simulated with the diffraction algorithm described above. The average lens width of the simulated diffusers was $D_\mu = 200\ \mu\text{m}$. The etch opening was $g = 1\ \mu\text{m}$ and the radius of curvature $ROC = 1300\ \mu\text{m}$ or $ROC = 300\ \mu\text{m}$. The result of the simulation is displayed in Figure 3.7. Figures 3.7a to 3.7d shows the intensity profile for the configuration with $ROC = 1300\ \mu\text{m}$. Figures 3.7e to 3.7h shows the intensity profile for the configuration with $ROC = 300\ \mu\text{m}$. The simulated intensity data is overlaid with a smoothed curve (running average over 51 samples which corresponds to 0.5°) to simplify the extraction of certain informations from the graph such as the FWHM angle or strong peaks. For a more detailed description of the linear diffuser design parameters see Section 4.2.

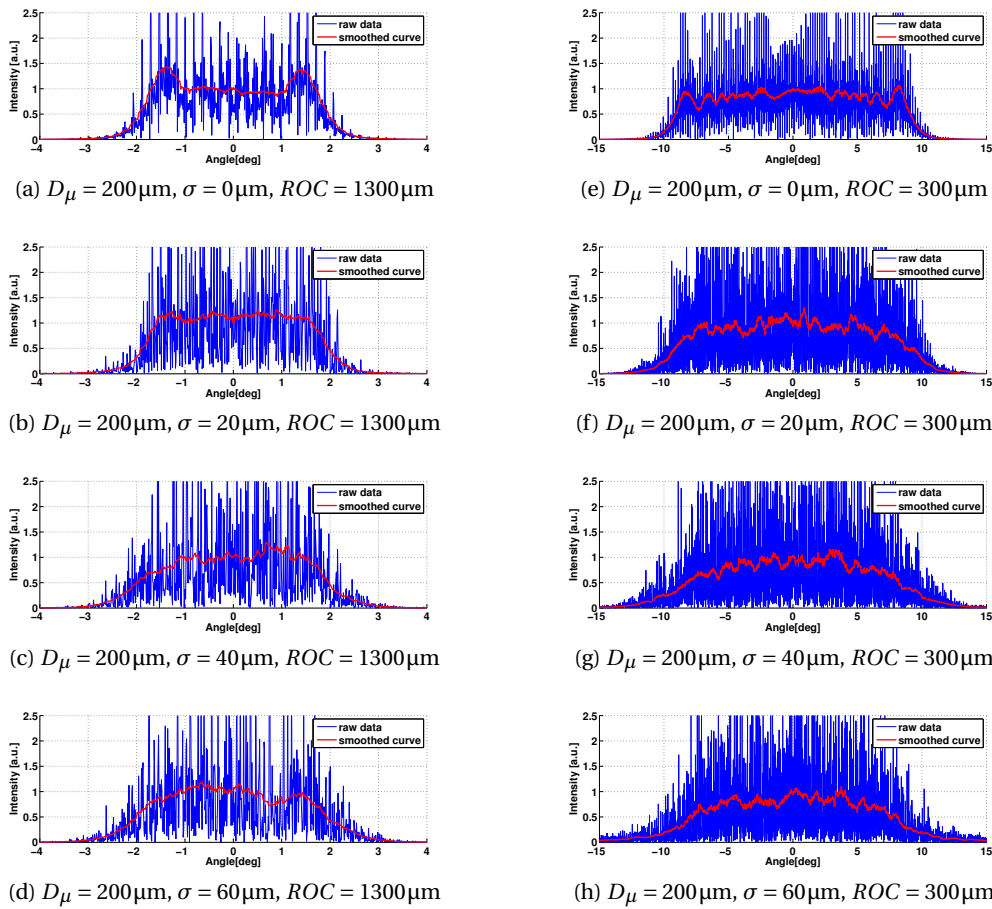


Figure 3.7: Diffraction model of diffusers with normal lens width distribution. The variation of the lens width varies from $\sigma = 0\ \mu\text{m}$ to $\sigma = 60\ \mu\text{m}$. The left column shows the simulation for $ROC = 1300\ \mu\text{m}$. The right column shows the simulation for $ROC = 300\ \mu\text{m}$.

The simulated diffusion FWHM angle is about 4° for the diffuser with a ROC of $1300\ \mu\text{m}$ and a mean lens width of $200\ \mu\text{m}$. For a ROC of $300\ \mu\text{m}$ the FWHM angle is 18° . The regular lens arrays (Figures 3.7a and 3.7e) result in a regular interference pattern modulated on to the diffused light. The periodicity corresponds roughly to the intensity pattern of a grating

3.3. Diffractive beam propagation model

with the period equivalent to the lens width of $200\ \mu\text{m}$. The statistical variation σ of the lens width smears out this regular pattern. An increase in σ flattens also the flanks of diffused intensity profile without noticeably changing the FWHM value. The rapidly varying intensity fluctuations without a regular pattern due to multiple beam interferences are clearly visible. A different statistical distribution (uniform distribution) was also simulated but did not show any remarkable difference in result to the normal distribution shown here.

Figure 3.8 shows the influence of the width of the etch opening g in the etch stop mask (see Section 3.2) on the undesired central specular transmission peak (zero order). The simulated widths are $1\ \mu\text{m}$, $2\ \mu\text{m}$, $5\ \mu\text{m}$ and $10\ \mu\text{m}$. Figures 3.8a to 3.8d show a diffuser with $ROC = 300\ \mu\text{m}$ and Figures 3.8e to 3.8h show a diffuser with $ROC = 1300\ \mu\text{m}$.

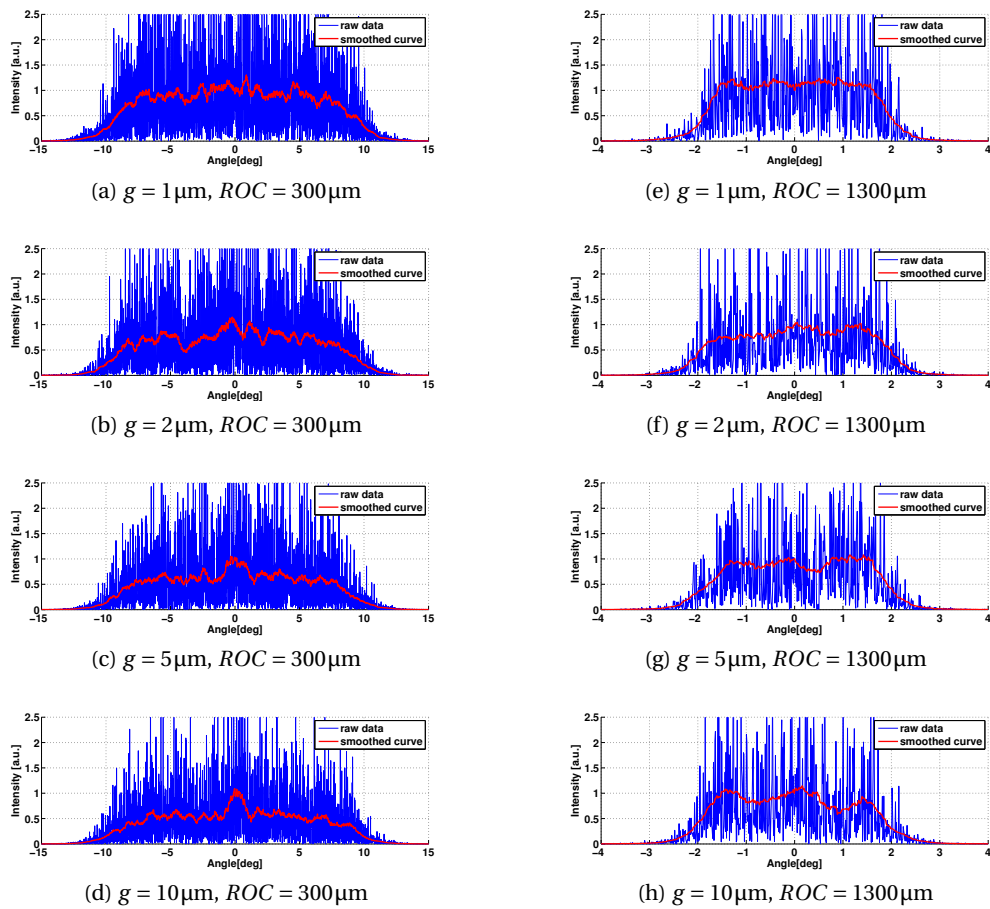


Figure 3.8: Diffraction model of diffusers with normal distribution of the lens width $\sigma = 20\ \mu\text{m}$ and average lens width $D_\mu = 200\ \mu\text{m}$. The width of the etch opening varies from $g = 1\ \mu\text{m}$ to $g = 10\ \mu\text{m}$. The goal of this simulation configuration was to study the influence of the etch opening's dimensions on the central transmission peak.

It is clearly visible that the sensitivity to the width of the etch opening and thus the width of the flat part at the bottom of the lenslet depends on the ROC of the microlenses. The larger the ROC , the smaller is the impact of the etch opening on the performance of the diffuser.

Chapter 3. Simulation

For a diffuser with $ROC = 300\mu\text{m}$ the central transmission peak starts to be visible for etch openings larger than $2\mu\text{m}$ (Figures 3.8c and 3.8d). For a diffuser with $ROC = 1300\mu\text{m}$ the central transmission peak is barely visible for etch openings up to $10\mu\text{m}$ (Figure 3.8h). This observation can be easily explained with the geometrical deviation from the perfect circular cross section introduced by a flat at the bottom which is smaller for circles with a large radius. See Figure 3.9 for a plot of the height deviation h from a perfect circular cross section as a function of ROC and the width of the etch opening g . The graph confirms the observation above that in order to keep the deviation small ($< \lambda/4$) for a small ROC it is important to chose a small etch opening g and that for a large ROC the width of the etch opening g is less crucial.

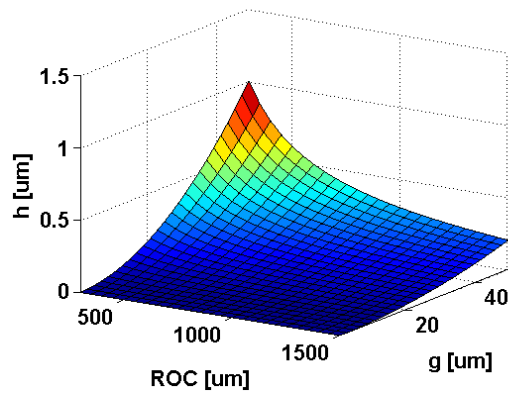


Figure 3.9: Plot of the deviation h from a perfect circular cross section as a function of ROC and the width of the etch opening g .

3.4 Gaussian Beam Decomposition Algorithm ray tracing

The main tool used for optical simulations by ray tracing was FRED from Photon Engineering LLC. FRED allows to trace coherent sources by Gaussian Beam Decomposition Algorithm (GBDA) [38]. This has the advantage that the refractive as well as the diffractive properties of the diffuser can be analyzed with a single tool. The challenge for this method is to find the appropriate parameters for the source.

Coherent sources in FRED are constructed from ray grids and the coherent properties of the source are invoked by assigning a Gaussian beamlet to each ray in the grid. Each ray in the grid serves as a "base ray" that is traced along the axis of each beamlet. By default, FRED assigns eight secondary rays to each base ray and it is the relationship of the secondary and base rays which allow computation of the beam waist and beam divergence at any plane as the beam is propagated.

For illustration purposes, the Figure 3.10 below shows a base ray and two in-plane pairs of secondary rays. An additional set of four secondary rays lie in the orthogonal plane. The waist rays initially trace parallel to the base ray at a distance determined internally by the grid spacing and the overlap factor and corresponding to Overlap times ω_0 . The divergence rays begin coincident with the base rays and trace a trajectory asymptotic to the far-field divergence angle, θ .

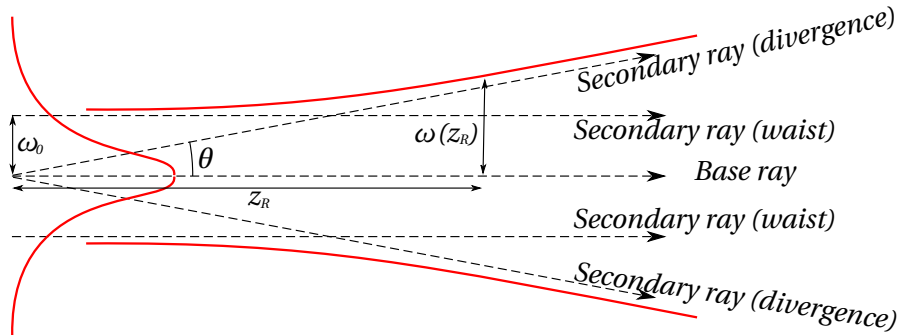


Figure 3.10: Illustration of Gaussian parameters and secondary rays used by FRED. θ is the far field divergence angle of the beam. z_R is the Rayleigh distance at which the surface of the beam cross section has doubled. ω_0 is the minimum beam waist.

The inverse relationship between the beam waist, ω_0 , and the far field divergence, θ (see Figure 3.10 and Equation (3.9)), carries an important implication with regard to sampling of surfaces.

$$\tan(\theta)_{z \gg z_R} = \frac{\omega_0}{z_R} = \frac{\lambda}{\pi \omega_0 n} \quad (3.9)$$

The spatial extent over which the secondary rays intersect any given surface increases as the initial waist ω_0 of the individual Gaussian beamlets decrease. A common mistake in setting up coherent sources is to create a grid of rays so finely spaced that the individual beamlets

Chapter 3. Simulation

become so divergent as to prevent adequate sampling of subsequent optical elements. This has direct consequences when simulating micro optical lens arrays such as the described one dimensional diffuser. A compromise between sampling of the different lens elements and lower limit of initial beam waist and thus divergence of secondary rays has to be found. As an example lets consider a statistical lens array with a mean lens width of $200\mu\text{m}$. The coherent source has a diameter of 8 mm, meaning that an average of 40 lenses are illuminated. A sampling with 2000 rays which corresponds to 50 rays per lens is way too dense, resulting in a rejection of most rays for coherent ray tracing due to secondary rays with too much divergence. A sampling with 40 rays results in no coherent ray errors but the intensity profile is too smooth due to an under sampling of lenses (on average 1 ray per lens). A sampling with 120 rays (3 rays per lens) proved to be a good compromise. With an additional reduction of the secondary ray scale factor from 1 to 0.01 the rejected rays were reduced to a few single rays.

The actual simulation setup was built on a monomode laser source at 633 nm and a beam diameter of 8 mm. Sampling of the source along the x-axis (along the lens array) was 120 rays with a secondary ray factor of 10^{-9} and an initial power of 1000.

The linear diffuser surface was made of an extrusion along the y-axis of a sampled curve generated by the fabrication simulation tool described in Chapter 4 and a flat plane as the back side. Sampling distance between points on the curve was $1\mu\text{m}$ and the width of the chip 10 mm. Note that this is only the geometrical sampling which should not be confused with the optical sampling of the source.

Figure 3.11 shows the result of a simulation of a set of linear diffusers with a normal lens width distribution. The mask parameters correspond to the photomask design LinDif 2.0 which means that the standard deviation is $\sigma = 0.2D_\mu$. For more details on the design parameters see Section 4.2. It is shown later in the discussion of the measured performance of the linear diffusers that the estimation of the diffusion angle is quite good, but the viability of the predicted intensity profile is somewhat limited. It seems to be true especially for diffusers with a large diffusion angle θ , respectively a small radius of curvature *ROC* (see Figure 3.11d) or with a large lens width variation σ .

Figure 3.12 shows the simulated intensity distribution for a set of linear diffusers with a fix *ROC* of $1300\mu\text{m}$, a mean width D_μ of $200\mu\text{m}$ and a uniform with distribution. Each chip has a different width variation σ varying from $0\mu\text{m}$ to $60\mu\text{m}$. An additional smoothed curve is overlaid to simplify the analysis. The smoothed curve is obtained by convolution of the simulated intensity with a 100 sample wide window. This is equivalent to an averaging over 1° . For a regular lens array ($\sigma = 0\mu\text{m}$) the intensity profile shows the expected regular ripples corresponding to a grating with $200\mu\text{m}$. The theoretical angle between peaks is

$$\arcsin\left(\frac{\lambda}{D_\mu}\right) = \arcsin\left(\frac{0.633}{200}\right) = 0.18^\circ \quad (3.10)$$

The introduction of a non-zero variation σ starts to blur the regular pattern (Figure 3.12b).

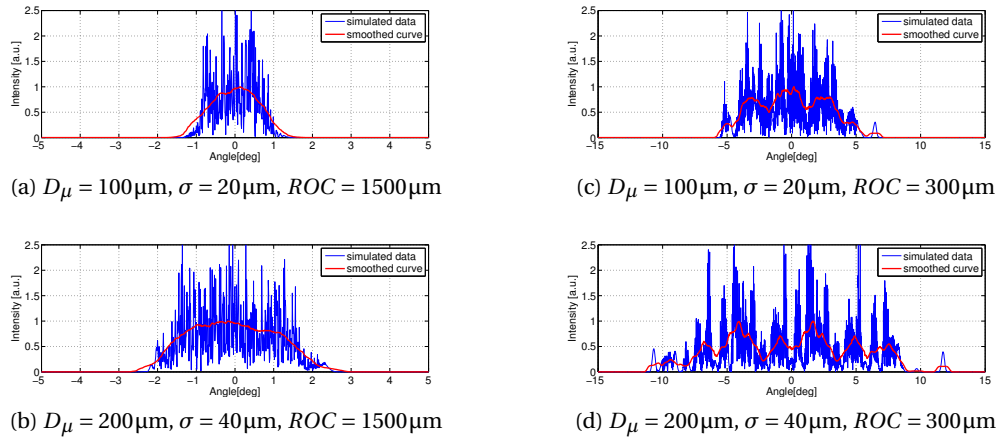


Figure 3.11: FRED simulations of diffusers with a normal distribution of the lens width.

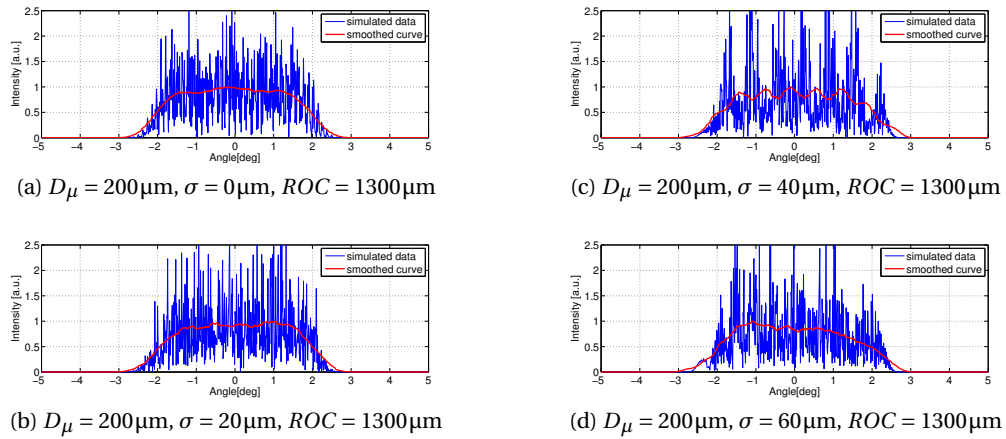


Figure 3.12: FRED simulations of diffusers with a uniform distribution of the lens width and an average lens width $D_\mu = 200\mu\text{m}$. The red curve is a running average over 0.5° . Note that the regular intensity pattern in (c) and (d) are simulation artifacts.

For larger variations (Figures 3.12c and 3.12d) a new regular pattern emerges that does not correspond with the mean periodicity of the array. Comparison with the data from the diffraction model and actual measurements show that this pattern is a simulation artifact only present in the Gaussian Beam Decomposition Algorithm.

3.5 Discussion

A comparison of the simulated FWHM angles for different diffuser configurations (Table 3.1) shows that all three methods presented above yield approximately the same results. The analytical model based on the average lens width is certainly the fastest and most uncomplicated solution as long as the FWHM angle is the main parameter of interest. For the simulation of the angular intensity distribution both Gaussian Beam Decomposition Algorithm and diffraction

Chapter 3. Simulation

theory are useful. The only difference between the two is, that the Gaussian Beam Decomposition Algorithm model is much more calculation intense and needs more time (about 20 minutes vs a few 10 seconds for the diffraction model). The diffraction model could be even more optimized as far as efficiency is concerned by using an FFT algorithm instead of the direct Rayleigh-Sommerfeld integral [39]. This would come at the cost of more complicated sampling considerations and was not implemented for the simulations presented here.

Table 3.1: Comparison of simulated FWHM values for different diffuser configurations and simulation methods.

D_μ [μm]	σ [μm]	ROC [μm]	FWHM Diffraction [$^\circ$]	FWHM FRED [$^\circ$]	FWHM NA [$^\circ$]
100	20	300	8.2	8.0	9.1
100	20	1300	1.8		2.1
200	20	300	18.0	16.2	18.2
200	20	1300	4.0	3.8	4.2

4 Fabrication

There are several different possible ways how to fabricate concave microlens arrays in fused silica. Ruffieux et al [40] used a two step fabrication process where photoresist is spun on an array of melted holes obtained by a photolithography step. The photoresist structures are then transferred into the fused silica or glass by reactive ion etching (RIE). This technology was also used to generate random two dimensional diffusers. The drawback of this technology is the fact that it is not possible to obtain a 100% fill factor. Similar results were obtained by He et al [41] using overexposed and reflowed sol-gel glass. Direct writing of concave structures is described by Lin et al [42] and Du et al [43]. Chen et al. [44] describe a mask less fabrication process based on a femtosecond laser enhanced local wet etching. Lim et al [45] also rely on wet etching but with a laser patterned gold mask layer. Li et al. [46] describe a fabrication process based on controllable dielectrophoretic force in template holes. Although this allows good control over the shape it does not allow for lens arrays with 100% fill factor. Lai et al. [47] demonstrate the fabrication of arbitrary shaped microlens arrays by laser sintering.

The fabrication process in this thesis relies on wet etching of fused silica through a thin film poly-Si etch mask. The decision for this particular fabrication process was based on its relative simplicity, available equipment and compatibility with 100% fill factor design. All the fabrication steps were executed at the clean room facilities of CSEM Comlab and SUSS MicroOptics Neuchâtel.

4.1 Process flow

A graphical description of the process flow is given in Figure 4.1. The poly-Si mask is deposited on the 2 mm thick 4" (100 mm) double side polished fused silica wafer (Lithosil Q1 from Schott). Poly-Si is an ideal hard mask due to its good adhesion to fused silica, negligible etch rate in HF and more important its hydrophobic surface. This reduces the risk of surface pinholes. To further minimize pinholes the layer is deposited in three steps of 200 nm by Low Pressure Chemical Vapor Deposition (LPCVD). A thin layer (500 nm) of diluted photoresist AZ1518 is spun onto the etch mask and patterned by photolithography. The pattern is transferred into

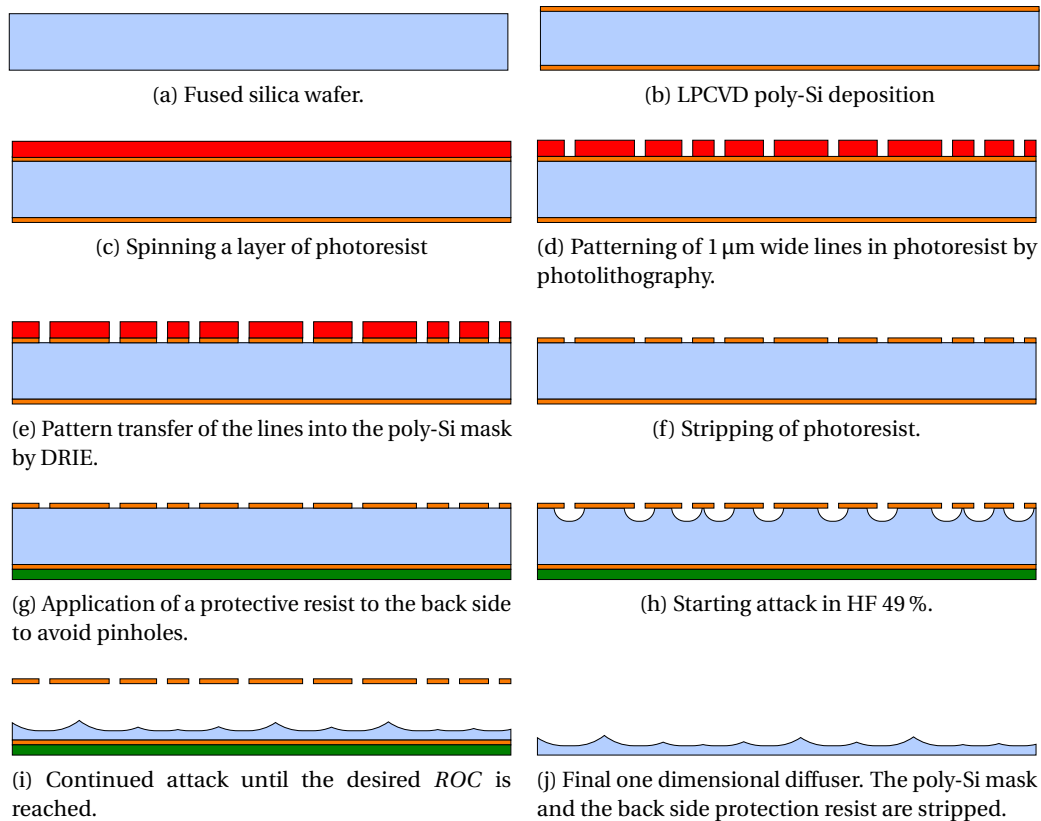


Figure 4.1: Illustration of the process flow for the fabrication of concave statistical microlens arrays in fused silica.

the poly-Si mask by Deep Reactive Ion Etching (DRIE). The remaining photoresist is stripped before the start of the HF etch bath. Pinholes in the back side poly-Si mask remain a problem since the etch times can be very long (up to 24h). This issue is solved by spinning an additional protective layer of ProTEK A-2 HF protection resist from Brewer Science on the back side. The etching of the fused silica is done by unbuffered 49% diluted Hydrofluoric Acid (HF) at room temperature. Once the mask is completely under etched it starts to fall off and little stripes of poly-Si start to float in the etch bath. The wafer is removed from the bath, quickly rinsed with DI water to remove all the remaining poly-Si mask pieces and the etching is continued in a second clean bath of HF 49% until the required *ROC* is reached. After the etch process the wafer is thoroughly rinsed in water to remove all traces of HF. The stripping of the protective resist layer is done according to the procedure recommended by the manufacturer with the special remover. Finally the poly-Si mask is stripped in a KOH bath at 60 °C.

4.2 Photomask design

The generation of the photomask design was done with a Matlab script similar to the one describe above for the etch process simulation. The parameters are width W and height H of the diffuser, mean lens width D_μ , variation of the lens width σ and the width of the etch opening G . Some of the parameters are illustrated in Figure 4.2a. The two different statistical distributions that were used are shown in Figure 4.2b. The continuous line shows a normal distribution around D_μ with standard deviation σ . The probability density function for a certain lens width D is given by Equation (4.1)

$$f(D; D_\mu, \sigma^2) = \frac{1}{\sqrt{2\pi\sigma^2}} e^{-\frac{(D-D_\mu)^2}{2\sigma^2}} \quad (4.1)$$

Maximum and minimum lens width are theoretically not limited and only governed by statistical probabilities. For the normal distribution about 32% of the lenses have a width outside $D_\mu \pm \sigma$ and only about 0.3% have a lens width outside $D_\mu \pm 3\sigma$

The dashed line represents a uniform distribution with $D_{min} = D_\mu - \sigma$ and $D_{max} = D_\mu + \sigma$. The probability density function for a uniform distribution is given by Equation (4.2)

$$f(D; D_{min}, D_{max}) = \begin{cases} \frac{1}{D_{max}-D_{min}} & \text{for } D_{min} \leq D \leq D_{max} \\ 0 & \text{for } D_{min} > D \text{ or } D > D_{max} \end{cases} \quad (4.2)$$

For the uniform distribution the maximum and minimum lens width is given by D_{max} and D_{min} respectively. The Matlab script generates a batch file for the mask program (Expert from Silvaco) that draws the necessary structures.

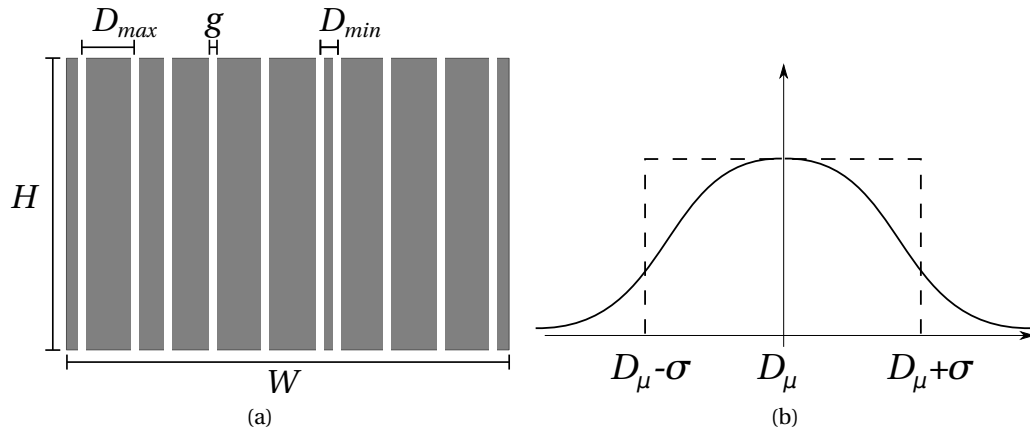


Figure 4.2: Photomask design parameters (a) for the fabrication of a concave lens array with a statistical distribution of the lens width. The grey fields represent the chrome layer. (b) Probability density functions for the lens width D . The continuous line represents a normal distribution and the dashed line a uniform distribution.

Chapter 4. Fabrication

The photomasks were all fabricated by ML&C in chrome on 5" fused silica substrate with a grid of 50 nm and a minimum feature size of 1 μm .

There were three different design iterations. The first one, LinDif 1.0, was a preliminary design to get an idea of the parameter space and the possible effects to observe. The single chip size is rather small with 14 mm \times 14 mm to be able to implement as many variations on one single 4" wafer. Table 4.1 shows all the different configurations for linear diffusers on this design. Notable is in particular the variation of the etch opening with a minimum of 5 μm and a maximum of 20 μm . LinDif 1.0 was implemented without any prior simulation in order to get measurements with real devices as fast as possible to validate later simulations. It showed immediately that the etch opening was chosen too big, resulting in the measurement of too much specular transmission (zero order). This was confirmed later on by simulation. For this reason the etch opening was fixed at 1 μm for the subsequent designs.

In addition to the one dimensional structures a few two dimensional diffusers were also added to the design but for various reasons they were not pursued any further.

Table 4.1: Parameters of the photomask design LinDif 1.0 for linear diffusers, lens width distribution: normal, chip size 14 mm \times 14 mm

Chip code	D_μ [μm]	σ [μm]	g [μm]
A1	50	10	20
A2	50	10	15
A3	50	10	10
A4	50	10	5
B1	100	20	20
B2	100	20	15
B3	100	20	10
B4	100	20	5
C1	150	30	20
C2	150	30	15
C3	150	30	10
C4	150	30	5
D1	200	40	20
D2	200	40	15
D3	200	40	10
D4	200	40	5

For the second design iteration LinDif 2.0 the parameter space was drastically reduced to allow for bigger chip size. For the parameters see Table 4.2. To differentiate between the four parameter sets realized in this design the chips were not labeled with a label but with a marking in the form of a continuous, dashed or dotted line. For later designs this method was dropped and replaced with a normal chip code marking. Based on the experience with LinDif 1.0 and insights gained by simulation the etch opening was kept fix at 1 μm . The distribution of the

4.3. Wet etching of fused silica in hydrofluoric acid

lens width was still a normal distribution with a $\sigma = 0.2D_\mu$ and $\sigma = 0.4D_\mu$.

Table 4.2: Parameters of the photomask design LinDif 2.0, normal lens width distribution, chip size 30 mm × 30 mm

Chip marking	D_μ [μm]	σ [μm]	g [μm]
none	100	20	1
dots	100	40	1
line	200	40	1
dashes	200	80	1

LinDif 3.0 was a mask design made for SUSS MicroOptics. The diffuser was spread over the whole 4" wafer with the parameters $D_\mu = 200\mu\text{m}$, $\sigma = 40\mu\text{m}$ and 1 μm etch opening.

The third design iteration LinDif 4.2 had again slightly smaller chips than LinDif 2.0 to allow for more configurations on a 4" wafer. All the diffusers of this design have the same average lens width $D_\mu = 200\mu\text{m}$. The lens width variation σ ranges from 0 to 160 μm in steps of 20 μm (see Table 4.3). The statistical distribution of lens width follows a uniform distribution as described in Figure 4.2b.

Table 4.3: Parameters of the photo mask design LinDif 4.2, uniform lens width distribution, chip size 20 mm × 20 mm

Chip code	D_μ [μm]	σ [μm]	g [μm]
mu200s0	200	0	1
mu200s20	200	20	1
mu200s40	200	40	1
mu200s60	200	60	1
mu200s80	200	80	1
mu200s100	200	100	1
mu200s120	200	120	1
mu200s140	200	140	1
mu200s160	200	160	1

4.3 Wet etching of fused silica in hydrofluoric acid

Wet etching with unbuffered HF is notoriously irreproducible as far as etch rate goes. It depends on many factors such as temperature, age of the solution, number of wafers already etched etc. [48]. Test patterns on the etch mask were implemented to improve the in situ control over the etch progress (see Figure 4.3). The basic idea is to have structures with a certain width that fall off when a certain etch depth is reached. This allows a visual control over the etch progress to insure that the etch depth and thus the *ROC* can be guaranteed even with

varying etch rates. For the first two design iteration a linear etch control was implemented (Figure 4.3a) based on an array of stripes with gradually increasing width, starting at $5\ \mu\text{m}$ and going up to $500\ \mu\text{m}$ in steps of $5\ \mu\text{m}$ with an etch opening of $1\ \mu\text{m}$ between the stripes. The advantage of this pattern is the close resemblance in topography to the actual linear diffuser pattern and the very fine grained control of $5\ \mu\text{m}$ steps. The disadvantage is that it needs quite a lot of space and visibility by naked eye is not very good. For this reason a simplified control pattern was used for the later design iterations (Figure 4.3b). It is made of four circles with increasing radius ($100\ \mu\text{m}$, $500\ \mu\text{m}$, $1000\ \mu\text{m}$ and $1500\ \mu\text{m}$) and an etch opening around the circles of $1\ \mu\text{m}$. The advantage is that the structures are big enough to be distinguished by naked eye.

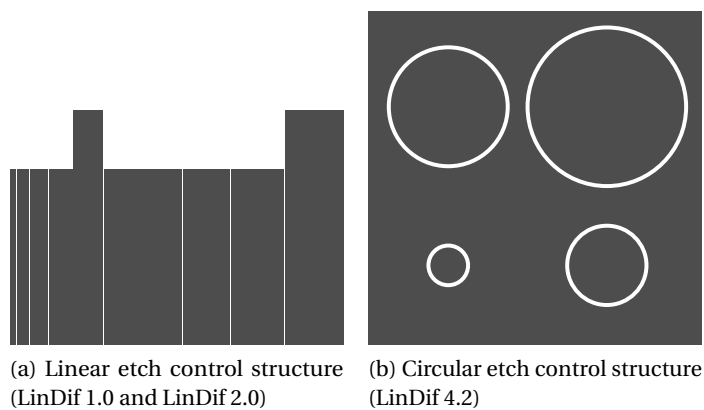


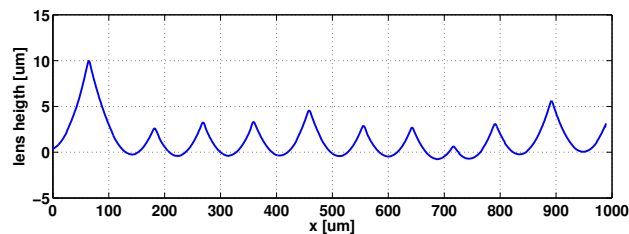
Figure 4.3: Etch control structures that fall off when a certain etch depth is reached.

The measured etch rate for fused silica in HF around $1\ \mu\text{m}\ \text{min}^{-1}$ corresponds to the values found in literature [49, 50]. Agitation of the HF solution shows no noticeable influence on the uniformity of the attack over the wafer or the etch rate. Even without any agitation the etch uniformity over the wafer is very good. The only thing that shows an influence on the uniformity is the orientation of the wafer in the bath. The patterned side of the wafer has to be oriented upwards, otherwise the flow that is induced by the different local concentrations in the etch bath will lead to noticeable local inhomogeneities.

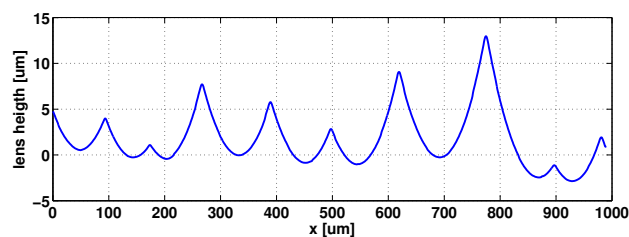
5 Results

5.1 Inspection

The surface profile of the fabricated devices was measured with a stylus alpha-step profilometer (KLA Tencor Alpha-Step IQ Surface Profiler). Figure 5.1 shows surface profiles for two devices with the same average lens width but with different variations. Figure 5.1a shows a standard deviation of $20\ \mu\text{m}$ and Figure 5.1b a standard deviation of $40\ \mu\text{m}$. As is to be expected the profile with the larger standard deviation is more irregular than the one with the smaller standard deviation.



(a)



(b)

Figure 5.1: Surface profiles of one dimensional diffusers with a mean lens width of $100\ \mu\text{m}$ and ROC of $300\ \mu\text{m}$ measured with a profilometer. (a) shows the profile for a device with standard deviation of $20\ \mu\text{m}$ and (b) for a standard deviation of $40\ \mu\text{m}$. (b) shows a clear increase in irregularity compared to (a). Not that the structures are extremely flat. The aspect ratio of the x and y axis is set to about 1:20 for illustrative purposes.

Chapter 5. Results

The surface topography and the optical function of the diffuser were also measured with a Mach-Zehnder interferometer in transmission. The profile measured with the Mach-Zehnder interferometer was also compared to the profile generated by the etch model proposed in Section 3.2. The two profiles are close to identical (Figure 5.2a). The error is plotted in Figure 5.2b. It is less than half the wavelength for a source with $\lambda = 633 \text{ nm}$.

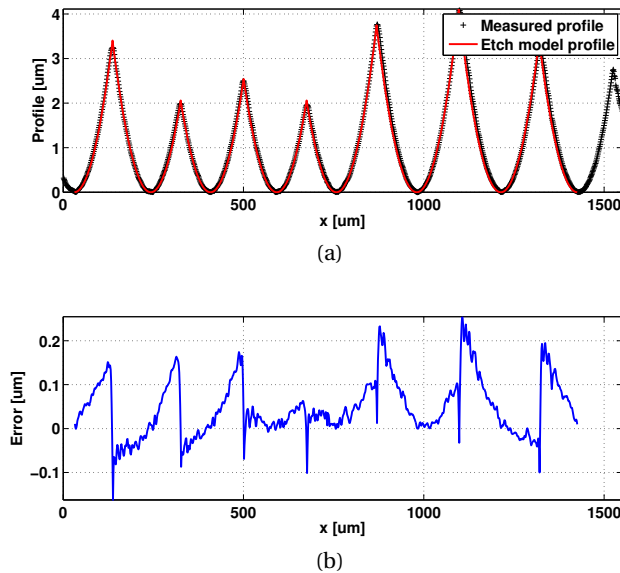


Figure 5.2: Baseline corrected measured profile from Mach-Zehnder interferometry and the simulated profile (a). The difference between the two profiles is plotted in (b).

The manufactured chips were also inspected by scanning electron microscope (SEM). Figure 5.3 shows the SEM micrograph of a linear diffuser with an average lens width of $200 \mu\text{m}$ and a ROC of $1300 \mu\text{m}$. Because of the very low aspect ratio between the lens width and the average lens height it is impossible to make meaningful SEM pictures of a cross sectional cut.

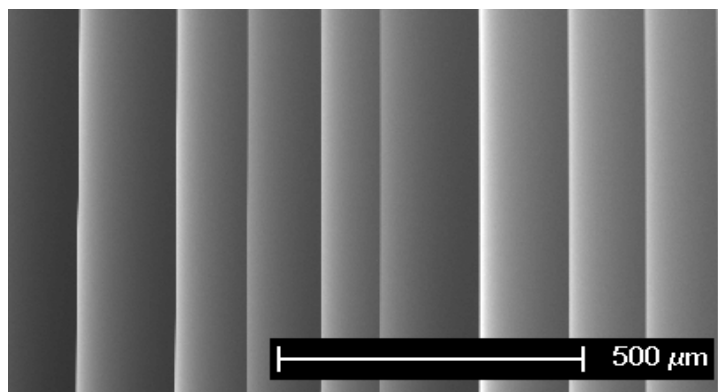


Figure 5.3: SEM micrograph of a linear diffuser with an average lens width of $200 \mu\text{m}$ and a ROC of $1300 \mu\text{m}$

5.2 Goniophotometer measurements

The optical properties were measured with a custom made goniophotometer with a particular high angular resolution of $< 0.01^\circ$. The measurement system is based on a rotating platform with the laser source, the diffuser sample and a photo detector mounted at a distance of 2 m. See Figure 5.4 for a schematic illustration of the goniophotometer setup. Laser and sample are rotated and the detector has a fixed position. This configuration allows for a high angular resolution at a reasonable mechanical complexity compared with the classical setup where the detector is mounted on an arm that is rotating around the sample. A slit aperture of 0.2 mm width is mounted in front of the detector to assure that the detector is not introducing any smoothing of the measured intensity. As a source a monomode HeNe laser at 633 nm with an output power of 2 mW is used. The beam diameter is expanded to about 30 mm and then clipped with a diaphragm to a diameter of 8 mm which means that on average 40 lenses (for 200 μm lens width) respectively 80 lenses (for 100 μm lens width) are illuminated.

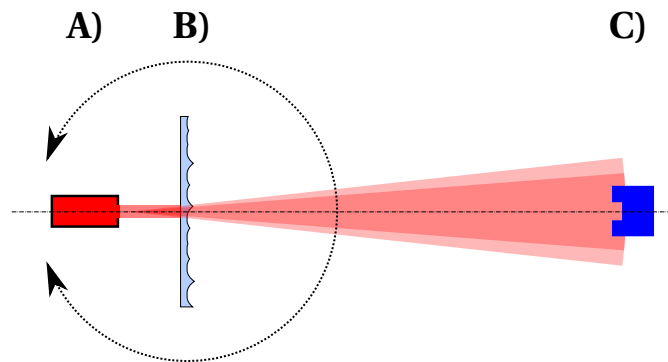


Figure 5.4: Schematics of the goniophotometer setup. The Laser source together with a beam expander (A) and the sample (B) is mounted on a rotating table. The photo detector with an aperture (C) is mounted fix at a distance of 2 m.

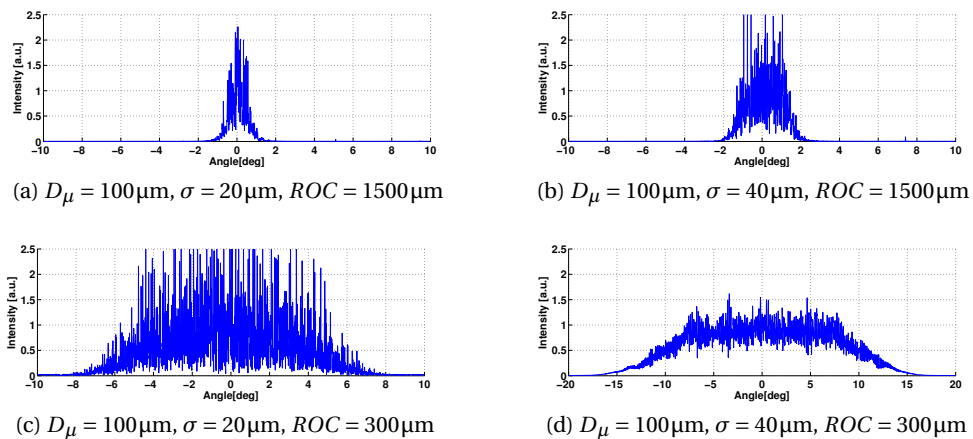


Figure 5.5: Goniophotometer measurements of design LinDif 2.0 (normal distribution). $ROC = 300\mu\text{m}$ and $1500\mu\text{m}$

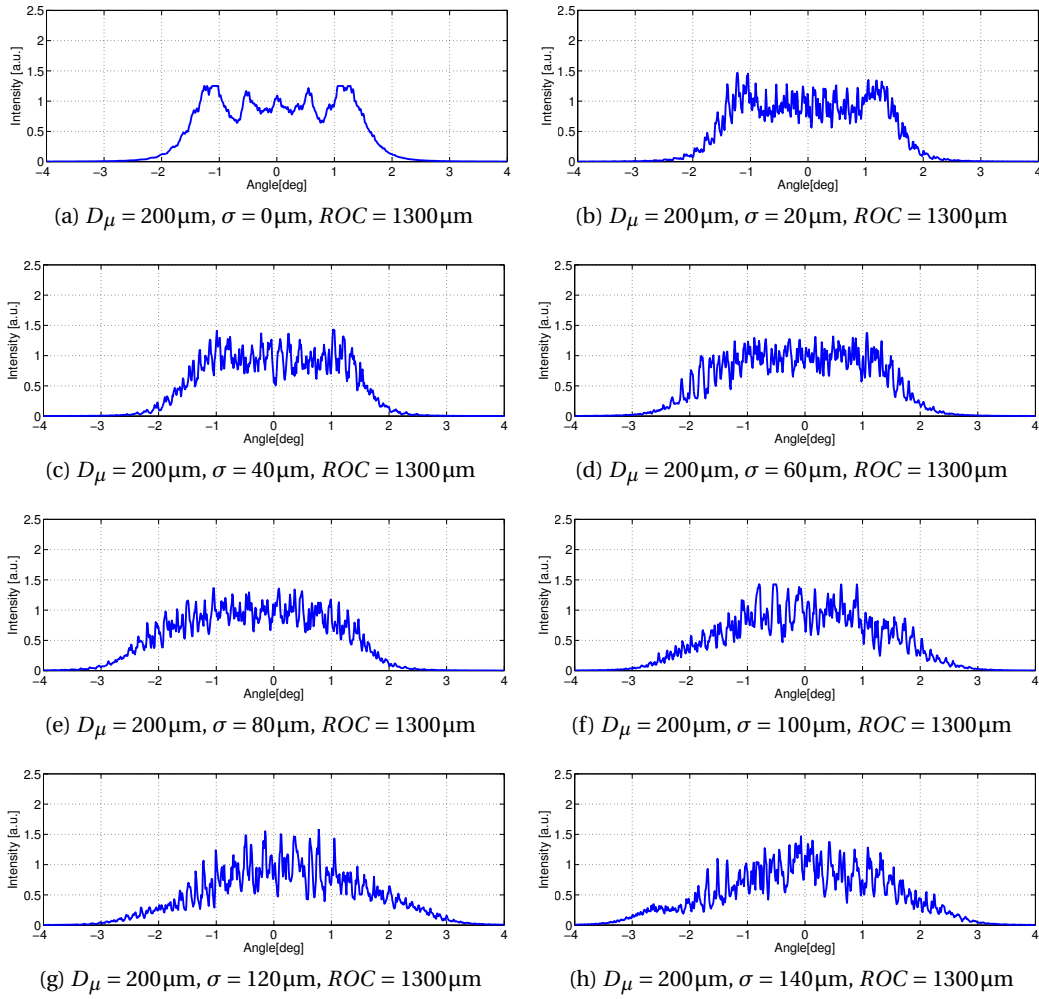


Figure 5.6: Goniophotometer measurements of design LinDif 4.2 (uniform distribution). Different lens width variations σ are measured for a constant $ROC = 1300\mu\text{m}$

Angular intensity distributions are shown in Figure 5.5 and Figure 5.6 for different one dimensional diffusers. Figure 5.5a shows the intensity profile for a sample with a mean lens width of $100\mu\text{m}$, a standard deviation of $20\mu\text{m}$ and a radius of curvature (ROC) of $1500\mu\text{m}$. The FWHM diffusion angle is 1° . For the same diffuser parameter but with a ROC of $300\mu\text{m}$ the FWHM angle is 10° (Figure 5.5c).

The measurements confirm that the FWHM angle depends on the ratio of mean lens width over ROC (Figure 5.5). The steepness of the intensity profile's flanks is influenced by the variation of the lens width. A larger standard deviation leads to a less steep flank (Figure 5.6 and Table 5.1).

In general the FWHM diffusion angles measured with the goniophotometer correspond well with the simulated values from the FRED simulations as well as the values calculated by

Table 5.1: Invariance of the measured FWHM angle as a function of lens width variation σ . $ROC = 1300\mu\text{m}$ and $D_\mu = 200\mu\text{m}$, uniform width distribution (LinDif 4.2, wafer 55)

σ [μm]	20	40	60	80	100	120	140	160
FWHM [$^\circ$]	3.4	3.2	3.6	3.6	3.5	3.3	3.4	3.5

the analytical method proposed in Section 3.1 and the diffraction model. The comparison of measured with simulated values (see Table 5.2) shows that for lenses with a large ROC the simulation results in a slightly larger FWHM diffusion angle whereas for small ROC the simulated FWHM diffusion angle is slightly smaller than the measured value. This could be explained by fabrication effects that are not taken into account for the simulation. For diffusers with a large ROC the sharp ridge where two lenses meet might get slightly rounded off by the long etch time resulting in the somewhat narrower measured FWHM angle compared to simulation. For diffusers with a small ROC the simulation do not take into account the scattering of light at the very sharp ridge between two lenses which would explain the larger measured FWHM angles for such diffusers.

Table 5.2: Comparison of measured FWHM diffusion angle with the predictions from FRED simulation, diffraction model and analytical model based on average lens NA (Section 3.1).

Distrib	D_μ [μm]	σ [μm]	ROC [μm]	gonio [$^\circ$]	FRED [$^\circ$]	Diffr [$^\circ$]	analytic [$^\circ$]
normal	100	20	300	10.0	8.0	8.2	8.8
normal	200	40	300	20.0	16.2	17.4	17.4
normal	200	40	1300		4.0	4.0	4.1
normal	100	20	1500	1.0	1.6	1.5	1.8
normal	200	40	1500	3.0	3.2	3.1	3.5
uniform	200	40	300		17.4	19.0	17.4
uniform	200	40	1300	3.2	4.3	4.0	4.1
uniform	200	40	1500		3.1	3.3	3.5

The goniophotometer measurements with a monomode HeNe laser source showed that the linear diffusers generate a non periodic, rapidly varying far field intensity distribution that was also observed by Wippermann et al. [29] for chirped fly's eye condenser based beam homogenizers or by Wagner et al. for various other diffusers [51]. The variations correspond to the speckles predicted above for the analytical model of a microlens based diffuser (cf. Section 3.1).

5.3 Transmission efficiency

The measured transmission efficiency of roughly 92% regardless of diffusion angle and polarization is equivalent to the expected transmission efficiency of an uncoated fused silica slide

calculated by the Fresnel Equation for reflection in the case of normal incidence [52]:

$$R = \left(\frac{n_1 - n_2}{n_1 + n_2} \right)^2 \quad (5.1)$$

and as a consequences of conservation of energy the transmission is

$$T = 1 - R \quad (5.2)$$

Which results in about 92% for a material with $n = 1.48$ in air. This shows that the diffusing structures do not influence the efficiency. A simple anti-reflection coating for the desired wavelength could increase the efficiency even further. Because there are no hidden structures due to undercut or similar and since the structures are very flat such an anti-reflection layer would be easy to apply and it should also work to nearly 100%.

5.4 Summary of the linear diffuser properties

In summary the properties of the linear diffuser based on statistical concave microlens arrays are the following:

- The FWHM diffusion angle depends on the ratio mean lens width over radius of curvature D_μ / ROC .
- The practical angular range is 0.1° to 20° FWHM.
- The statistical variation of the lens width σ has no influence on the FWHM diffusion angle but determines the steepness of the intensity profile's flanks.
- The intensity profile is modulated by a speckle pattern that depends on the coherence and the dimensions of the source.
- No noticeable central transmission peak (zero order).
- The transmission efficiency is given by the substrate material and the surface coating and is not remarkably influenced by the diffusing structure.

5.5 Performance evaluation with an Excimer laser

The real world homogenizing performance of the fabricated linear diffusers was evaluated with an Excimer laser at the Bayrische Laser Zentrum in Erlangen, Germany. 10 pulses of 28 ns pulse width were applied to a PMMA sample slide. The traces were then inspected with a polarizing optical microscope equipped with Nomarski prism and used in differential interference contrast (Figure 5.8). This gives a good qualitative impression of the homogeneity of the beam profile. The laser was a Coherent-Laser ExciStar M-100 ArF Excimer laser at 193 nm

5.5. Performance evaluation with an Excimer laser

with a mean power of up to 12 W, a pulse energy of 120 mJ and a pulse width of 28 ns. The beam dimensions at the exit were 4 mm × 15 mm and the beam divergence 1 mrad × 3 mrad. The setup was composed of a fly's eye condenser based flat top element (FT5 Microlens Array Nr. 18-00254 from SUSS MicroOptics), the random linear diffuser, a field lens and the PMMA slide which served as target. See Figure 5.7 for a schematic illustration of the setup.

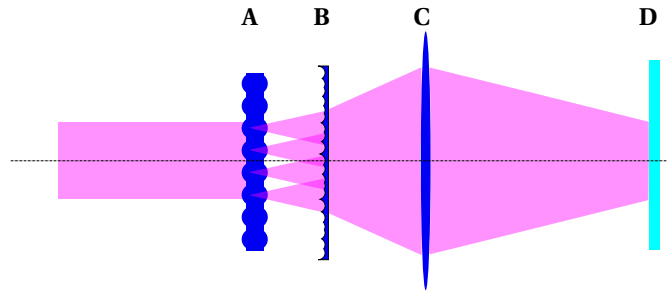


Figure 5.7: Schematics of the test setup with an Excimer laser source. From left to right: raw beam, fly's eye condenser flat top element (A), random linear diffuser (B), field lens (C) and PMMA target slide (D) at the focus of the field lens.

Figure 5.8a shows the trace left in the PMMA sample if only the flat top element is used without any linear diffuser. A regular diffraction pattern generated by this micro optical element is clearly visible. If we add the linear diffuser after the flat top element (Figure 5.8b) we see that everything gets smeared out resulting in a smooth profile. Even after several runs the linear diffuser element did not exhibit any signs of laser induced damage showing the suitability for high power laser applications.

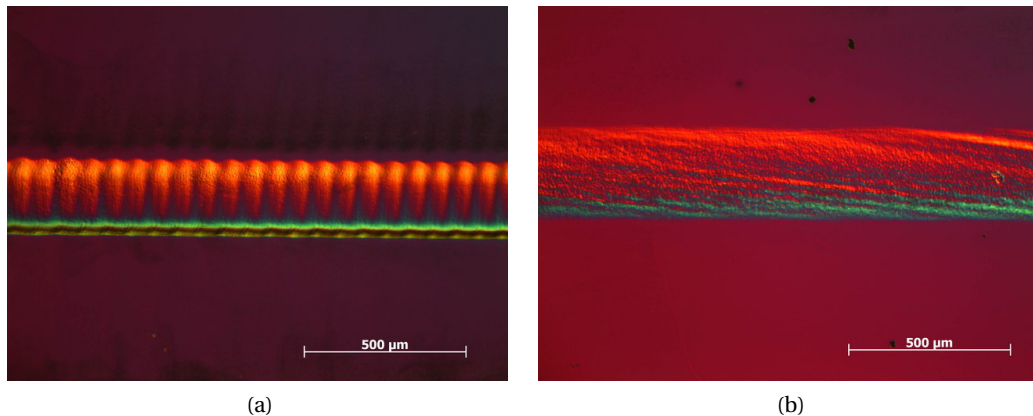


Figure 5.8: Traces left in a PMMA slides by an Excimer laser after passing through different beam shaping elements. (a) Flat top element from SUSS MicroOptics. The periodic intensity peaks are clearly visible. (b) Fly's eye condenser flat top element combined with a linear diffuser with a diffusion angle of 1° FWHM. Compared to (a) the intensity is very smooth without any periodic intensity peaks.

The observed smooth profile when compared with the goniophotometer measurements are

Chapter 5. Results

no big surprise since the coherence length of the monomode HeNe laser that was used as a source for the goniophotometer measurements is considerably longer than the coherence length of an Excimer laser. The Excimer laser is actually a source that is only partially coherent [53]. In order to model such a source correctly it would be necessary to overlay the far field intensity obtained by the diffraction model (Section 3.3) with a convolution of the source intensity profile with the diffuser [54].

6 Conclusion

A true one dimensional diffuser suitable for high power laser beam shaping application has been realized based on concave structures preventing focusing hot spots. The FWHM angle of the diffuser can be selected within the range of 0.1° to 20° by adapting a single fabrication parameter (etch time) which influences the *ROC* of the lens. An analytical model for the estimation of the diffusion angle was proposed and its precision to a few 10th of degrees experimentally verified. A diffraction based model of the linear diffuser showed good agreement with the measured data. Simulation based on Gaussian beam decomposition algorithm was also done, showing that this approach gives somewhat questionable information on the intensity profile but results in comparable prediction of the FWHM diffusion angle. The performance of the fabricated devices inside a complete beam shaping system was verified and it was shown that the use of a linear diffuser can improve the homogeneity of a line generated with a fly's eye beam shaping element. The fabricated diffuser showed absolutely no central transmission peak (zero order) as it is required by many beam homogenizing applications. The measured transmission efficiency is very good. The Fresnel losses for the shallow structures are comparable to an unstructured fused silica slide and could be reduced even further by the use of appropriate anti reflection coatings.

Part II

Compact large angle transformers

7 Introduction

Spreading the angular intensity distribution of diverging sources such as (uncollimated) LEDs or laser diodes can not be done with the technology proposed in the first part of this thesis on small angle diffusers. Since the microlens array based technology allows a maximal diffusion angle of 20° FWHM it is not efficiently spreading the angular spectrum for sources with a divergence of the same order as the maximum diffusion angle or higher. For sources with a large divergence the small angle diffusers only work as homogenizers.

Instead of the microlens based diffuser that is basically made for collimated sources and small angles, an angle transformer of some sort is needed that transforms an input half angle θ_i into an output half angle θ_o . See Figure 7.1 for a schematic illustration of an angular transformer with acceptance half angle θ_i , output angle θ_o and the input and output aperture with diameter $2a$ and $2a'$. The output angle θ_o can be up to $\pi/2$ thus creating a Lambertian source out of a source with less angular extend.



Figure 7.1: Schematic illustration of an angle transformer with acceptance half angle θ_i , output angle θ_o and the input and output aperture with diameter $2a$ and $2a'$.

Such angular transformers exist in the form of non imaging concentrators like the compound conic concentrators (e.g. the compound parabolic concentrator CPC), the light cone concentrator or a combination thereof. They have been invented at the beginning of the second half of the last century almost simultaneously by Baranov, Hinterberger and Winston [55, 56].

Chapter 7. Introduction

Primary applications for those concentrators is the field of thermal solar energy [57, 58].

The novelty of the approach presented in this thesis lies in the compactness of the design and the use of the concentrator not as such but rather as an angle transformer with very high efficiency. When the dimensions of the classical solar concentrators are usually of the order of a few 10 cm the design developed in this thesis has dimensions of a few mm or less. Compound parabolic concentrators (CPC) in the μm range have been realized by Atwater et al. [59] for potential use as LED collimator. Figure 7.2 shows an SEM micro graph of a micro CPC array fabricated by two photon absorption lithography and focused ion beam drilling reported in [59].

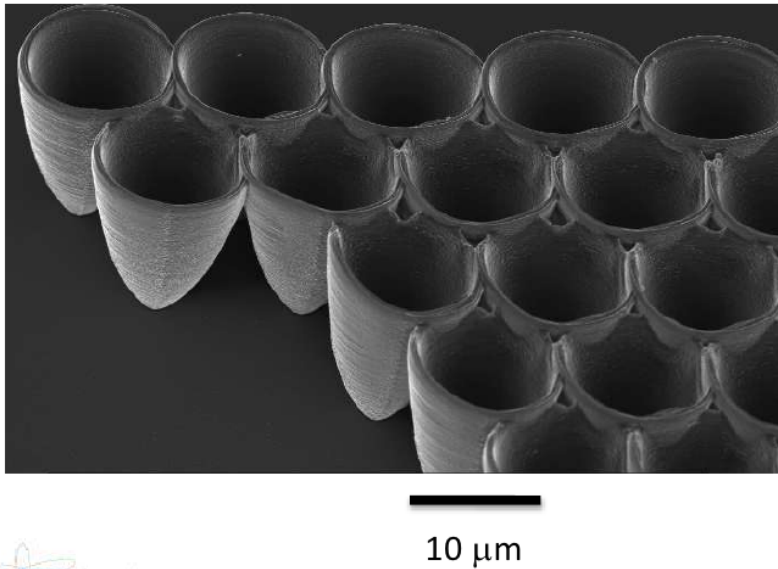


Figure 7.2: SEM micro graph of a densely packed micro photonic CPC array reported by Atwater (<http://e3scenter.org/pubs/102.html>).

For the scope of this thesis the lower limit of the miniaturization is given by the limit when diffraction induces larger angle deviations than refraction. Typically at dimensions of $< 50 \mu\text{m}$ the effects of diffraction start to dominate refraction for light in the visible range and we call this limit the *limit of refraction*.

Chapter 8 is giving an introduction to non imaging optics and its basic design principles such as the edge ray principle or the string method. The design of the compound parabolic concentrator and its variations in the form of the dielectric filled CPC and the θ_i/θ_o transformer are described in more details in Section 8.4.

Chapter 9 treats possible applications for compact CPC arrays other than large angle diffusers for diverging sources. The possible applications discussed in this thesis are LED collimation at chip level, fiber coupler with large NA and improved light management for photovoltaic solar cells. The implementation and fabrication of a compact dielectric CPC array is discussed in Chapter 10.

8 Non imaging optics

8.1 Basic design principles

This section gives a brief introduction to non imaging optics and certain design principles associated with it. Non imaging optics treats a particular field of optics where the goal is not an aberration free image of the source but rather the efficient transfer of light. Non imaging optics and especially collecting optics were extensively treated by Wellford and Winston [60, 61].

The most common method for the design of non imaging optics is known as the edge ray principle [62, 63]. The optics are designed in a way, that the outermost rays of the source are redirected to the edges of the detector. This way all the rays coming from between the edges of the source and having an angle θ smaller than the maximum acceptance angle of the system end up at the receiver. They are not focused on a point and do not form an image of the source. Figure 8.1b illustrates this with a non imaging system that transfers all the rays within a certain acceptance angle θ coming from a source between A and B onto the receiver. For comparison an imaging system is illustrated in Figure 8.1a. The system forms an image of point A and B in A' and B' .

Non imaging concentrator optics are often realized with reflective optics. A simplified design method for a reflective concentrator for a finite source at a finite distance is the so called string method as it is illustrated in Figure 8.2. One end of the string is pinned to the edge S_2 of the source and the other to the edge R_2 of the receiver. The length of the string is $\overline{S_2R_1R_2}$. A pen is tracing the outline of the reflector keeping the string tight. The resulting curve is a piece of an ellipse that has its foci at S_2 and R_2 and starts at R_1 . The same procedure is used for the rays coming from S_1 resulting in the second piece of an ellipse that starts from R_2 (not drawn in Figure 8.2). This is known as a compound elliptic concentrator or CEC. Depending on the application and the source the CEC can be realized as a trough or by rotation around the optical axis.

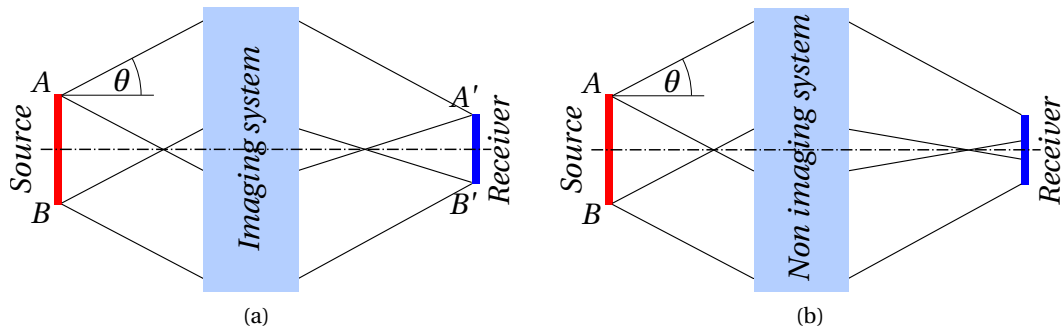


Figure 8.1: Illustration of an imaging system (a) and a non imaging system (b). The edge ray principle states that all rays originating between A and B having a maximum angle θ are transferred to the receiver. Only the imaging system also forms an image of the source at the same time. The additional constraint of the imaging formation limits the range of θ for the imaging system.

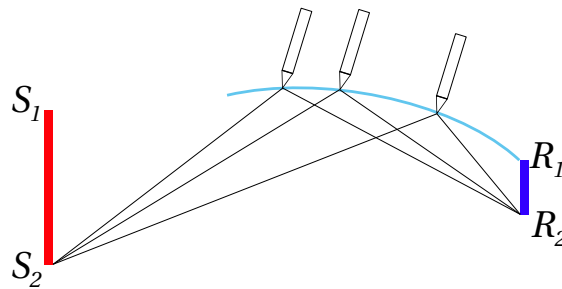


Figure 8.2: Construction of a compound elliptic concentrator CEC according to the string method. Note the undercut that can appear for a CEC at the entry which presents a potential fabrication issue.

8.2 The Compound Parabolic Concentrator

For an infinitely far source the elliptic shape of the CEC in Figure 8.2 turns into a piece of a parabola PR with focus F (see Figure 8.3). The axis of the parabola PA is inclined with respect to the optical axis OA by the input acceptance angle θ_i . This means that all the rays with an angle θ_i with respect to the optical axis are focused on F and all the rays with an angle smaller than θ_i are reflected and pass between R and F . Rays with an angle bigger than θ_i are reflected multiple times and are rejected eventually.

There are different mathematical representations of the CPC curve. The most convenient is probably the parametric representation in a cartesian coordinate system according to [61]. For a graphical illustration see Figure 8.4. The origin of the coordinate system lies at the center of the exit aperture and the z axis lies on the axis of the concentrator. The parameter ϕ is the angle swiped by radius vector r and varies between $2\theta_i$ and $\theta_i + \pi/2$. The parametric function

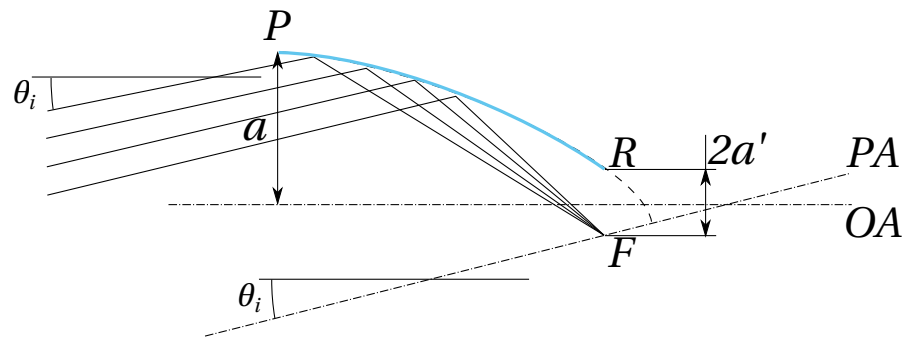


Figure 8.3: Concept of a compound parabolic concentrator CPC.

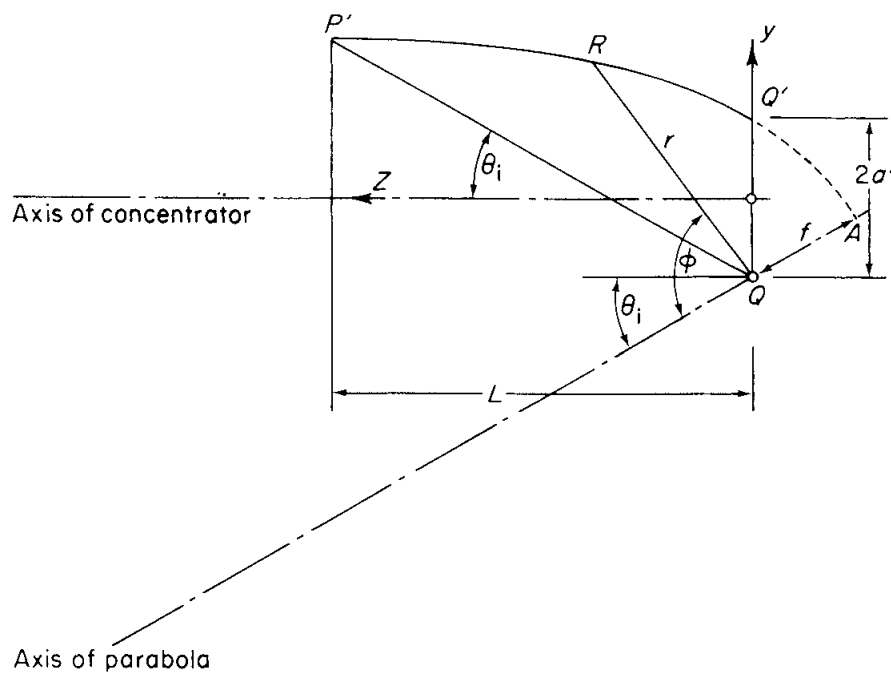


Figure 8.4: Illustration of the parametric CPC construction. Source [61]

for the cartesian coordinates y and z of the tilted parabola piece are then:

$$y = r \sin(\phi - \theta_i) - a' = \frac{2a'(1 + \sin(\theta_i) \sin(\phi - \theta_i))}{1 - \cos(\phi)} - a' \quad (8.1)$$

$$z = r \cos(\phi - \theta_i) = \frac{2a'(1 + \sin(\theta_i) \cos(\phi - \theta_i))}{1 - \cos(\phi)} \quad (8.2)$$

a' is the half width of the exit opening and can be expressed as a function of the half width of

the entry aperture a :

$$a' = a \sin(\theta_i) \quad (8.3)$$

The length L of the CPC is given by

$$L = \frac{a + a'}{\tan(\theta_i)} \quad (8.4)$$

It should be noted that the untruncated cpc has parallel walls at the entry. As with the CEC the parabola can be rotated around the optical axis to obtain a 3D compound parabolic axisymmetric concentrator CPC or the curve is used as the profile of a trough 2D CPC.

8.3 The generalized Etendue or Lagrange invariant and its implications for the use of a CPC as a diffuser

The interest of non imaging concentrators for light diffusing applications might not be directly apparent. The idea pursued in this thesis is to use the angle transforming properties of non imaging concentrators to transform the angular spectrum of the diverging source. The physical quantity that describes this property is the generalized etendue or Lagrange invariant. It depends on the acceptance cone and the entry aperture. If there are no other apertures that cut off the beam then it is an invariant for the entire optical system. For a system with beam dimensions dx and dy and the optical direction cosines dp and dq [60] then the generalized etendue invariant takes on the form:

$$dx \, dy \, dp \, dq = dx' \, dy' \, dp' \, dq' \quad (8.5)$$

For the specific case of a two dimensional concentrator as the one illustrated in Figure 8.3 the etendue invariant is

$$4na \sin(\theta) = 4n' a' \sin(\theta') \quad (8.6)$$

where n is the refractive index at the entry and n' the refractive index at the exit. a and a' are the half width of the entry and exit aperture.

Figures 8.5 to 8.8 show the ray trace simulation of a reflecting CPC with an acceptance angle of 30° and uniform sources with different FWHM angles. The illumination of a CPC having an acceptance angle of 30° with a source of 40° FWHM (corresponding to $\pm 20^\circ$) leads to an angular distribution that is still in large extends limited to the angle of the source (Figure 8.5). Only a small part is directed to higher angles. A source that exactly fills out the acceptance angle of the CPC is getting turned into an approximation of a full Lambertian source by the CPC (Figure 8.6). Due to the finite precision of the simulated geometry a few rays are turned back (Figure 8.6b). Analysis of the intensity distribution displayed in Figure 8.6c shows that the reflected rays represent only a tiny part of the total intensity. A slight overfilling of the CPC

8.3. The generalized Etendue or Lagrange invariant and its implications for the use of a CPC as a diffuser

by 1° leads to more back reflection (Figure 8.7). A hypothetical uniform source with 90° would be mostly turned back (Figure 8.8).

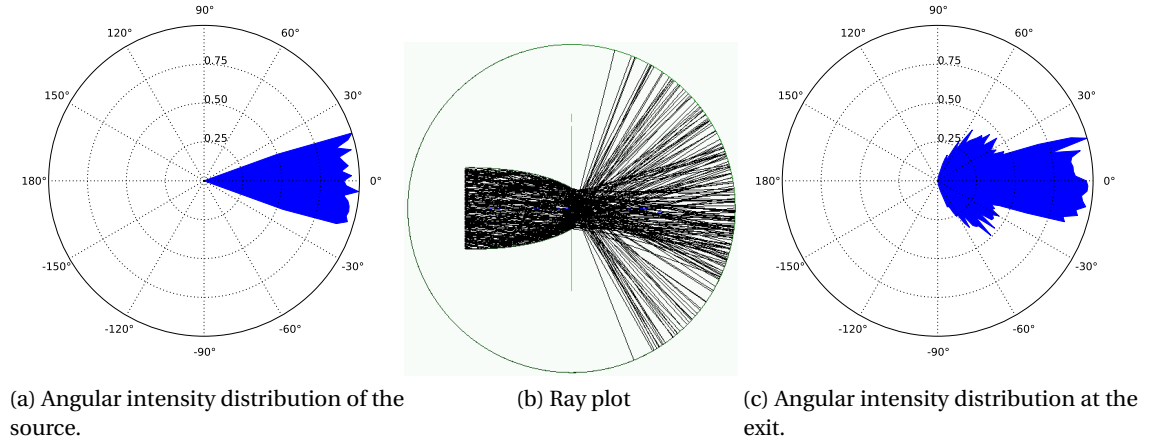


Figure 8.5: Ray tracing of a CPC with an acceptance angle of 30° and a source with $\pm 20^\circ$.

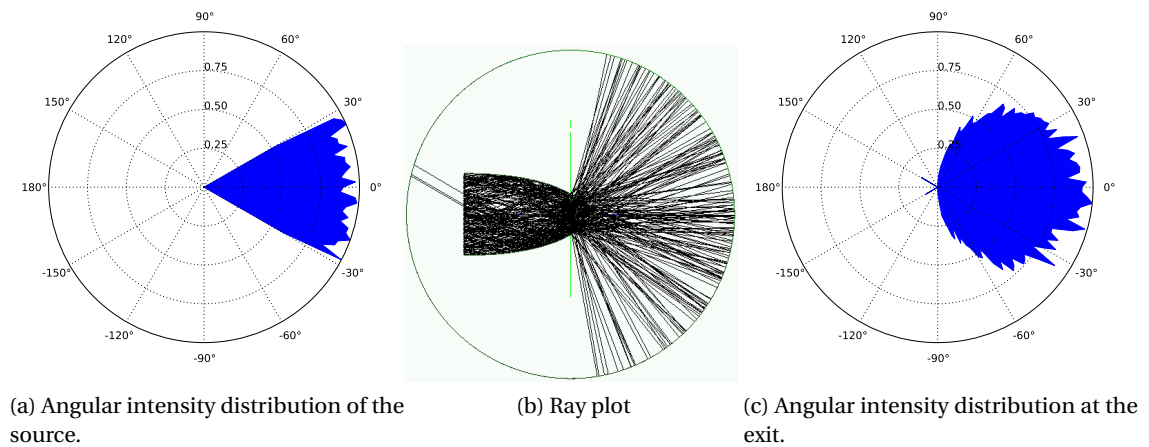


Figure 8.6: Ray tracing of a CPC with an acceptance angle of 30° and a source with $\pm 30^\circ$. Few single rays are rejected.

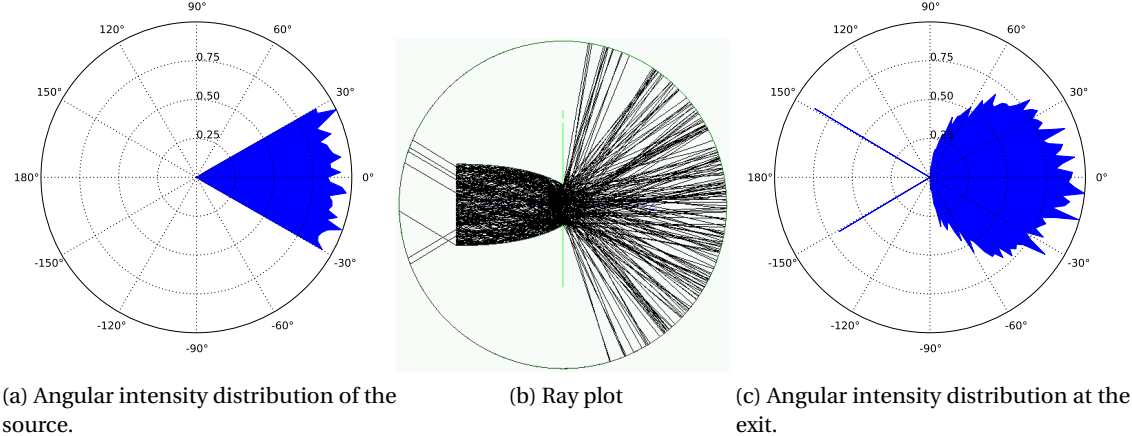


Figure 8.7: Ray tracing of a CPC with an acceptance angle of 30° and a source with $\pm 31^\circ$. A sharp increase in the number of rejected rays can be observed

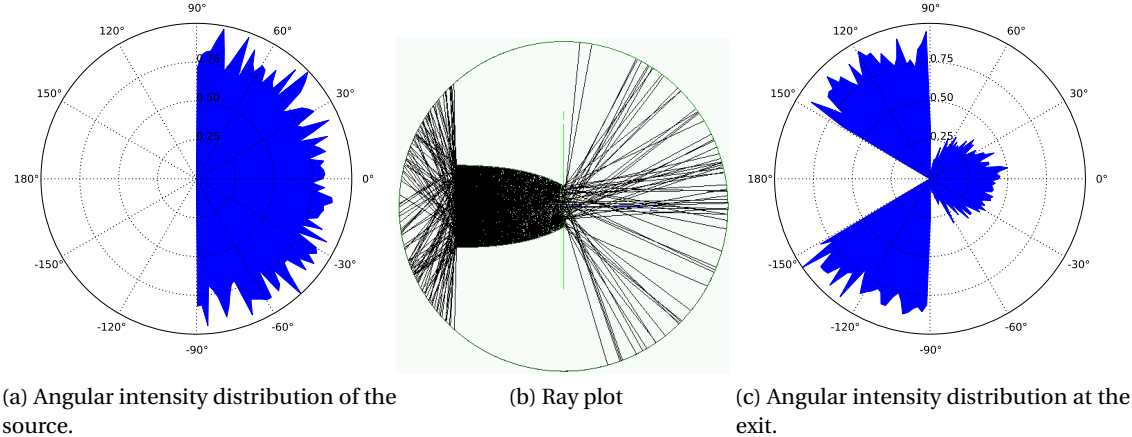


Figure 8.8: Ray tracing of a CPC with an acceptance angle of 30° and a source with $\pm 90^\circ$. A great number of rays are rejected.

8.3. The generalized Etendue or Lagrange invariant and its implications for the use of a CPC as a diffuser

For an optical concentrator it is sometimes interesting to know by how much the light is getting concentrated. Although this thesis is mainly about the angle transforming capabilities of the concentrators the concentration factor is briefly explained here. For fundamental physical reasons the concentration can not exceed a certain maximum value otherwise thermodynamic laws would not be respected. This can be easily seen from Equation (8.6) on Page 46. Since θ' can not exceed $\pi/2$ the concentration factor is limited to C_{max} . The maximum concentration ratio C_{max} for a concentrator with an entry aperture $2a$ and an exit aperture $2a'$ is

$$C_{max} = (a/a') = n'/(n \sin(\theta)) \quad (8.7)$$

for a 2D concentrator with a square entry profile and

$$C_{max} = (a/a')^2 = [n'/(n \sin(\theta))]^2 \quad (8.8)$$

for a 3D axisymmetric concentrator with a circular entry profile where θ is the input semi angle and n is the refractive index at the entry and n' is the refractive index at the exit. For more details on the derivation of the maximum concentration ratio see [60, 61, 64]. As an example the dielectric filled CPC design discussed later on in Chapter 10 has an entry aperture half width $a = 1.77$ mm and an exit aperture $a' = 0.5$ mm which results in a concentration factor $C_{max} = 3.54$ for the 2D trough configuration and $C_{max} = 12.54$ for the 3D axisymmetric configuration.

An ideal concentrator accepts all rays within the acceptance angle and rejects rays with larger angles. The 2D CPC concentrator with reflective end walls is a near perfect concentrator in the sense that it accepts all rays inside the acceptance angle and rejects all the rays that are outside of the acceptance angle. The skew angle of a ray has no influence on the transmission because of the quasi infinite length of the concentrator. For the transmission only the projected angle in the plane perpendicular to the long trough axis intervenes. The 3D CPC is only ideal for rays that pass through the central axis of rotation. Off-axis rays might be rejected after several reflections even when inside the acceptance cone. Winston et al. [61] traced different rays for a CPC with an acceptance angle $\theta_{max} = 10^\circ$. The resulting patterns of accepted and rejected rays are reproduced in Figure 8.9.

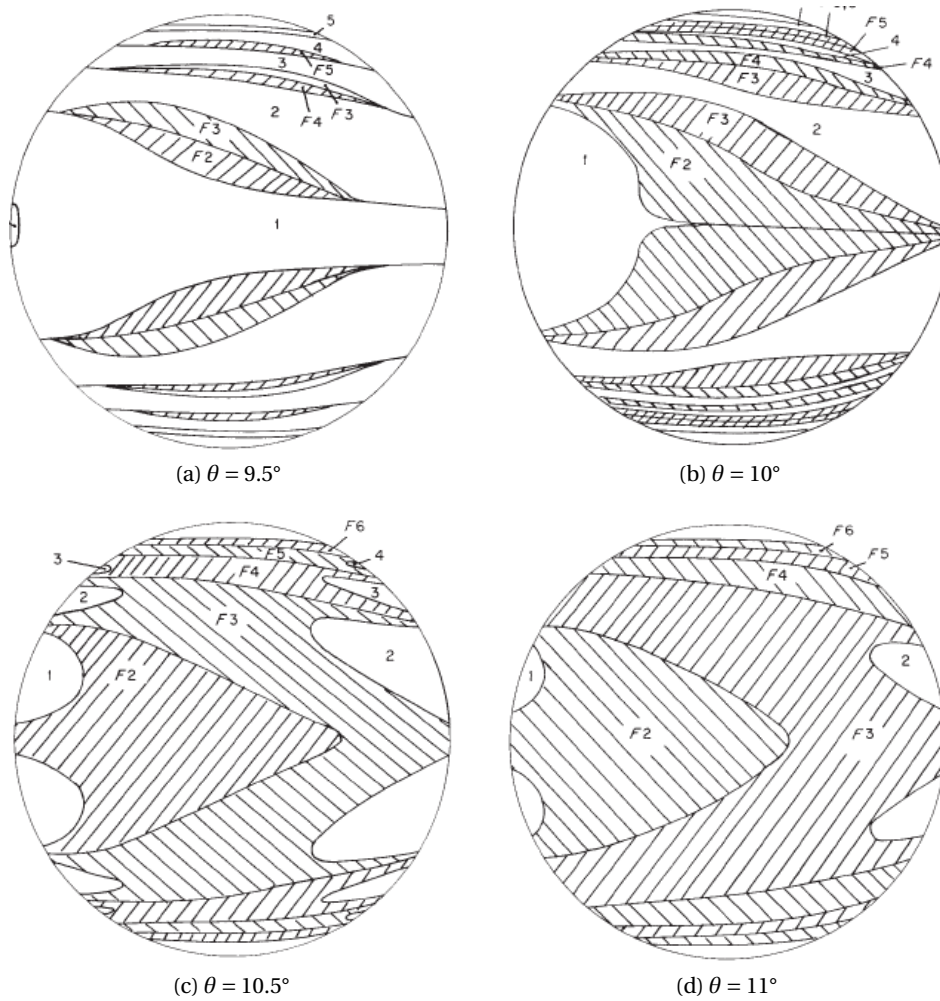


Figure 8.9: Patterns of accepted and rejected rays at the entry face of a CPC with $\theta_{max} = 10^\circ$. The entry aperture is seen from above with incident rays sloping downward to the right forming an angle θ to the axis of rotation of the CPC. Rays entering areas labeled n are transmitted after n reflections; those entering hatched areas labeled Fm are turned back after m reflections. Source [61]

8.4 The dielectric filled CPC design and the θ_i/θ_o converter

Winston et al. [65] introduced the solid CPC filled with a dielectric material. This introduction was followed by a number of other publications [66, 67, 68] treating the design particularities of the dielectric filled CPC, sometimes also called dielectric total internal reflection concentrator (DTIRC). The design relies on total internal reflection (TIR) at the boundaries instead of reflective materials. This presents several advantages, e.g. nearly no reflection loss and it is mechanically better suited to fabricate arrays of concentrators with sub millimeter dimensions. Figure 8.10 illustrates a dielectric filled CPC.

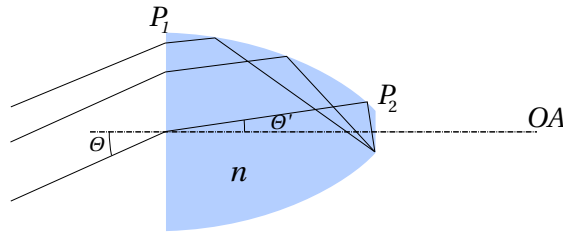


Figure 8.10: Schematic illustration of a dielectric filled CPC with refractive index n .

The CPC is designed for an acceptance angle θ' inside the material with refractive index n . The relation between the acceptance angle θ of the system and θ' inside the concentrator is

$$n \sin(\theta') = \sin(\theta) \quad (8.9)$$

The condition for total internal reflection is then

$$\sin(\theta) \leq n - \frac{2}{\sqrt{n}} \quad (8.10)$$

Since the sine can only take values between 0 and 1 the index of refraction n of the dielectric must be $\geq \sqrt{2}$. Figure 8.11 shows a plot of the required refractive index n as a function of the maximum acceptance angle θ . Typical polymers such as polycarbonate (PC), polymethyl-

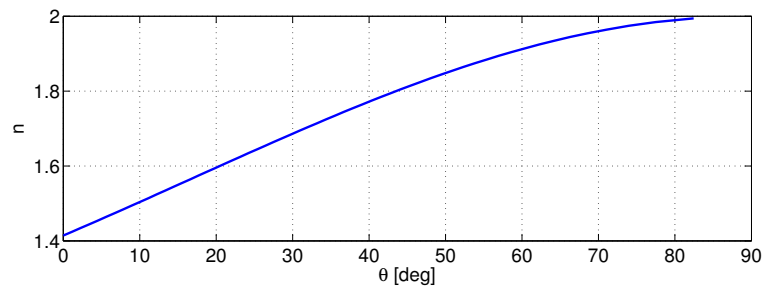


Figure 8.11: Required index of refraction n as a function of the input acceptance angle θ to guarantee TIR conditions.

metacrilate (PMMA) or polydimethylsiloxane (PDMS) have a refractive index around 1.5 in the visible range. High refractive index polymers (HRIP) can have an index of refraction up to 1.8 [69]. From Figure 8.11 it can be seen that the maximum acceptance angle is limited by the refractive index of the transparent polymers to about 30° if a 100% TIR has to be guaranteed.

An additional advantage of the dielectric filled CPC is the fact that for the same acceptance angle it is possible to obtain a higher concentration ratio when compared to the standard reflective CPC design [70].

Coupling light from a dielectric CPC into air or any other material with a significantly lower refractive index than the CPC material requires some modifications of the CPC shape. Otherwise a part of the light is rejected due to TIR at the exit. The modified shape is a so called θ_i/θ_o transformer [61], where $\theta_o < \pi/2$. In order to avoid any losses due to TIR at the exit θ_o has to be smaller than the critical angle $\theta_c = \arcsin(n_2/n_1)$ where n_2 is the refractive index inside the CPC and n_1 is the refractive index of the medium at the exit.

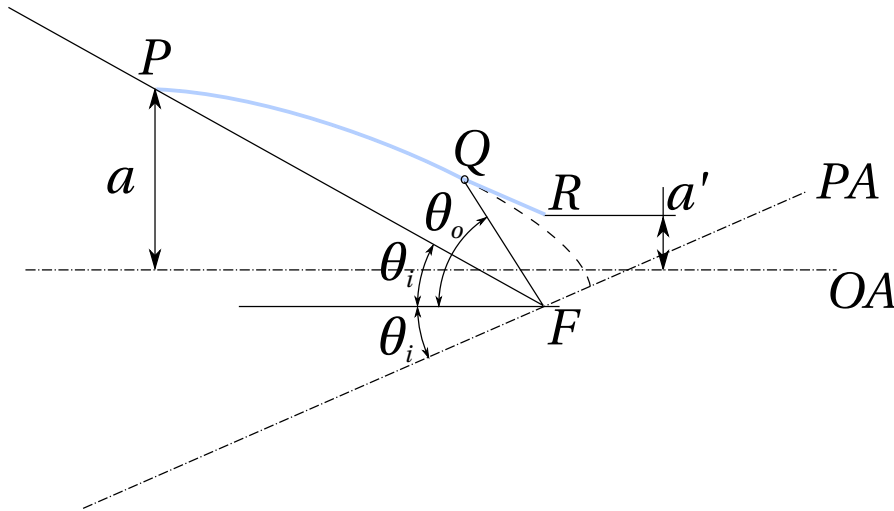


Figure 8.12: Illustration of the θ_i/θ_o converter. Between P and Q the curve corresponds to a CPC with acceptance angle θ_i and entry aperture $2a$. Between Q and R the CPC curve is replaced by a straight line.

The construction of the θ_i/θ_o converter is similar to the standard CPC described in Section 8.2. The only difference to a standard CPC with acceptance angle θ_i and length L is that the range of the angle ϕ that the radial vector swipes between P and Q is $2\theta_i$ to $\theta_i + \theta_o$. The final piece between Q and R is a straight line that forms an angle $\frac{1}{2}(\theta_o - \theta_i)$ with the axis of the concentrator. This is an ideal concentrator with

$$\frac{a}{a'} = \frac{\sin(\theta_o)}{\sin(\theta_i)} \quad (8.11)$$

Lee et al. [71] propose to add a micro structure to the exit surface to optimize coupling efficiency.

8.5 The simple cone concentrator

A simple design for a concentrator consists of a cone with half angle γ . This non imaging concentrator is briefly compared with the CPC to give more insight on the operating principle. See Figure 8.13 for an illustration of the cone concentrator.

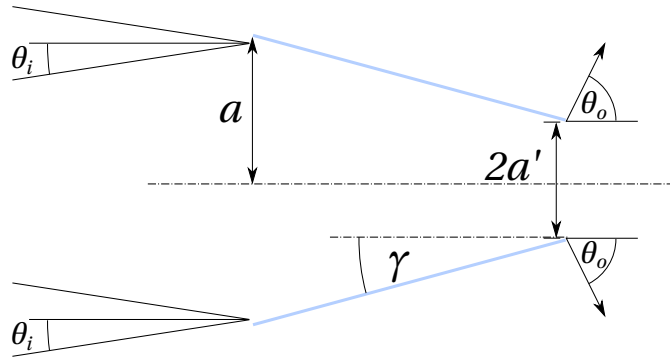


Figure 8.13: Simple reflective cone concentrator with half angle γ

The output angle θ_o depends on the number of reflections k , the input angle θ_i and the inclination γ of the cone boundaries to the concentrator's axis.

$$\theta_o = 2k\gamma + \theta_i \tag{8.12}$$

Williamson introduced in 1952 a simple geometrical construction method for simple cones

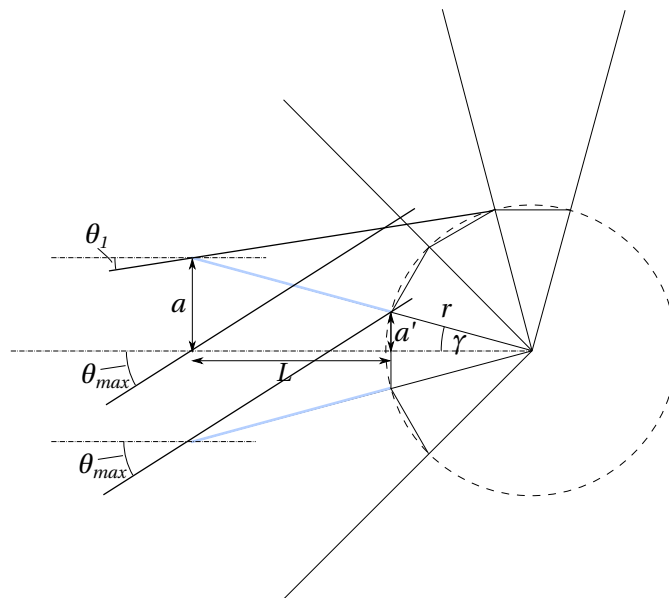


Figure 8.14: Simple cone concentrator design method proposed by [72]. All the rays that touch the central polygon formed by the exit apertures are passed through the cone.

or V-troughs [72]. An illustration of this so called pitch-circle construction [60] is given in Figure 8.14. The cones are repeated around a center defined as the point where the extension of the two cone boundaries would meet. The exit apertures of the cones form a polygon. In order for a ray to pass the cone it has to hit the central polygon, otherwise it is reflected back. The relation for the output angle given in Equation (8.12) can be easily deduced from the illustration in Figure 8.14.

If the maximum acceptance angle θ_{max} is defined similarly to the CPC as the ray that enters at one extremity and grazes the exit at the other extremity then it can be seen, that some rays inside the acceptance cone are reflected back. The maximum angle for which all rays are accepted is given by θ_1 which is obviously smaller than θ_{max} . Table 8.1 shows a comparison between cone and CPC. To obtain a meaningful comparison the acceptance angle θ_{max} and the concentration factor C_{max} are the same for both designs. The transmission data from Welford's book [60] confirm that a certain amount of light inside the acceptance cone are reflected back. Thus the cone concentrator is less efficient than the CPC design.

Table 8.1: Comparison of some properties of the simple cone concentrator and the CPC.

Property	CPC	Cone
Acceptance angle	θ_{max}	θ_{max}
Concentration	C_{max}	C_{max}
Transmission inside θ_{max}	>99%	<80%
Ideal concentrator	Yes	No

9 Applications for a compact CPC array design

Non imaging concentrator optics are often rather bulky. Concentrator designs with dimensions of the order of several ten centimeters up to tens of meters are not uncommon for thermal solar applications (see Figure 9.1).



(a) Experimental 1 MW solar furnace at Promes Odeillo, France. ©by David Blaikie



(b) Parabolic trough concentrator array. Source: NREL

Figure 9.1: Two examples of (non imaging) reflector optics for thermal solar energy applications. Note the big dimensions.

For luminaries the free form optics (see Figure 9.2) are usually made by diamond turning of a master and reproduction by injection molding [73, 74]. Their dimensions are depending on the application of the order of a few centimeters with the lower limit of a few millimeters given by the diamond tooling.

For certain applications such as photovoltaic solar cells and LED luminaries it would be an advantage to have a concentrator design that has similar dimensions as micro lens arrays leading to a more planar structure with an overall thickness of the concentrator of less than five millimeters. Donati et al. [75] discuss also the use of a micro concentrator array to improve certain image photo detectors.

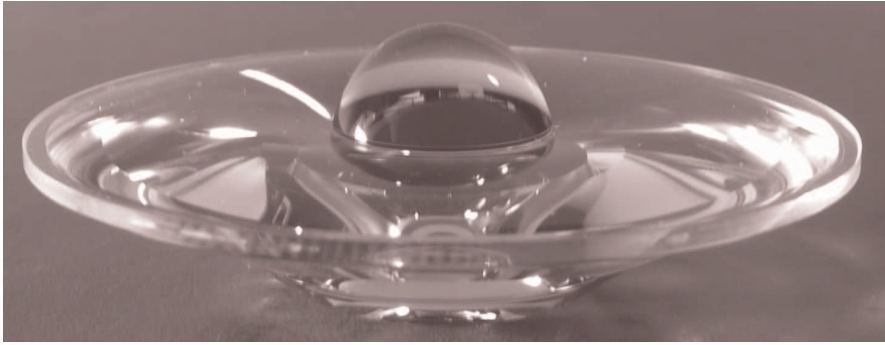


Figure 9.2: RXI free form LED collimator. The total height is about 14 mm. Source [73]

9.1 LED collimator

In this section I will briefly discuss the properties of a compact CPC array for the collimation of LEDs or other Lambertian sources as it was introduced by [76]. Up to here the CPC was presented as a concentrator, meaning the light passing an entry aperture with diameter $2a$ is concentrated on an exit aperture with diameter $2a'$ where $a > a'$. In the case of an ideal concentrator with maximal concentration it is possible to transfer an entry angle θ_i into an exit angle of 90° . There is nothing that prevents us from turning around the direction of the light and thus reduce the angle of a Lambertian source to the acceptance angle θ_i of the CPC. The only problem is the unpractical length of the device. The length of a CPC is given by Equation (8.4) which is repeated below for convenience as a function of the small aperture a' and the acceptance angle θ_i .

$$L = \frac{a + a'}{\tan(\theta_i)} = \frac{a'(1 + \frac{1}{\sin(\theta_i)})}{\tan(\theta_i)} \quad (9.1)$$

It becomes immediately clear that in order to collimate a Lambertian source to $\theta_i = 0^\circ$ the length of the device tends to infinity. But for some applications a collimation of $< 10^\circ$ is already enough.

The typical modern high power LED is an array of active zones with a polymer dome lens cover (see Figure 9.3). The total size of the active area is about $10 \text{ mm} \times 10 \text{ mm}$ and the size of a single emitter is about $0.2 \text{ mm} \times 0.2 \text{ mm}$. A single CPC collimator with $\theta_i = 10^\circ$ that replaces the dome lens would have a length of 168 mm and this at a diameter at the larger end of 58 mm! That is where the advantage of a compact CPC array becomes clear. An array of CPCs with an acceptance angle $\theta_i = 10^\circ$ and a diameter of the small end of 0.2 mm that could be basically placed over each single emitter would result in a length of 6.7 mm and a diameter at the large end of 1.15 mm. This is not much more than the domed lens cap of the above mentioned CREE LED which has a height of 6.1 mm.

In a second step the pre-collimated radiation from the CPC array could be further collimated with a normal lens.



Figure 9.3: High power white LED CREE XLamp MP-L. The array of single emitters is visible under the polymer dome lens cover.

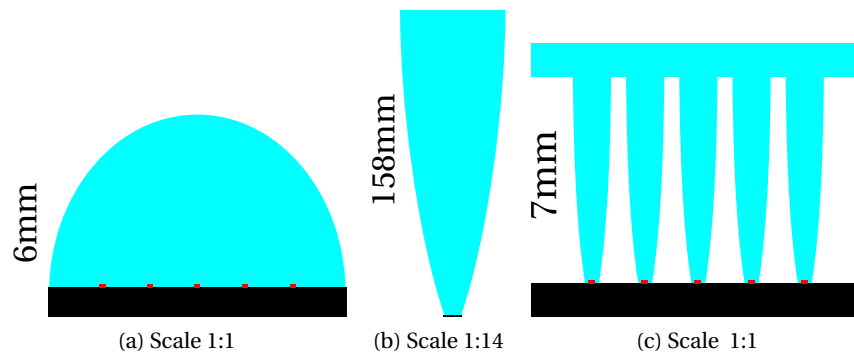


Figure 9.4: LED collimation: comparison between the classical polymer dome lens (a), which does not collimate the light, a CPC for the entire chip that collimates to 10° (b) and an array of miniaturized CPCs (c). Note that (a) and (c) are to scale relative to each other but (b) is scaled down by a factor of 14.

More sophisticated non imaging collimator for LEDs have been reported by Grabovickic [77], Moiseev [78], Dross [79, 80, 81], Kudaev [82], Miñano [83], Zhenrong [18, 84] and Spigulis [85]. Those RXI (standing for refraction, reflection and total internal reflection) collimator were designed by the so called simultaneous multiple surface (SMS) method introduced by Benítez and Miñano [86].

9.2 Fiber bundle coupler

Efficiently coupling incoherent light from Lambertian sources such as LEDs into fiber bundles is difficult with lens systems. Thyagarajan et al. [87] treat the theoretical aspects of efficiency limits when coupling incoherent light from uncollimated sources into optical fiber bundles. They find that a CPC with an acceptance angle corresponding to the acceptance angle of

the fiber bundle is an ideal mean of coupling light into a fiber bundle. See Figure 9.5 for a schematic illustration of such a CPC fiber coupler. The publication by Thyagarajan et al. [87]

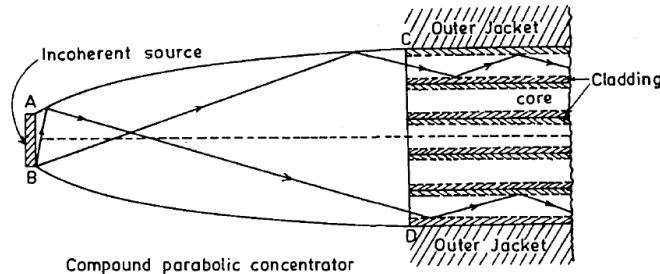


Figure 9.5: Illustration of a CPC fiber coupler as described by Thyagarajan et al. in [87]

does not touch on the actual realization of such CPC fiber couplers. Nakamura et al. [88] propose a fabrication process for hollow reflective CPC fiber couplers based on powder blasted structures in glass that are metalized to be reflecting. The fabrication process of compact dielectric CPC arrays realized during this thesis could be easily adapted to typical fiber bundles with an active diameter of around 1 mm and an acceptance angle around 10° .

9.3 Micro concentrated solar cells

For concentrator photovoltaic (CPV) the light is concentrated to increase efficiency. Highly concentrated photovoltaic have concentration factors bigger than 100 [89, 90]. High concentration factors do not only bring higher intensity but also the additional challenge of thermal management [91]. As discussed in Section 8.3 the concentration factor is inverse proportional to $\sin(\theta_i)$ respectively $\sin(\theta_i)^2$. This means that for high concentration factors the acceptance angle has to be small and as a consequence the highly concentrated solar cell also requires a tracking system for proper alignment [92, 93].

The efficiency increases theoretically as the logarithm of the intensity, until it reaches too high a value of current density, leading to ohmic losses that reduce the efficiency. Thus concentrator cells must be specially designed to have very low series resistance [94, 95]. In most solar cell designs, the photocurrent is extracted through a conducting window layer in combination with a silver grid at the front of the device. The trade-off between series resistance and shadowing requires either buried contacts or screen printing of narrow lines with high aspect ratio.

The compact dielectric CPC array presents an alternate approach where concentrators direct the incoming light into the cell. The front metalization can thus be extended over the area between the paraboloids without shadowing loss. See Figure 9.7 for an illustration of the concept.

The concept discussed here does not aim at maximum concentration but rather at a system that is still reasonably thin, does not necessarily need active sun tracking and collects also the

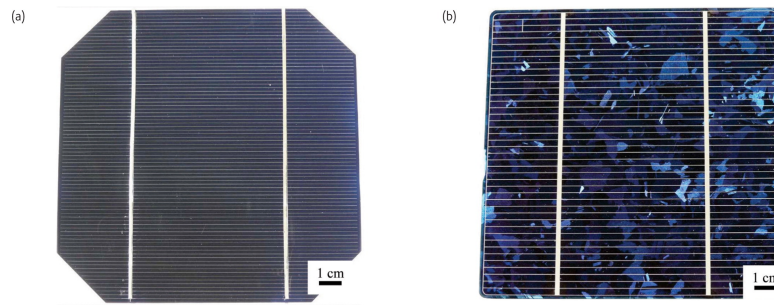


Figure 9.6: Two examples of crystalline respectively polycrystalline solar cells with the front electrode grid and the larger bus line clearly visible. Source [96]

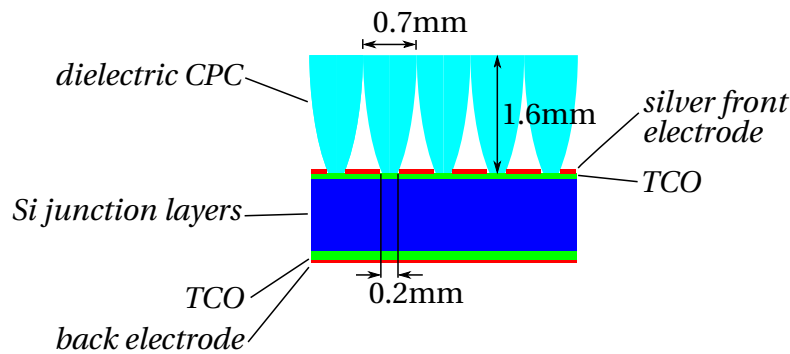


Figure 9.7: Illustration of a PV cell with a compact 2D CPC array with an acceptance angle of 24° . The width of the illuminated zone of the cell is 0.2 mm. The concentration factor is 3.5.

diffuse light which represents an important part of light in temperate climate zones where the sky is often covered.

The use of dielectric filled concentrators for PV cells, especially for facade integration of solar cells, was described by Zacharopoulos et al. [97] and Mallick et al. [98]. The concentrator elements have typically dimensions of a few 10 mm [99].

Korech et al. [100] discussed a dielectric micro concentrator array for solar cells to reduce series resistance without shadowing loss using a cone trough concentrator array made of glass. With the fabrication technology proposed in Chapter 10 it is actually possible to fabricate the

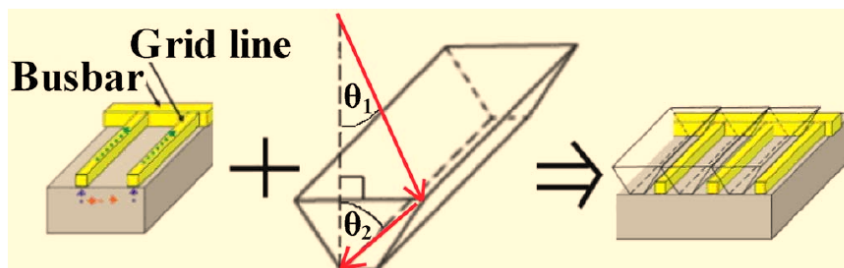


Figure 9.8: Illustration of a cone micro concentrator array. Source [100]

Chapter 9. Applications for a compact CPC array design

exact CPC or θ_i/θ_o shape without adding more fabrication complexity than the fabrication of the simplified cone concentrators proposed by Korech in [100].

Park et al. [101] demonstrated a 3D axisymmetric concentrator based on a tapered waveguide (see Figure 9.9). This concentrator has an acceptance angle around 6° . Because of its dimensions this concept does not really count as compact. In addition it only concentrates the light and does not help to reduce the series resistance.

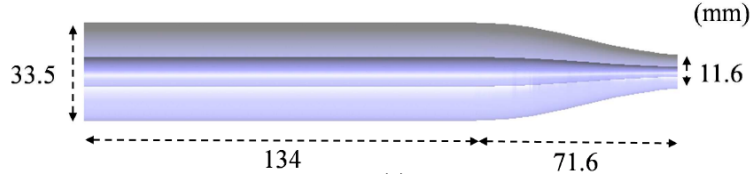


Figure 9.9: Illustration of a tapered waveguide concentrator. Note the relatively large dimensions. Source [101]

The 3D axisymmetric concentrator might look more favorable for micro concentrator array because of its higher concentration factor and the bigger surface that can be metalized when compared with the 2D trough configuration. Nevertheless the 2D trough concentrator is preferable [57, 102, 103, 104] for terrestrial photovoltaic applications without diurnal azimuthal sun tracking for two reasons:

1. The 2D trough CPC with reflective end walls has a theoretical acceptance angle of 90° along its axis thus eliminating the need of diurnal azimuthal sun tracking and improving the collection of diffuse light.
2. There is nearly no loss due to packing density since the gap between the trough structures can be better minimized.

The maximum concentration possible for 2D CPCs [105] depends on the maximal allowable length L , half width a , index of refraction of the material n and acceptance angle θ_i . For convenience the formulas for the length

$$L = \frac{a + a'}{\tan(\theta'_i)} \quad (9.2)$$

the design acceptance angle θ'_i

$$\sin(\theta'_i) = \frac{\sin(\theta_i)}{n} \quad (9.3)$$

and the concentration factor

$$C_{max} = \frac{a}{a'} = \frac{1}{\sin(\theta'_i)} = \frac{n}{\sin(\theta_i)} \quad (9.4)$$

are repeated here for a dielectric 2D CPC submerged in air. It becomes immediately clear that the higher the concentration factor, the smaller the acceptance angle and the longer the CPC will get. This explains also why concentrated photovoltaic that do not need any tracking can only have a moderate concentration factor. On the other hand this allows also for relatively compact systems.

Figure 9.10 shows the elevation angle of the sun as a function of the time of the day. The elevation angle is the angle above or below the celestial equator plane and the sun. This value is independent of the geographical latitude of the observer. Thus the minimum acceptance angle needed for a system without any vertical tracking that needs to collect all the light at noon over the year is 24° . Of course the solar cells need to have a fix inclination which depends on the geographical latitude.

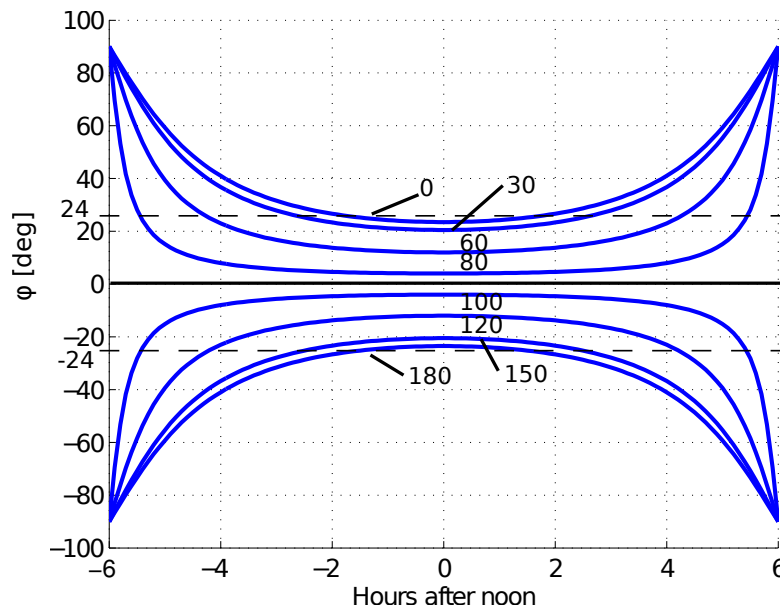


Figure 9.10: The elevation angle ϕ of the sun above or below the equator as a function of the time of the day. Each curve is labeled with the number of days after midsummer. The dashed lines show the minimum acceptance angle for a 2D CPC to collect all the light at noon over the year without vertical tracking.

See Table 9.1 for the concentration ratio and length of a compact dielectric 2D CPC with a refractive index of 1.44 and an exit half width $a' = 0.1$ mm for different acceptance angles. For $\theta_i = 10^\circ$ the CPC becomes impractically long and would need vertical tracking. On the other hand the concentration factor is more than two times higher than for $\theta_i = 24^\circ$. In order to collect more light than just at noon the acceptance angle could be increased to 30° . This would come at the cost of a decrease in concentration of 20% but at the same time would allow to shorten the length of the CPC by 30%. A possibility based on linear corrugated reflectors to increase the acceptance angle without losing too much concentration was discussed by Rönnelid et al. [106].

Chapter 9. Applications for a compact CPC array design

Table 9.1: Concentration ratio and Length for a 2D dielectric CPC with $n = 1.44$ and an exit half width of 0.1 mm for a selection of acceptance angles.

Acceptance angle	10°	24°	30°
Concentration	8.3	3.5	2.9
Length [mm]	7.65	1.54	1.05

The fraction of the surface covered and shadowed by the metal contact fingers and the bus line ranges from a few percentages for normal photovoltaic cells up to 10% for commercial concentrated solar cells [107, 100]. For a micro concentrated solar cell as proposed here with a compact 2D CPC array the surface available for metalization is more than 60% without any shadowing loss!

To reduce the loss due to Fresnel reflection at the interface solar cell - CPC it might be interesting to modify the CPC shape to obtain a θ_i/θ_o converter (Section 8.4). See Figure 9.11 for a plot of the transmission coefficient at a silicon nitride (Si_3N_4) - PDMS interface. Silicon nitride is often used as an anti reflection coating and encapsulation for silicon solar cells [94].

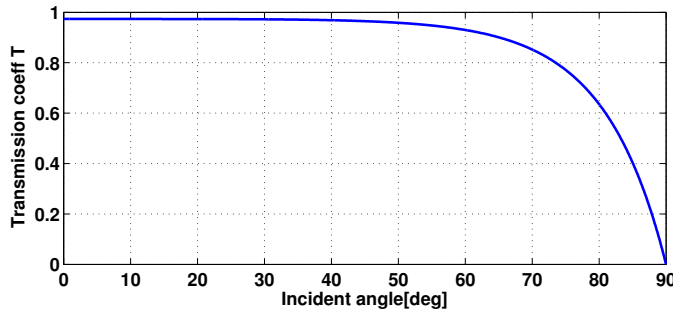


Figure 9.11: Transmission coefficient at a silicon nitride ($n = 2.0$) - PDMS ($n = 1.44$) interface

Korech et al. [100] propose to limit θ_o to 50°. Of course the reduction of reflection loss comes at the price of a lower concentration rate since the concentration of a θ_i/θ_o converter is

$$C = \frac{\sin(\theta_o)}{\sin(\theta_i)} \quad (9.5)$$

The compact dielectric CPC array is best suited for solar cell configurations where the active layers are “at the top” such as crystalline silicon or the more sophisticated HIT (Heterojunction with Intrinsic Thin layer) cells [94]. See Figure 9.12 for an illustration of the cross section of a crystalline silicon and a HIT cell.

Thin film solar cells are usually deposited at the back of a glass substrate and are thus less suitable for the compact CPC array since concentration through the glass is not possible with the CPC. For thin film solar cells deposited at the back of a transparent substrate it

9.3. Micro concentrated solar cells

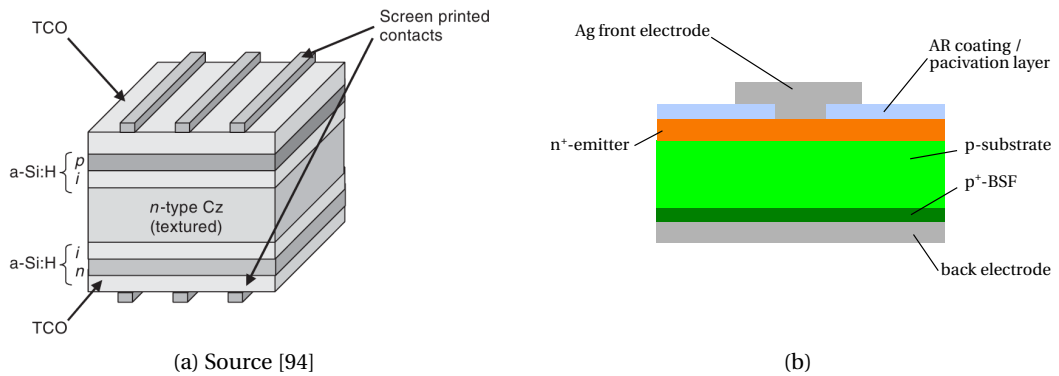


Figure 9.12: Illustration of the cross section of a HIT cell (a) and of a crystalline silicon solar cell (b).

is more interesting to use a cylindrical microlens array at the front of the substrate for the concentration (see Figure 9.13a) [108]. The interconnects of the micro cells still lead to a certain shadowing loss as for conventional cells. Compared to the CPC based concentration system with a relatively large acceptance angle the micro lens concentrator setup is sensitive to misalignment. See Figure 9.13b for a plot of the generated power for a microlens concentrated thin film solar cell as a function of the tilt angle [108]. The periodicity results from focusing light on neighboring cells.

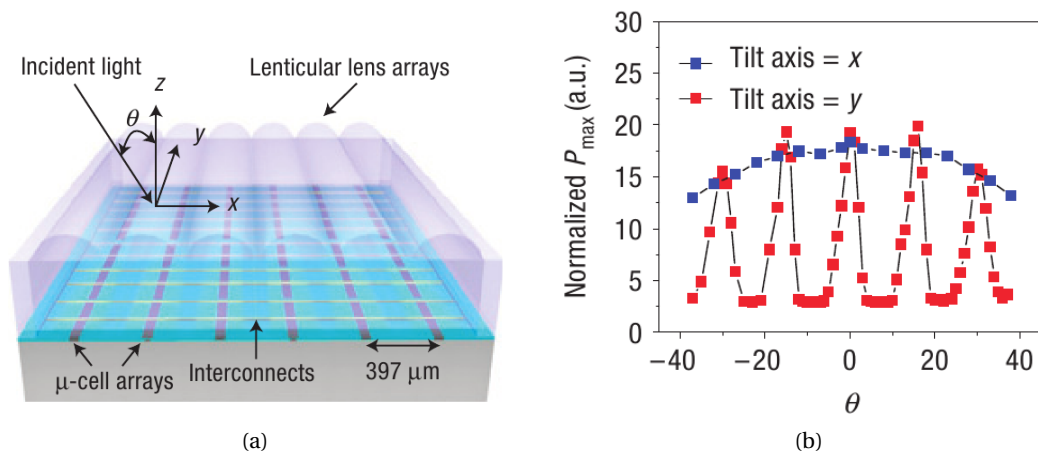


Figure 9.13: Illustration of a microlens concentrated thin film solar cell (a) and the resulting normalized power output as a function of the tilt angle with respect to the sun (b). Source [108]

10 Implementation of a compact dielectric CPC array

In this chapter a complete implementation from the concept, simulation, fabrication and characterization of a compact dielectric CPC array is presented.

10.1 Concept

The goal is to develop a versatile implementation that can be adapted to different applications as discussed in Chapter 9. The usual requirements for micro optical components such as potentially low cost for big volume manufacturing, good reproducibility and possibility to cover large surfaces should apply.

The dimensions of the single CPC should be bigger than 50 μm to avoid large diffraction effects for visible light [109] and less than 5 mm to count still as compact. The acceptance angle of the CPC design presented here is 24°. For lack of specific requirements this value was taken somewhat arbitrarily as the angle that would be needed to accept light from the sun at noon in winter and summer in a place with 50° geographical latitude for a solar cell inclined at a fix angle of 40°.

The material for the dielectric CPC is highly transparent polydimethylsiloxane (PDMS, Silgard® 184 from Dow Corning) which has an average index of refraction of 1.44 at 400 nm. The complete dispersion relation of PDMS can be approximated with the Sellmeier equation (Equation (10.1)).

$$n^2(\lambda) = 1 + \frac{B_1\lambda^2}{\lambda^2 - C_1} + \frac{B_2\lambda^2}{\lambda^2 - C_2} + \frac{B_3\lambda^2}{\lambda^2 - C_3} \quad (10.1)$$

According to [110] the experimentally determined coefficients for the first term are $B_1 = 1.0093$ and $C_1 = 13185 \text{ nm}^2$. See Figure 10.1 for a plot of the dispersion of PDMS over the relevant wavelength range.

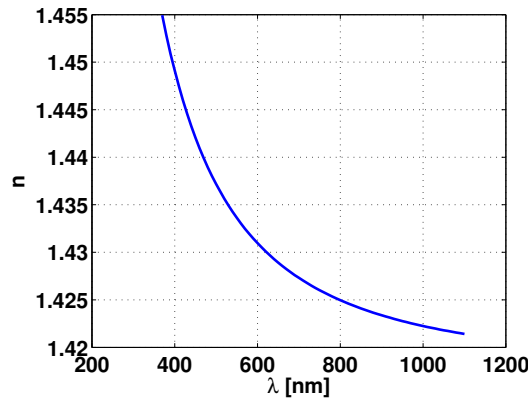


Figure 10.1: Dispersion relation of PDMS. Note that n is always bigger than $\sqrt{2}$

Since the CPC is filled with a dielectric its design acceptance angle θ'_i is

$$\sin(\theta'_i) = \frac{\sin(\theta_i)}{n} \quad (10.2)$$

which results in $\theta'_i = 16.4^\circ$ for $\theta_i = 24^\circ$ and $n = 1.44$. According to Equation (8.4) on Page 46 the total length of the CPC is 7.7 mm if the exit aperture is 1 mm. For practical reasons the CPC is truncated to a length of 5 mm. This has little consequences for the optical performance (see Section 10.2) but has many advantages for the fabrication process. Since the end walls of a full length CPC are parallel (see Section 8.2) it is easier to demold a truncated CPC which has slightly inclined end walls. The fact that the end walls are inclined allows also for less space between the single CPCs in an array and thus a denser packing.

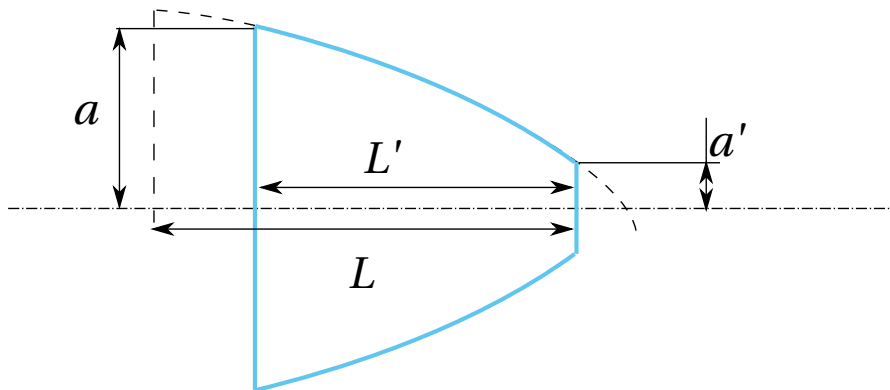


Figure 10.2: Illustration of a truncated CPC of length L' .

As discussed in Section 8.4 an unmodified dielectric CPC is not ideal if the light has to be coupled out into air. For lack of time and resources only the unmodified CPC was realized and experimentally investigated.

10.2 Simulation

The simulation of the different CPC designs is done by incoherent ray tracing with FRED from PhotonEngineering. A Matlab script is used to generate the CPC profile. This allows more design flexibility and control over the parameters than the built in CPC components of FRED. The profile is calculated with the parametric form of the equation for a CPC given in [61] and is repeated below for convenience:

$$y = r \sin(\phi - \theta_i) - a' = \frac{2a'(1 + \sin(\theta_i) \sin(\phi - \theta_i))}{1 - \cos(\phi)} - a' \quad (10.3)$$

$$z = r \cos(\phi - \theta_i) = \frac{2a'(1 + \sin(\theta_i) \cos(\phi - \theta_i))}{1 - \cos(\phi)} \quad (10.4)$$

where z is the optical axis, a' is the half width of the exit aperture, θ_i is the acceptance angle of the CPC and ϕ is the parameter. Since the CPC design is relatively robust, i.e. small deviations from the perfect shape have little influence on the functionality it is not very crucial to choose a fine grained increment for the parameter ϕ . The increment of ϕ is set to 0.1 for all the simulations discussed here. This results in 500 to 1000 points per profile which is just manageable for FRED.

The source used for the simulation is a Lambertian that is clipped to the required angle usually corresponding to the acceptance angle of the CPC. If not mentioned differently the wavelength is 633 nm and the source is incoherent and unpolarized.

Figure 10.3 shows the influence of the truncation on the angular intensity distribution. For the large angles there is no difference to the full length CPC. But at the angles around and below the acceptance angle there are some marked differences visible.

If the light is coupled from a dielectric CPC to air there are some losses expected due to back reflection at the exit aperture. The critical angle for the extraction of light from a material with higher index of refraction is given by Snell's law of refraction:

$$n_1 \sin(\theta_1) = n_2 \sin(\theta_2) \quad (10.5)$$

and for the critical angle if $n_2 = 1$

$$\theta_c = \arcsin(1/n) \quad (10.6)$$

For PDMS with a refractive index of 1.43 at 600 nm the critical angle is $\theta_c = 44.37^\circ$. Light is not only reflected once the critical angle is reached but reflection is already present before. The amount of light that is reflected at an interface between two materials with refractive index n_1 and n_2 and for which $n_1 > n_2$ depends also on the incident angle θ_1 and the polarization of

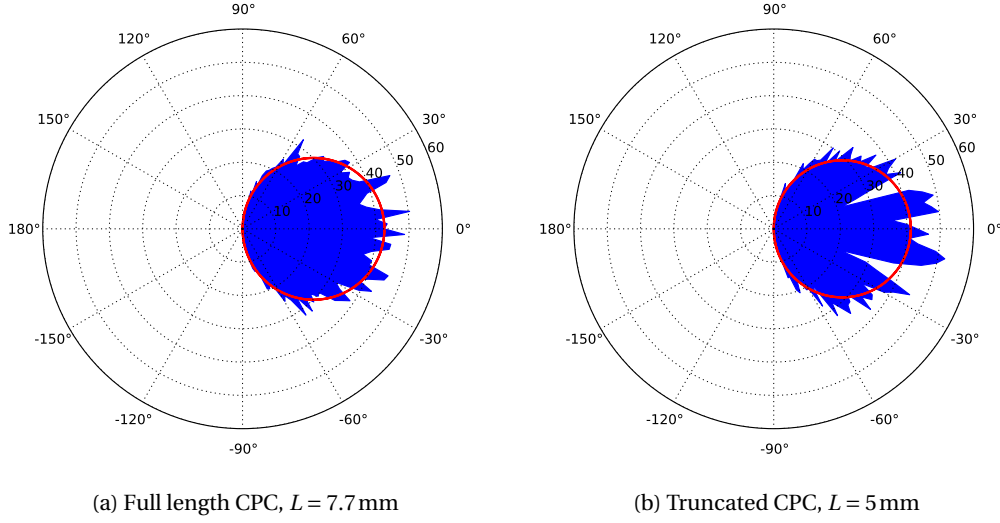


Figure 10.3: Simulation of the truncation effect on the angular intensity distribution of a dielectric filled CPC. For the simulation the media at the exit has the same refractive index as the dielectric inside the CPC.

the light. The power reflection coefficients are given by the Fresnel equations [52] given below

$$R_s = \left| \frac{n_1 \cos(\theta_1) - n_2 \cos(\theta_2)}{n_1 \cos(\theta_1) + n_2 \cos(\theta_2)} \right|^2 = \left| \frac{n_1 \cos(\theta_1) - n_2 \sqrt{1 - \left(\frac{n_1}{n_2} \sin(\theta_1)\right)^2}}{n_1 \cos(\theta_1) + n_2 \sqrt{1 - \left(\frac{n_1}{n_2} \sin(\theta_1)\right)^2}} \right|^2 \quad (10.7)$$

$$R_p = \left| \frac{n_1 \cos(\theta_2) - n_2 \cos(\theta_1)}{n_1 \cos(\theta_2) + n_2 \cos(\theta_1)} \right|^2 = \left| \frac{n_1 \sqrt{1 - \left(\frac{n_1}{n_2} \sin(\theta_1)\right)^2} - n_2 \cos(\theta_1)}{n_1 \sqrt{1 - \left(\frac{n_1}{n_2} \sin(\theta_1)\right)^2} + n_2 \cos(\theta_1)} \right|^2 \quad (10.8)$$

For unpolarized light the reflection coefficient is the average of R_s and R_p

$$R = \frac{R_s + R_p}{2} \quad (10.9)$$

Because of the conservation of energies the transmission coefficient is

$$T = 1 - R \quad (10.10)$$

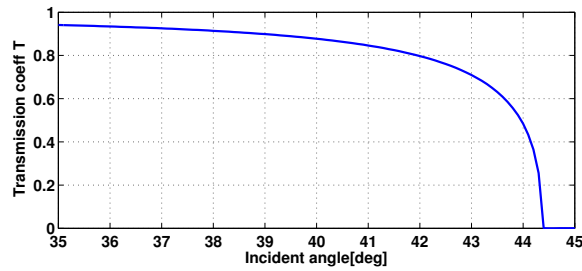


Figure 10.4: Transmission coefficient for a PDMS to air interface.

Figure 10.4 shows the transmission curve for a PDMS-to-air interface. It shows that the transmission is not a binary function but is rather gradually decreasing towards the critical angle and total internal reflection (TIR).

Simulation of a full length CPC made of PDMS that couples light to air (Figure 10.5b) shows that the angular intensity distribution still corresponds well with a Lambertian distribution (red circle in the graph) but that the loss due to back reflection at the exit interface is considerable.

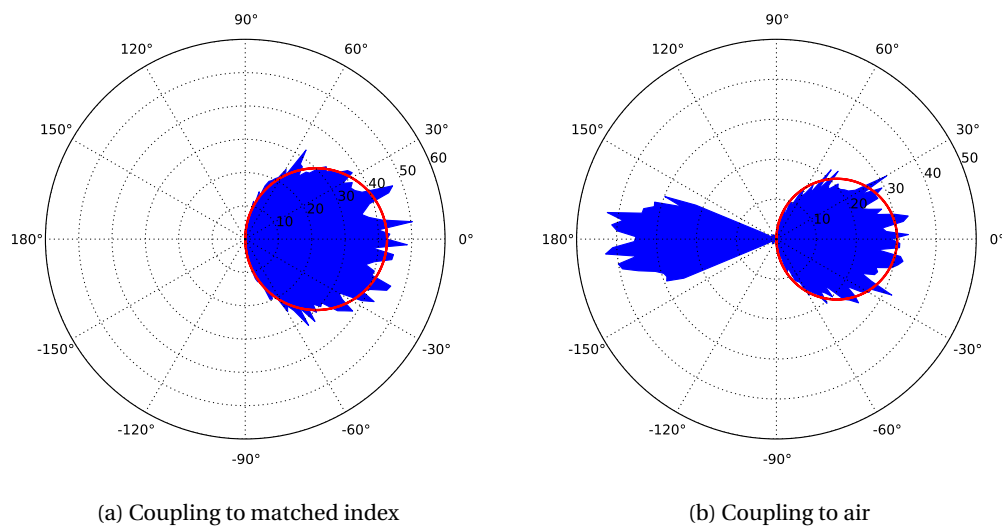


Figure 10.5: Ray tracing simulation of a dielectric CPC made of PDMS coupling to a matched index (a) and the same CPC coupling to air (b). The red circle marks a perfect Lambertian scaled to the intensity at 0°.

As described in Section 8.4 a possible improvement on the dielectric CPC for coupling light to air is the θ_1/θ_2 converter which is a slightly modified CPC design where the maximal output angle is θ_2 instead of 90°. For $\theta_2 = \theta_c$ (Figure 10.6a) there is still some back reflection due to Fresnel reflection (Equation (10.9) and Figure 10.4).

It has to be noted that the angular distribution of the light coming from a dielectric θ_1/θ_2 converter is not Lambertian anymore. The large angles are not as present as in the standard

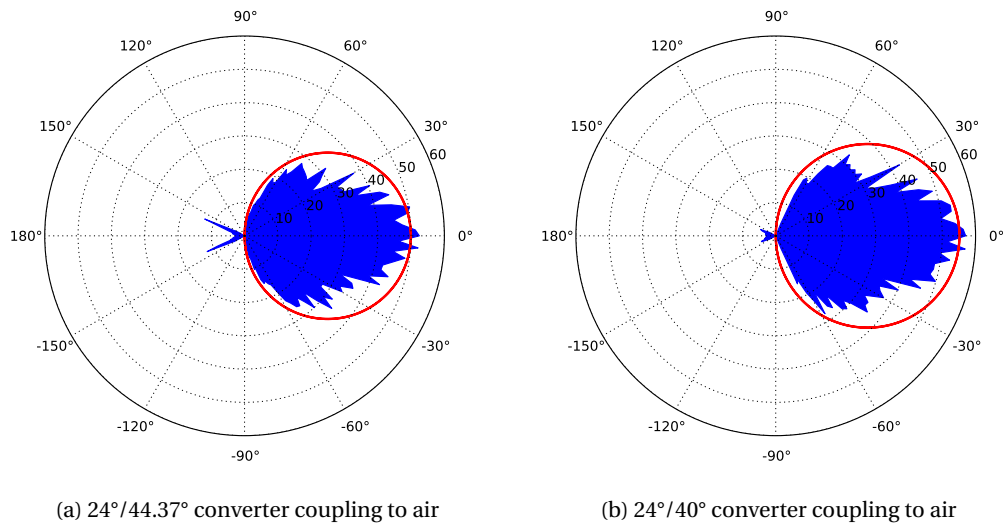


Figure 10.6: Ray tracing simulation of a dielectric θ_1/θ_2 converter made of PDMS coupling light to air. In (a) $\theta_2 = \theta_c = 44.37^\circ$ and in (b) $\theta_2 = 40^\circ$. The red circle marks a perfect Lambertian scaled to the intensity at 0° .

Lambertian distribution. From this it becomes clear that there is a trade off between transmission efficiency and perfectly Lambertian distribution when coupling from a dielectric concentrator to air.

10.3 Fabrication

For the prototype fabrication of the compact dielectric CPC array a PDMS replication process of a master device was used. Two different process flows were realized:

1. The PDMS is molded directly in a negative master.
2. The positive master is first replicated with a negative silicone mold of which the PDMS replica is made afterwards.

For illustrations of the process flow see Figure 10.7 and Figure 10.10 respectively.

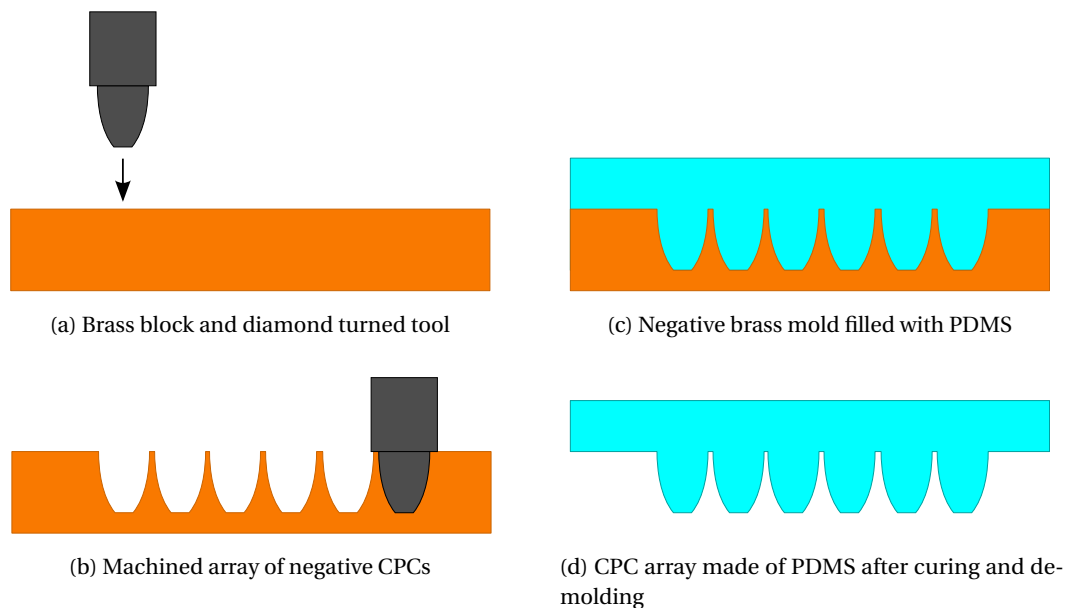


Figure 10.7: Process flow for the direct replication in PDMS of a negative master. The master is machined by diamond turned tooling from a solid block of brass. This process allows the fabrication of 3D as well as 2D trough structures

The negative mold/master is machined in a brass block with a diamond turned tool by Idonus Sarl in Neuchâtel, Switzerland. Figure 10.8a shows the cross section of the diamond tool with the relevant dimensions. For the tool maker the shape of the CPC has to be approximated by a series of radii that are also displayed in Figure 10.8a. The advantage of diamond turned tools is that the surface quality of the machined brass is relatively good and does not necessarily require any additional chemical polishing. The surface roughness measurements were performed with a white light interferometer from Veeco. See Figure 10.8b for the a surface profile. The RMS roughness of the surface machined with the diamond turned tool is about $R_{rms} = 200$ nm. This seems rough when compared with surface flatness requirements of imaging systems which are typically $\lambda/10$. But the optical power transfer in a CPC is relatively robust to errors [61]. Scattering at the surface may lead to some rays inside the acceptance

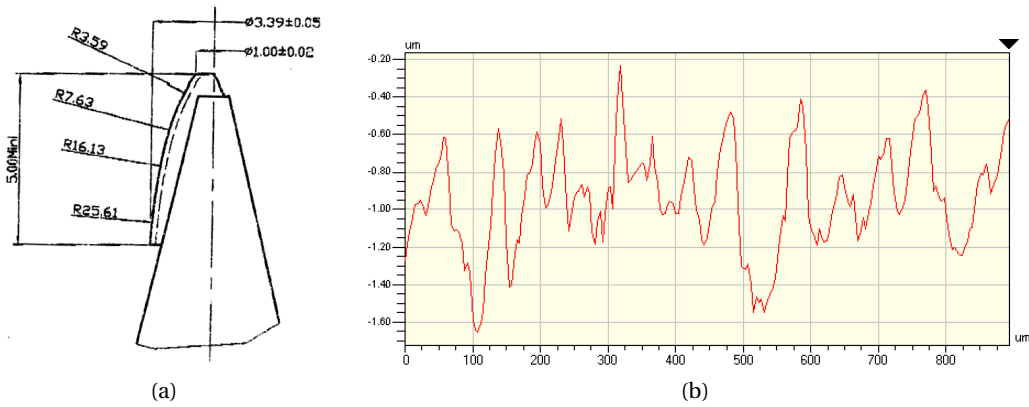


Figure 10.8: (a) Cross section of the diamond turned drill tool with a set of radii to approximate the parabolic shape.(b) Surface profile showing the roughness of brass part machined with the diamond turned tool.

angle to be rejected and some outside of the acceptance angle to be accepted. For the prototype presented here it was decided to forgo any additional chemical polishing of the surface.

With one and the same tool it is possible to drill a matrix of CPC shaped holes for an array of 3D CPCs or to machine a series of 2D CPC troughs. See also Figure 10.9 for an image of the brass negative master.

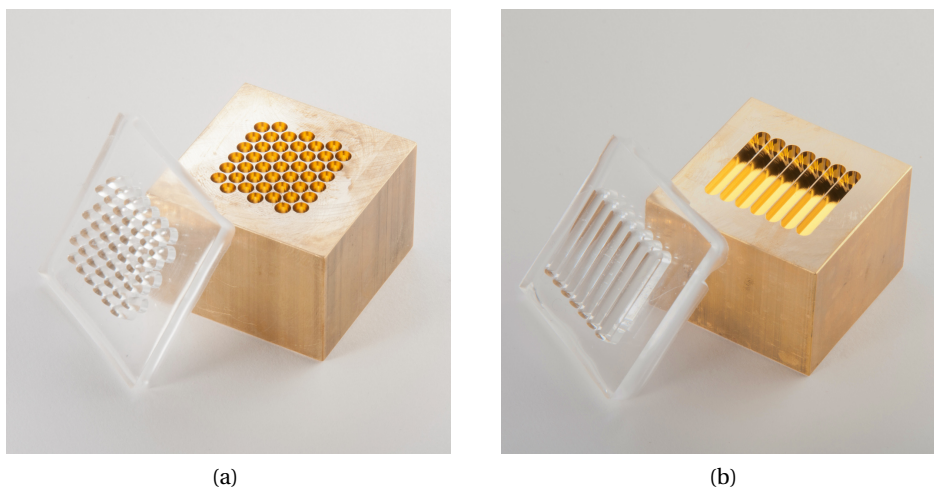


Figure 10.9: Brass mold and replicated CPC array made of transparent PDMS. (a) shows a hexagonal array of 3D CPCs and (b) shows an array of 2D CPCs. The CPCs are designed for acceptance angles of 24° and are truncated to a length of 5 mm. The width of the entry aperture is 3.4 mm and the width of the exit aperture is 1 mm.

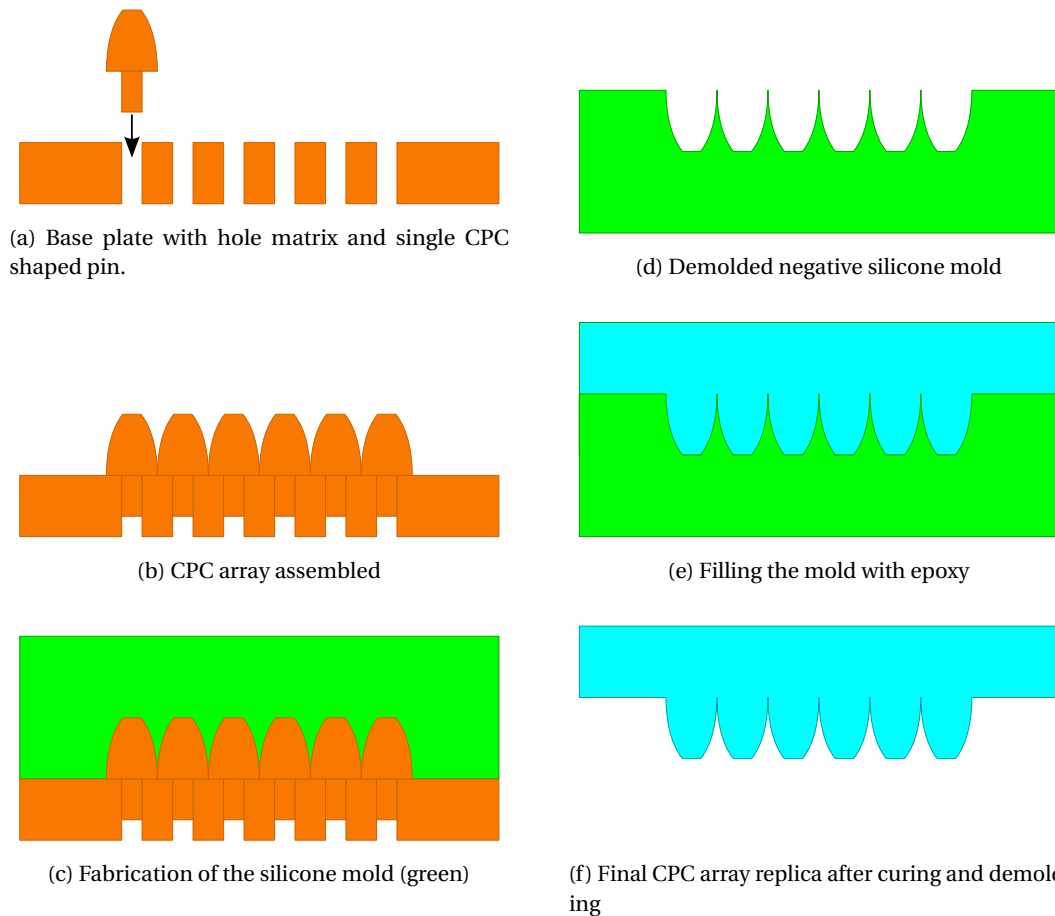


Figure 10.10: Process flow with a positive master assembled from single CPC shaped brass pins.

The second fabrication procedure is based on a positive master and a negative mold in soft silicone. See Figure 10.10 for the process flow. The CPC array of the master is not machined from a block of brass but is an assembly of CPC shaped pins instead.

The machining of the pins and the brass base plate with a hole matrix was done by a supplier for the watch industry (Chatelaine Prototype Sarl). The single pins are press-fitted one by one into the holes of the base plate to form the positive master. See Figure 10.11 for the cross section and the dimensions of a single CPC shaped brass pin with an acceptance angle of 30° .

The silicone mold is made with Mold Star® 15 by Smooth On, a platinum cured silicone rubber that is very strong and flexible. The shrink factor of the rubber is not specified but is supposed to be low. Considering that the rubber was not specifically made for micro technology but rather casting of bigger objects the shrinking is probably still quite substantial. Since the prototype does not require any alignment, this is not an issue here but needs to be kept in mind when adapting the process for specific applications.

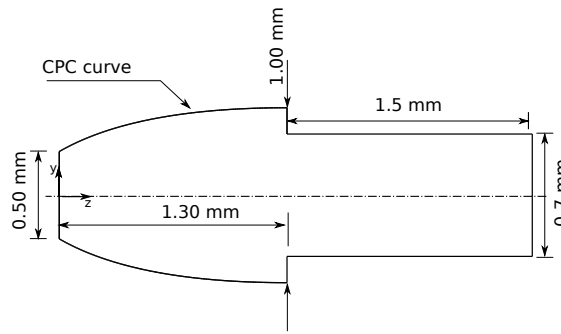


Figure 10.11: Cross section of a single CPC shaped pin. The acceptance angle is 30° and the CPC curve is approximated by 200 points.

Replication of the CPC array in PDMS from the silicone mold was not successful for a variety of reasons. But since the mold is very flexible it is also possible to use a more solid polymer than PDMS for the CPC replica. Successful replications were done with a highly transparent epoxy (EPON™ 825, activated with Jeffamine). EPON™ 825 is a high purity bisphenol A epichlorohydrin epoxy resin with a very low viscosity. See Figure 10.12 for an optical microscope image of the brass master and the highly transparent epoxy replica of an array of axisymmetric CPCs with an acceptance angle of 30° and an exit aperture diameter of 0.5 mm.

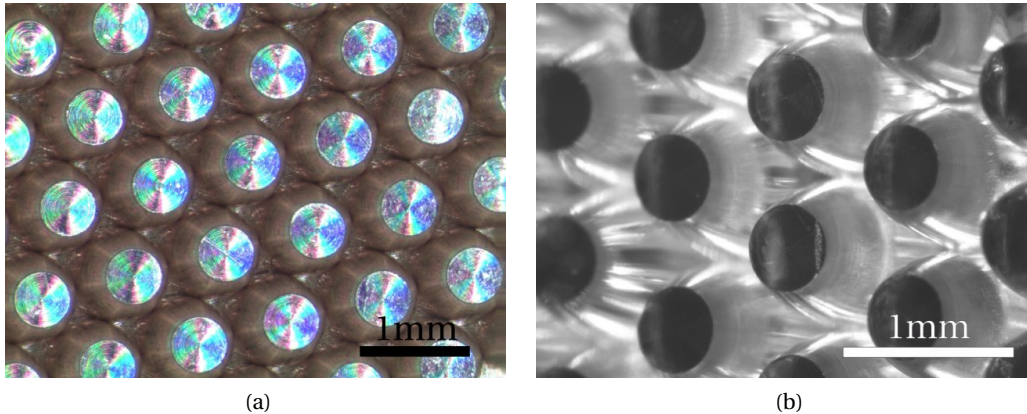


Figure 10.12: Optical microscope images of a miniaturized CPC array with a designed acceptance angle of 30° . (a) is the positive brass master made of an assembly of single CPC shaped brass pins and (b) is the replica in highly transparent epoxy.

The disadvantage of the second process flow over the direct replication of the negative master is that it is impossible to make 2D trough concentrators. In addition the assembly of the master gets very tedious for surfaces bigger than a few square centimeters. On the other hand the replication is not restricted to flexible polymers such as PDMS.

10.4 Characterization and discussion of the result

The optical characterization of the fabricated 2D and 3D CPC arrays is not trivial. The method should depend on the possible application and the relative requirements. For applications in the domain of solar concentration a collimated source with the wavelength spectrum and angular divergence of the sun ($\pm 0.27^\circ$) is usually illuminating the concentrator at different angles and the resulting flux at the exit is measured. Parretta et al. [111] propose an inverse illumination method to easily extract the angular transmission efficiency of a CPC design both in ray tracing simulation and measurement.

In our case a more qualitative but very simple characterization method to show basic features of the system is used. The goal was to investigate the angular intensity distribution at the exit of the CPC array. See Figure 10.13 for an illustration and Figure 10.14 for an image of the setup that was used. Figure 10.15 shows the illuminated CPC array in comparison with the reference PDMS layer. The image is taken from a grazing angle to show that the CPC array transfers the light into high angles.

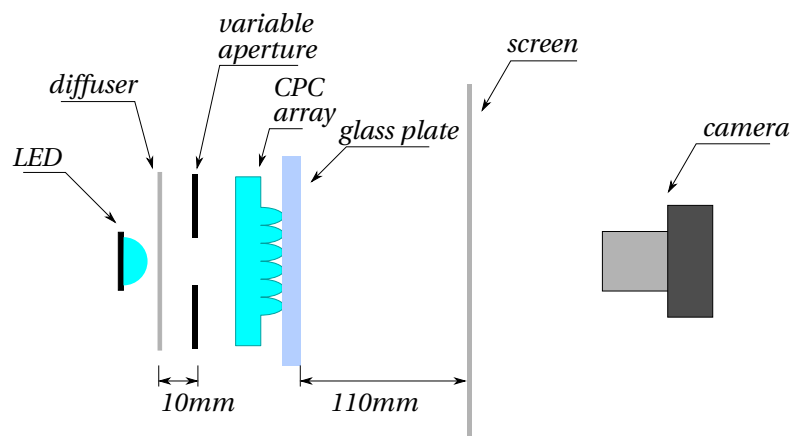


Figure 10.13: Illustration of the illumination and measurement setup.

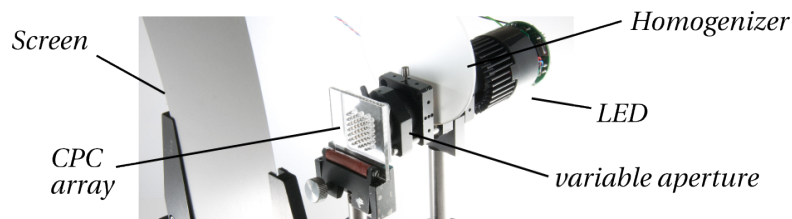


Figure 10.14: Measurement setup for the characterization of the CPC arrays. The light source is a high power white LED. The homogenizer plate is used to make sure that the source is uniform. The variable aperture allows to adjust the angular extent of the source.

The light source was a high power white LED Cree XLamp with a light output up to 1500 lm at 25 W electrical power. The driver circuit and the LED were mounted on a cooling housing with an integrated low vibration ventilator. The LED consists of an array of single emitters

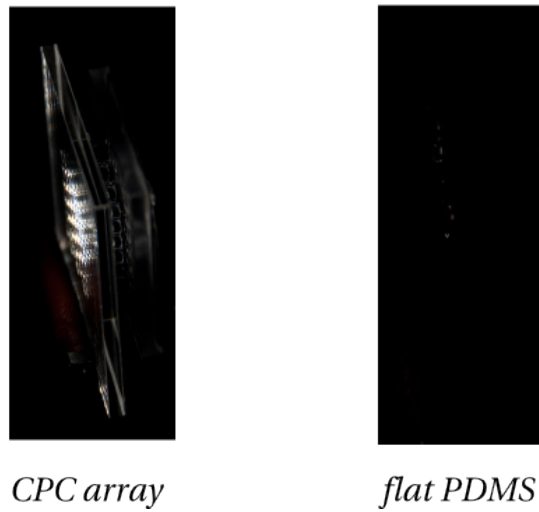


Figure 10.15: Visual comparison between an illuminated CPC array made of PDMS (left) and a flat layer of PDMS with the same thickness as the CPC (right) seen from a grazing angle. It shows how the CPC array transfers the light in angles close to 90°.

that are sealed with a soft polymer dome lens. The source has a nearly Lambertian intensity distribution with 120° FWHM. A diffuser plate was added to smooth the intensity profile and remove intensity variations due to the array of single emitters. The variable aperture with a diameter ranging from 1 mm to 12 mm was used to clip the angular distribution of the source. The CPC array made of soft PDMS was glued to a 2 mm thick glass slide to increase its rigidity. The USB camera (Mightex BCE-B013-U, CMOS, monochrome 8-bit, 1.3 Mpixel) with an 8 mm objective (Thorlabs model MVL8L, $f/1.4$) recorded the intensity distribution on the screen. The exposure time of the camera was always adapted so as not to reach saturation but still use as much of the camera's dynamic range as possible. For the comparison of measured curves they are first normalized with the exposure time.

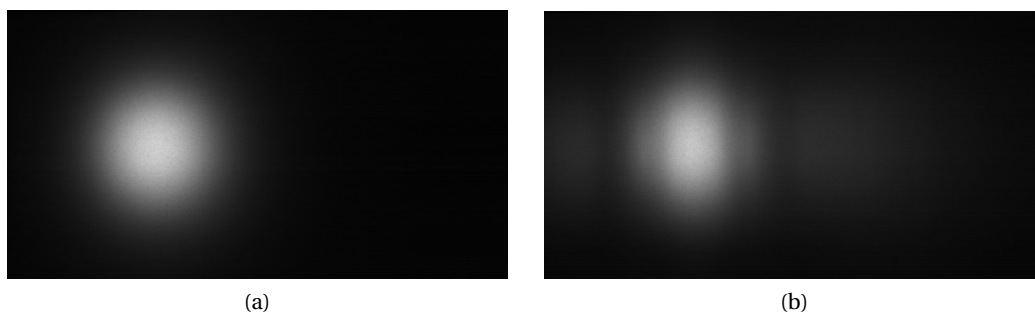


Figure 10.16: Image of the screen illuminated with (a) the reference sample (exposure time 5 ms, aperture diameter 12 mm) and (a) the 2D CPC trough array (exposure time 10 ms, aperture diameter 12 mm)

The reference sample consisted of a glass plate with a flat PDMS layer (“PDMS blank”) of

10.4. Characterization and discussion of the result

the same thickness as the CPC array. This allows to take into account all the losses due to reflections at the different interfaces and absorption inside the materials. Figure 10.16a shows an image of the screen recorded by the USB camera for the reference sample illuminated with the aperture diameter set to 12 mm and Figure 10.16b shows an image of the screen for the fabricated 2D CPC trough array. The aperture for this image is also set to 12 mm.

The intensity is extracted from the images and normalized with the appropriate exposure time to be able to compare the two curves. The x-Axis is scaled according to the setup's geometry to obtain the angle. Figure 10.17a shows several graphs for different illumination apertures and the 2D CPC array. Figure 10.17b shows the same aperture sets but for the reference PDMS blank. Figure 10.17c shows a contrast enhancement factor plot which is defined as the fraction of the intensity of the CPC array divided by the intensity of the reference PDMS blank. This allows an easier extraction of the information about the distribution of intensity relative to the reference sample.

At first the intensity curve for the CPC looks rather disappointing. The spreading of the light into large angles is present but not as strong and uniform as the simulation of the full length dielectric CPC (see Figure 10.5 on Page 69) and the visual observations on Figure 10.14 would make us expect.

Closer investigation reveal several reasons that explain the shape of the curve for the intensity distribution of the dielectric CPC in Figure 10.17a:

1. The source is not filling the acceptance angle completely. The intensity distribution for the reference sample shows that the angle of the source is about $\pm 10^\circ$ instead of the $\pm 24^\circ$ that are needed to fill the acceptance angle completely. This explains the dominance of the intensity around the center and the limitation of the diffusion angle to $\pm 50^\circ$
2. The CPC is truncated from 7.2 mm to 5 mm. This explains the slight valley in the intensity distribution around $\pm 15^\circ$ and also reinforces the intensity around the center.
3. The definition of intensity used for the polar plots is flux/steradian. The measurement with a flat screen is a projection and leads to a certain distortion, especially for the large angles.

The realized compact dielectric CPC arrays presented here serve as a proof of concept for the fabrication of such devices. The measurement of the fabricated devices show that the generic design that was used has the potential but needs to be adapted and modified for specific applications. The fabrication method presented here is not directly suitable for large scale, large volume and low cost industrial manufacturing but rather a proof of concept. Adapting the fabrication process to methods that are more suitable for those requirements, such as injection molding or roll-on imprinting should be possible.

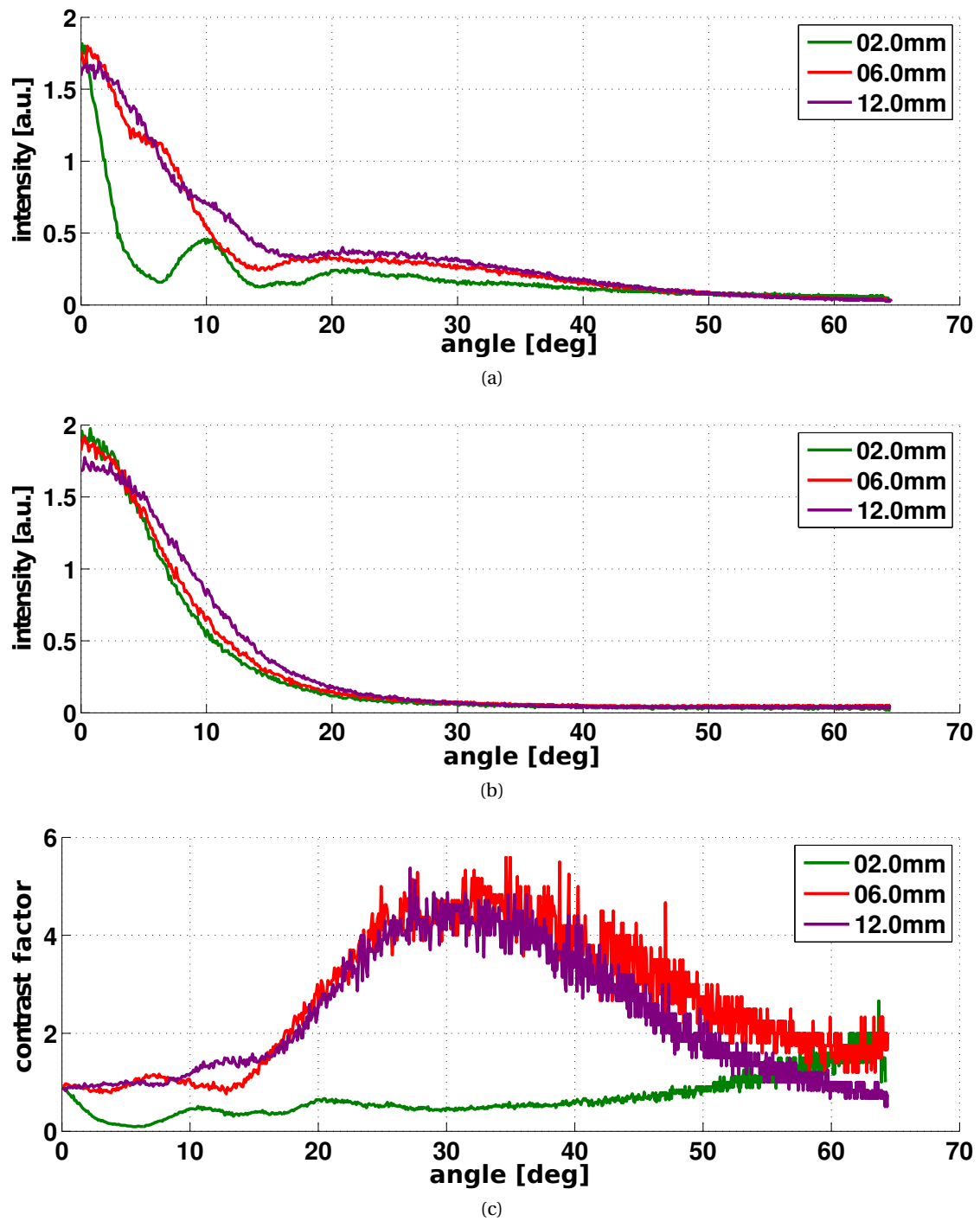


Figure 10.17: Measured angular intensity distribution for (a) the 2D CPC array and (b) the PDMS reference sample with different illumination aperture diameters. (c) shows a contrast enhancement factor plot which is defined as $\frac{I_{CPC}}{I_{PDMS}}$

11 Conclusion

For large angle transformation in a compact form it was necessary to look beyond the microlens array based diffusers discussed in the first part of this thesis. The compact angle transformer based on the compound parabolic concentrator CPC has been retained as a possible alternative.

Possible applications that could profit from a compact array of concentrators were discussed. The possibilities range beside the diffusion of non collimated sources from the chip level collimation of high power LEDs to fiber bundle couplers with a large numerical aperture to improved photovoltaic solar cells with shadowing less reduced series resistance that do not require sun tracking.

The CPC's potential as an angle transformer was investigated by ray tracing simulation and a first prototype of a compact dielectric CPC array with an acceptance angle of 24° and a resulting concentration factor of 3.54 for the 2D trough configuration and 8.7 for the hexagonal array of axisymmetric CPC cones was developed and fabricated. The dimensions of the CPC were 0.5 mm for the exit aperture and a length of 5 mm. The dielectric material used was polydimethylsiloxane (PDMS) with a refractive index of 1.44 in the visible wavelength domain. The replication process relied on precision machined brass forms, either as a direct negative mold or as a positive master.

First measurements confirmed the CPC's angular transformation capabilities but showed at the same time that the design of the prototype that was deliberately kept general must be optimized in order to be of any use for specific applications.

Appendix

A Refractive statistical concave 1D dif- **fusers for laser beam shaping**

R. Bitterli, M. Kim, T. Scharf, H.-P. Herzig, A. Bich, C. Dumouchel, S. Roth, R. Völkel, K. J. Weible

Reproduced from Proc. SPIE 7062, 70620P, Copyright 2008, SPIE

Refractive statistical concave 1D diffusers for laser beam shaping

Roland Bitterli¹, MyunsiK Kim¹, Toralf Scharf¹, Hans-Peter Herzig¹, Andreas Bich²,
Christine Dumouchel², Sylvain Roth², Reinhard Völkel², K.J. Weible²

¹ University of Neuchâtel, Institute of Microtechnology, CH-2000 Neuchâtel, Switzerland

² SUSS MicroOptics SA, CH-2000 Neuchâtel, Switzerland

ABSTRACT

Certain high power laser applications require thin homogeneous laser lines. A possible concept to generate the necessary flat-top profile uses multi-aperture elements followed by a lens to recombine separated beamlets. Advantages of this concept are the independence from entrance intensity profile and achromaticity. However, the periodic structure and the overlapping of beamlets produce interference effects especially when highly coherent light is used. Random optical elements that diffuse only in one direction can reduce the contrast of the interference pattern. Losses due to undesired diffusion in large angles have to be minimized to maintain a good quality and high efficiency of beam shaping. We have fabricated diffusers made of fused silica for a wide range of wavelengths that diffuse only in one direction. Structures are based on an array of concave cylindrical microlenses with locally varying size and position following a well defined statistical distribution. The scattering angle can be influenced by process parameters and is typically between 1° and 60°. To predict the influence of process parameters on the optical properties, a simplified model for the fabrication process and geometrical optics have been used. Characterization of the fabricated devices was done by stylus measurements for the surface shapes, micro-interferometry to measure phase profiles and high resolution goniometry to obtain far field distribution of light. The simulated data compare very well to measured optical properties. Based on our simulation tool we discuss limits of our fabrication method and optimal fabrication parameters.

Keywords: Beam shaping, fused silica, isotropic etching, concave micro structure, micro lens, laser line

1. INTRODUCTION

Thin film transistors (TFTs) are a very important market for laser surface treatment. The amorphous layer of silicon gets annealed with a laser to achieve a lower density of defects and thus better electronic properties.¹ To obtain a good quality and efficient fabrication it is important to have a laser with a line profile with very little intensity variation. A possible concept to generate the necessary flat-top profile uses multi-aperture elements followed by a lens to recombine separated beamlets.² Advantages of this concept are the independence from entrance intensity profile and achromaticity. However, the periodic structure and the overlapping of beamlets produce interference effects especially when highly coherent light is used. Random optical elements that diffuse only in one direction reduce the contrast of the interference pattern. Losses due to undesired diffusion in large angles have to be minimized to maintain a good quality and high efficiency of beam shaping.

In this paper we describe the fabrication and characterization of random optical elements based on concave micro structures. We will treat the fabrication of concave spherical as well as cylindrical micro structures. Especially the latter is of great interest, as it allows to fabricate a 1D diffuser by arranging concave cylindrical micro structures in an array with a certain statistical distribution of their width. As mentioned above, the diffuser should have a narrow diffusion angle (2° to 10° FWHM). In order to guarantee a maximum of homogeneity it is important that the diffuser has no sharp peak of undiffused light, i.e. no zero order. The diffusers presented in this paper based on concave micro optical elements fulfill both requirements. For simplicity we name the concave micro structures microlenses although they do not respect diffraction limited imaging performances.

To predict and optimize the design we present a simulation model based on geometrical optics. This means that the simulation are very rapid at the cost of neglecting diffraction. We will show that for most of the described diffusers this is not an issue.

2. FABRICATION OF CONCAVE MICRO STRUCTURES

Laser surface treatment and similar applications require lasers with a certain amount of power. This limits the choice of material. The devices discussed in this paper were fabricated in fused silica for its good transmission in a wide range of wavelengths.

The principle of fabricating structures in fused silica with a circular cross section is the same as is widely used in micro fluidics:³ the fused silica is isotropically etched through an aperture in an etch stop mask. As mask material we used a 200 nm thick layer of LPCVD poly-Si that was then patterned by photolithography and RIE. As an etchant we use an aqueous solution of 50% hydrofluoric acid (HF) at room temperature.

In order to obtain structures with a circular cross section it is important to use an aperture that is as small as possible while still allowing the etchant access to the material. In an isotropic etch process every point inside the aperture is the center of a circle that is propagating into the material. To simplify the model for the isotropic etch process it can be represented by two circles propagating from the etches of the aperture into the material (see Figures 1-4) with a flat zone with the same dimension as the aperture connecting the two circles. After the etch process is completed with a desired profile, the mask has either fallen off or is removed by KOH.



Figure 1. Fused silica substrate with a patterned poly-Si mask.

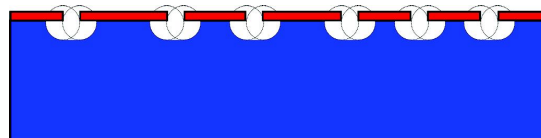


Figure 2. Isotropic etch process: two circles propagate into the substrate connected by a flat at the bottom.

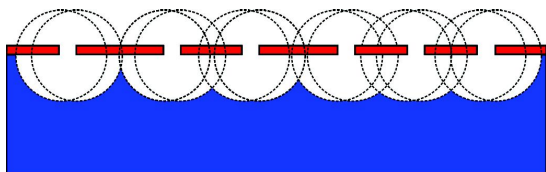


Figure 3. After a certain time the mask is completely under etched. The flat at the bottom becomes less and less important.

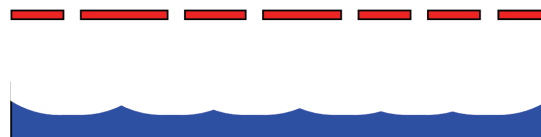


Figure 4. The etch process can be continued to adjust the diffusion angle. The indication of the circles was left out for reasons of clarity.

2.1 Spherical Lens Array

To fabricate an array of spherical microlenses with the technology described above we used a fused silica wafer with a poly-Si mask. The mask was patterned with circular apertures by photolithography and RIE.

The mask parameters for a regular lens array are the diameter of the circular aperture in the mask d and the pitch of the array of apertures P . Together with the etch time the pitch decides on the size of the lens. The diameter of the aperture determines the deviation from the sphere. The smaller the aperture, the less the flat zone at the bottom of the concave lens.

Figure 7 shows an SEM image of a regular spherical lens array seen from a certain angle. The outline of the lenses is square because the etch stop mask has been completely under etched so that the lenses overlap. The mask parameters for a lens array with statistical positions of the lens centers are the diameter of the circular aperture in the mask d , the minimum pitch P_{min} , the fillfactor Q and the statistical distribution σ . Figure 8 and Figure 6 show the result of a fabricated statistical lens array. In Figure 6 we can also see the completely under etched poly-Si etch stop mask with circular apertures. The mask is ruptured and reveals the circular microlenses underneath. If we compare the SEM image of a 2D diffuser fabricated by isotropic etching (Figure 8) with the image of a classical diffuser plate made by sand blasting (Figure 9) we see that the surface morphology is quite different. The advantage of the etched diffuser is that it is possible to engineer the diffusion angle, which is

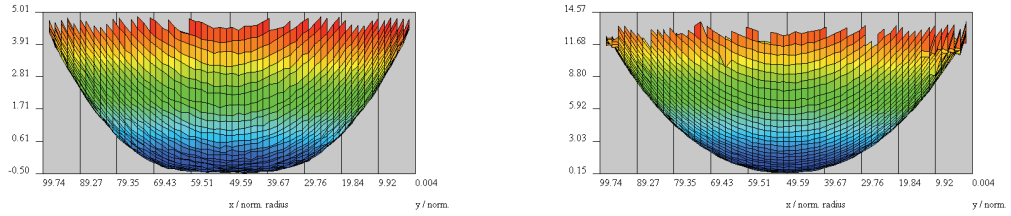


Figure 5. Unwrapped phase from Mach Zehnder micro interferometry measurements to illustrate the influence of the width of the etch aperture on the shape of the structure. The etch aperture of the left image was 10 μm and for the right image 2 μm . The smaller etch aperture results in a better spherical approximation.

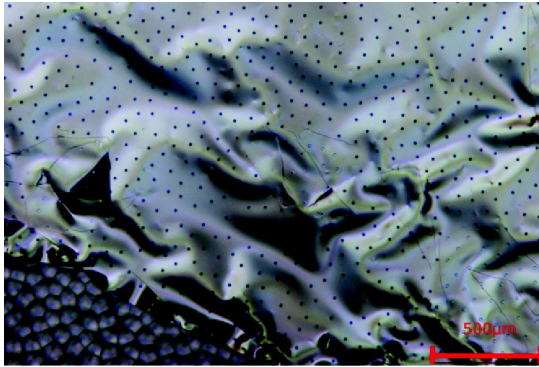


Figure 6. Picture of a 2D diffuser after the isotropic etching. The poly-Si mask is completely under etched and ruptured, revealing the spherical lenses in the lower left corner.

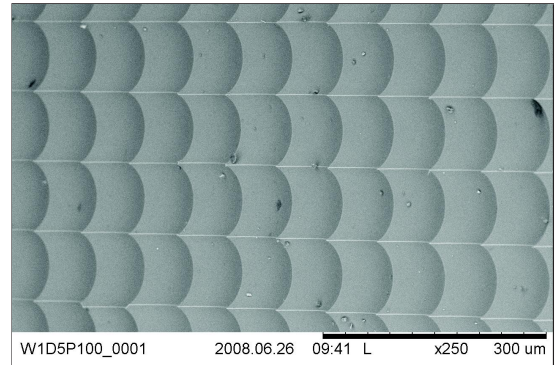


Figure 7. SEM image of a regular array of spherical microlenses seen from a certain inclination. The mask has been completely under etched, all the lenses are overlapping giving the square outline.

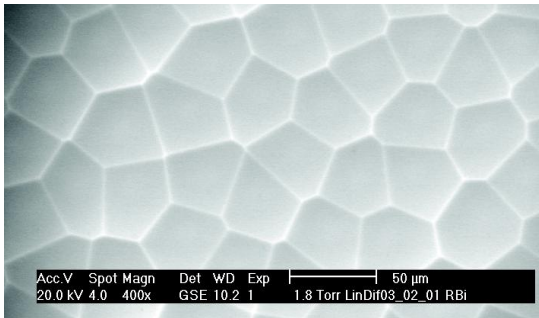


Figure 8. SEM image of a 2D diffuser fabricated by isotropic etching through a hole mask.

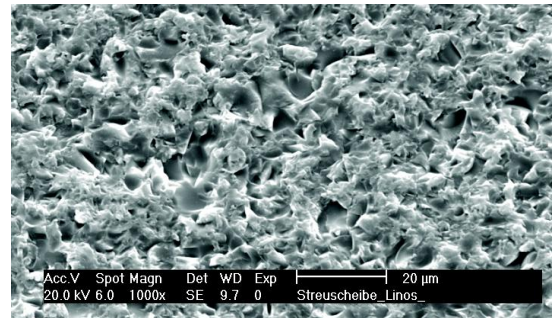


Figure 9. Classical 2D diffuser fabricated by sandblasting (Linos). Note the very sharp structures that tend to scatter light in large angles.

rather difficult for a traditional diffuser made by sand blasting. In addition it is possible with minor changes to the mask concept to generate concave cylindrical lenses with a circular cross section. This allows us to design a diffuser that diffuses only in one direction which is not possible with classical fabrication means such as sand blasting.

3. 1D DIFFUSER

Figure 10 shows the system of a laser line generator with a flat-top profile. The periodic structure of the fly’s eye condenser and the overlapping of beamlets produce interference effects especially for lasers with a long coherence length. To reduce the contrast of the interference pattern we propose to use random optical elements (1D diffuser). Below we will discuss the concept, fabrication and characterization of 1D diffusers based on statistical arrays of cylinder lenses.

3.1 Concept for a 1D Diffuser

The concept we present in this paper for a 1D diffuser is based on a statistical array of cylinder lenses. The above described process based on isotropic etching with an etch mask applies also to the fabrication of concave cylindrical microlens in fused silica. The circular aperture in the etch mask is simply replaced by a slit. Figure 11 shows the mask concept for the isotropic etching of a statistical array of cylindrical microlenses. The gap width W_G between the mask lines is kept constant while the width of the mask lines W_L varies following a certain statistical distribution. For the devices discussed in this paper we use a standard distribution with a mean width \bar{W}_L and a certain standard deviation σ_{W_L} . The width of the gap W_G should be as small as possible to obtain a good approximation of a circular cross section (see 2.1 and Figure 11).

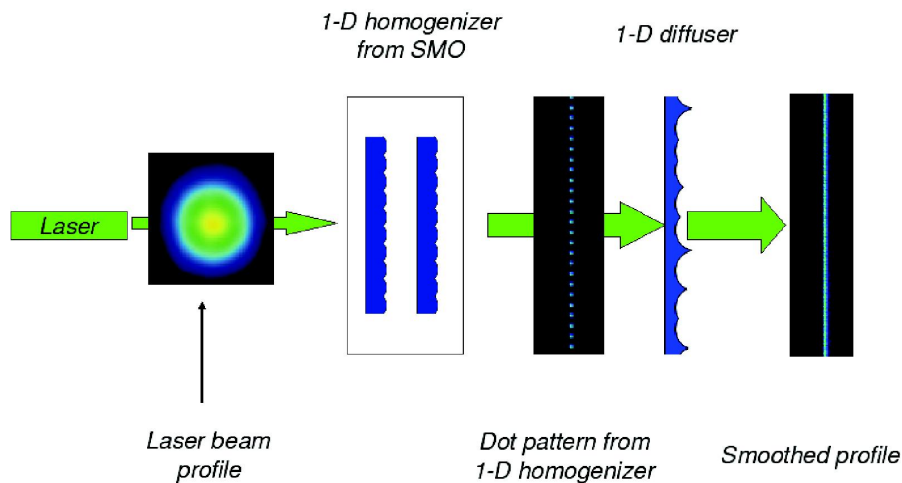


Figure 10. Schematics of an optical system to generate a flat top line. The periodic beam shaping element (fly’s eye condenser and Fourier lens) lead to an interference pattern that is smoothed into a homogeneous line with a 1D diffuser.

In order to achieve small diffusion angles ($2-10^\circ$) it is important that the structures are not too high without narrow angles. This can be done by long etchtimes which result in a large radius of curvature for the lens compared to its width.

3.2 Fabrication

The fabrication relies on 100 mm fused silica wafers with a thickness of 2 mm. The size of a single chip is $30 \times 30 \text{ mm}^2$ allowing for 4 chips per wafer. The mask parameters are listed in Table 1. The gap width W_G is kept constant at $1 \mu\text{m}$ to ensure a good spherical approximation.

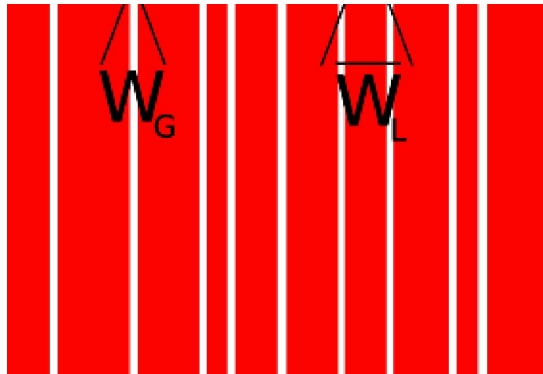


Figure 11. Mask concept for a 1D diffuser based on a statistical array of cylindrical microlenses. The main parameters are the width of the gap W_G , the mean width of the lines \bar{W}_L and the statistical distribution of the line width.

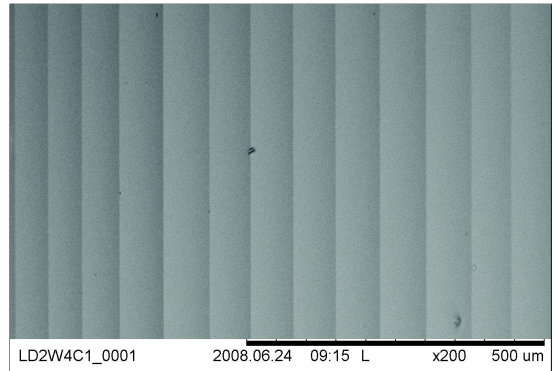


Figure 12. SEM image of a 1D diffuser after etching. The etch mask was completely under etched and has fallen off. The values of the mask parameters are for the gap width $W_G = 1 \mu\text{m}$, for the mean distance $\bar{W}_L = 100 \mu\text{m}$ and the standard deviation of the width $\sigma_{W_L} = 20 \mu\text{m}$.

Table 1. Mask parameters for 1D diffuser chips.

Parameter	Chip 1	Chip 2	Chip 3	Chip 4
Gap width W_G [μm]	1	1	1	1
Mean line width \bar{W}_L [μm]	100	100	200	200
Deviation σ_{W_L} [μm]	20	40	40	80

We use an etch mask made of poly-Si that is deposited by LPCVD on both sides in two flashes of 100 nm thickness to reduce the probability of pin holes in the mask. The mask is then patterned by photolithography and reactive ion etching (RIE). The etch rate with an aqueous solution of HF (49%) varies between 1.5 μm and 2 μm which is consistent with the values from the literature.⁴ In order to have an in-situ control over the advancing of the etch process and compensate the varying etch times, certain test structures have been designed on the wafer that fall off when completely under etched indicating the progress of the etch process. The very long etching times of several hours make it very important that there are no pinholes in the back side poly-Si protection mask. Pinholes lead to cavities in the back side of the wafer that can even pierce through the whole wafer if the etch time is long enough. Increasing the thickness of the poly-Si layer is not possible, because for small gaps in the etch stop mask it is crucial to keep the poly-Si layer relatively thin. Possible solutions would be to apply an additional layer of photoresist or metal to the back or use a wafer chuck.

Figure 13 and Figure 14 show stylus profilometer measurements of 1D diffusers. Figure 13 illustrates the statistical variation in the size of the lenses and also variation in height. Note that the aspect ratio is not equal for convenience, leading to a certain distortion. Figure 14 shows a small portion of Figure 13 but with aspect ratio 1:1 giving an impression of the structures' shallow height profile. The circles are numerically fitted to the data to illustrate the quasi circular shape of the structures.

3.3 Simulation

We use a simple simulation model for the fabrication process and the optical properties to be able to predict angular distribution of the diffused intensity and optimize the design. The model for the fabrication process uses the assumption, that the etch process is perfectly isotropic. As proposed above and illustrated in Figure 1-4 we use two circles that propagate from the edges of the aperture in the mask. The basic parameters are the width of the aperture in the mask and the statistical distribution of the distances between the apertures. The optical part of the simulation relies on geometrical optics using Snell's Law (c.f. eq 1 and Figure 15) as a basis.⁵

$$n_1 \sin \theta_i = n_2 \sin \theta_o \quad (1)$$

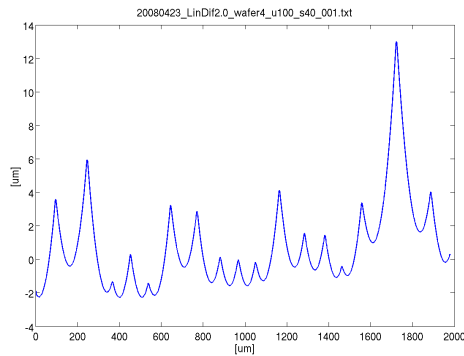


Figure 13. Stylus measurement of a linear diffuser. The random variation of the structures is well visible. Note the distortion due to the aspect ratio of the graph. For a zoom with equal aspect ratio see Figure 14

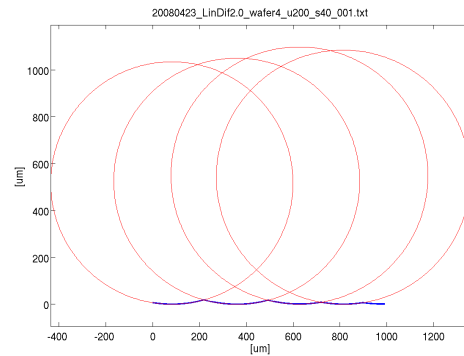


Figure 14. Zoom into the stylus profile graph with an aspect ratio 1:1. The circles are fitted to the graph to illustrate the good circular approximation of the structures.

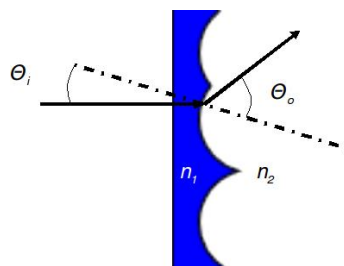


Figure 15. Schematics for the geometrical optics approach for the simulation.

The parameters for the optical simulation are the refractive index n_1 (fused silica), n_2 (air), the number of rays to use for the simulation and the size of the zone to simulate. Due to its restriction to geometrical optics, the model is very fast but lacks all information on diffraction. Comparison between measurement data and simulation show that the model is still fairly precise for feature sizes beyond 100 μm . For feature sizes around 50 μm the difference between the simple model and measured data becomes more noticeable due to diffraction phenomena.

3.4 Measurement

For the characterization of the optical properties of the fabricated 1D diffusers we employ a goniophotometer. The setup (Figure 16) consists of a laser light source (HeNe 632.8 nm, 15 mW, beam diameter 3 mm), a sample holder for the diffuser and a movable detector. The incident beam is perpendicular to the diffuser. The angular resolution of the measurement setup is 0.5°. The important properties that can be extracted from measurement of the intensity's angular distribution are the diffusion angle (FWHM), the uniformity of the diffused intensity and the intensity of the undiffused light (zero order).

Figure 17 and Figure 18 show the measured intensity as a function of diffusion angle together with simulated prediction for the same parameters. Figure 17 shows the measured and simulated data for a 1D diffuser with a mean width of of the structures \overline{W}_L of 100 μm and a standard deviation σ_{W_L} of 40 μm which corresponds to $0.4\overline{W}_L$. The diffusion angle (FWHM) is about 5°. There is no noticeable zero order in the measured data. The visible intensity ripples at the top are probably due to speckles but need more investigation.

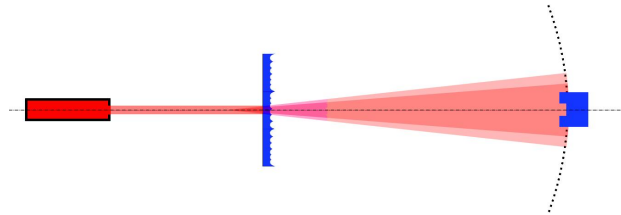


Figure 16. Schematics of the goniophotometer setup. The laser source is a HeNe laser (632.8 nm, 15 mW) with a beam diameter of 3 mm. The detector moves on an arc with its rotation center at the diffuser.

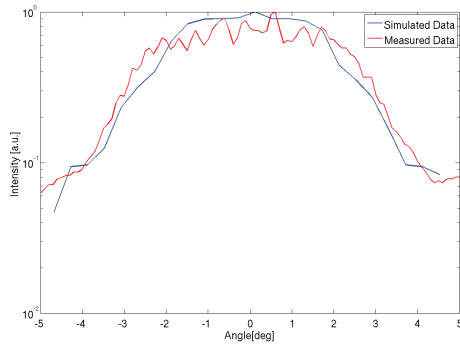


Figure 17. Goniophotometer measurement curve and simulated data for a 1D diffuser with the parameters mean width \overline{W}_L 100 μm , standard deviation σ_{W_L} 40 μm and width of the aperture in the mask W_G 1 μm . The diffusion angle (FWHM) is 5° and we can see that the simulation and measurement correspond well.

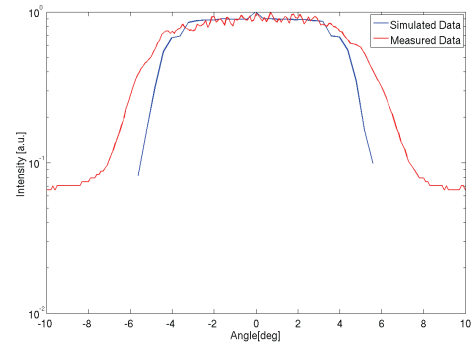


Figure 18. Goniophotometer measurement curve and simulated data for a 1D diffuser with the parameters mean width \overline{W}_L 200 μm , standard deviation σ_{W_L} 80 μm and width of the aperture in the mask W_G 1 μm . The measured diffusion angle (FWHM) is 11° and the simulated diffusion angle is 10°.

Figure 18 shows the data for a diffuser with a doubled mean width \overline{W}_L of 200 μm and a standard deviation σ_{W_L} of 80 μm which means that it is not changed relative to \overline{W}_L compared to the first sample. The diffusion angle also doubled to about 11°. This is due to the fact that wider structures have also a higher profile if etched for the same time as the narrower structure. This leads to a higher NA and thus a wider diffusion angle. In order to further reduce the diffusion angle, it would be necessary to increase the etch time. As we have seen above this necessitates a better protection of the back side to prevent pinholes.

Comparison between measurement and simulation show good agreement in diffusion angle and importance of zero order. Because of the simplicity of the used model it is not possible to reproduce certain intensity variations such as speckles and diffraction effects that are visible in the measured data.

In order to be able to judge the real performance of the presented 1D diffusers for laser flat-top line generation it will be necessary to perform measurements of the entire line generation system (Figure 10). We also plan to build a new goniophotometer setup which allows for a better angular resolution and a more realistic beam size (~ 2 cm).

4. CONCLUSION

A fabrication method for concave micro optical elements made of fused silica has been demonstrated. Fabrication of different elements such as non diffraction limited lens arrays, 2D and 1D diffusers has been shown. In particular 1D diffusers have been investigated in more details. It has been shown that it is possible to fabricate 1D diffusers based on arrays of cylindrical microstructures with a statistical distribution of the structures' width to avoid

grating effects. Goniophotometer measurements have shown that the presented diffusers have a diffusion angle smaller than 10° with a complete suppression of the zero order (specular term). A simulation model to predict the influence of certain fabrication parameters has been presented and compared to measurement data.

ACKNOWLEDGMENTS

The author would like to thank SUSS MicroOptics SA for their close collaboration and the innovation promotion agency KTI/CTI Switzerland for the funding.

REFERENCES

- [1] Miyasaka, M. and Stoemenos, J., "Excimer laser annealing of amorphous and solid-phase-crystallized silicon films," *Journal of Applied Physics* **86**, 5556–5565 (November 1999).
- [2] Schröder, G., [*Technische Optik, Grundlagen und Anwendungen*], Vogel Verlag und Druck (2002).
- [3] Steingoetter, I. and Fouckhardt, H., "Deep fused silica wet etching using an Au-free and stress-reduced sputter-deposited Cr hard mask," *Journal of Micromechanics and Microengineering* **15**, 2130–2135 (2005).
- [4] Williams, K. R. and Muller, R. S., "Etch rates for micromachining processing," *JMEMS* **5**, 256–269 (December 1996).
- [5] Saleh, B. and Teich, M., [*Fundamentals of Photonics*], John Wiley & Sons, inc. (1991).
- [6] Wippermann, F., Zeitner, U.-D., Dannberg, P., Bräuer, A., and Sinzinger, S., "Beam homogenizers based on chirped microlens arrays," *Optics Express* **15**, 6218–6231 (May 2007).

B Fabrication and characterization of linear diffusers based on concave micro lens arrays

R. Bitterli, T. Scharf, H.-P. Herzig, W. Noell, N.F. de Rooij, A. Bich, S. Roth, K. J. Weible, R. Voelkel,
M. Zimmermann, M. Schmidt

Reproduced from Opt. Express 18, 14251-14261, Copyright 2010, Optical Society (OSA)

Fabrication and characterization of linear diffusers based on concave micro lens arrays

Roland Bitterli,^{1,*} Toralf Scharf,¹ Hans-Peter Herzig,¹ Wilfried Noell,² Nico de Rooij,² Andreas Bich,³ Sylvain Roth,³ Kenneth J. Weible,³ Reinhard Voelkel,³ Maik Zimmermann,⁴ and Michael Schmidt⁴

¹Optics and Photonics Technology Laboratory, Ecole Polytechnique Federale de Lausanne, A.-L. Breguet 2, 2000 Neuchâtel, Switzerland

²Sensors, Actuators and Microsystems Laboratory, Ecole Polytechnique Federale de Lausanne, Jaquet Droz 1, 2000 Neuchâtel, Switzerland

³SUSS MicroOptics SA, Jaquet-Droz 7, 2000 Neuchâtel, Switzerland

⁴Bayerisches Laserzentrum GmbH, Erlangen, Germany

*roland.bitterli@epfl.ch

Abstract: We present a new approach of beam homogenizing elements based on a statistical array of concave cylindrical microlens arrays. Those elements are used to diffuse light in only one direction and can be employed together with fly's eye condensers to generate a uniform flat top line for high power coherent light sources. Conception, fabrication and characterization for such 1D diffusers are presented in this paper.

©2010 Optical Society of America

OCIS codes: (140.3300) Laser beam shaping; (220.0220) Optical design and fabrication; (220.4000) Microstructure fabrication; (230.1980) Diffusers; (140.3390) Laser materials processing

References and links

1. M. Miyasaka and J. Stoemenos, "Excimer laser annealing of amorphous and solid-phase-crystallized silicon films," *J. Appl. Phys.* **86**(10), 5556–5565 (1999).
2. G. Schröder, *Technische Optik, Grundlagen und Anwendungen*, (Vogel Verlag und Druck, 2002).
3. R. Bitterli, M. Kim, T. Scharf, H. P. Herzig, A. Bich, C. Dumouchel, S. Roth, R. Voelkel, and K. J. Weible, "Refractive statistical concave 1D diffusers for laser beam shaping," *Proc. SPIE* **7062**, 70620P (2008).
4. I. Steingöetter and H. Fouckhardt, "Deep fused silica wet etching using an Au-free and stress-reduced sputter-deposited Cr hard mask," *J. Micromech. Microeng.* **15**(11), 2130–2135 (2005).
5. H. Zhu, M. Holl, T. Ray, S. Bhushan, and D. R. Meldrum, "Characterization of deep wet etching of fused silica glass for single cell and optical sensor deposition," *J. Micromech. Microeng.* **19**, 065013 (2009).
6. F. Wippermann, U.-D. Zeitner, P. Dannberg, A. Bräuer, and S. Sinzinger, "Beam homogenizers based on chirped microlens arrays," *Opt. Express* **15**(10), 6218–6231 (2007).
7. T. A. Leskova, A. A. Maradudin, E. R. Méndez, and A. V. Shchegrov, "The design and fabrication of one-dimensional random surfaces with specified scattering properties," *Phys. Solid State* **41** (5), 835–841 (1999).
8. M. C. King and D. H. Berry, "Small-angle diffusing screens for photolithographic camera illumination systems," *Appl. Opt.* **11**(11), 2460–2462 (1972).
9. E. R. Méndez, E. E. García-Guerrero, H. M. Escamilla, A. A. Maradudin, T. A. Leskova, and A. V. Shchegrov, "Photofabrication of random achromatic optical diffusers for uniform illumination," *Appl. Opt.* **40**(7), 1098–1108 (2001).
10. N. M. Ganzherli, "Microlens rasters and holographic diffusers based on PFG-01 silver halide photographic material," *J. Opt. Technol.* **76**, 384–387 (2009).
11. J. Albero, L. Nieradko, C. Gorecki, H. Ottevaere, V. Gomez, H. Thienpont, J. Pietarinen, B. Päivänranta, and N. Passilly, "Fabrication of spherical microlenses by a combination of isotropic wet etching of silicon and molding techniques," *Opt. Express* **17**(8), 6283–6292 (2009).

1. Introduction

Laser lines with a uniform intensity profile have many applications. An example would be the use of a high power excimer laser for amorphous silicon annealing for the fabrication of TFT's [1]. To obtain a maximum in throughput and uniformity it is desirable to have a line with a uniform profile. A possible concept to generate the necessary flat-top profile uses multi-aperture elements followed by a lens to recombine separated beamlets [2]. Advantages of this concept are the independence from entrance intensity profile and achromaticity.

However, the periodic structure and the overlapping of beamlets produce interference effects especially when highly coherent light is used. Random optical elements that diffuse only in one direction reduce the contrast of the interference pattern [3]. Losses due to undesired diffusion in large angles have to be minimized to maintain a good quality and high efficiency of beam shaping. For high power applications it is interesting to have concave structures that avoid the formation of undesired hot spots.

There are different fabrication methods for diffusers proposed in literature. They can be divided into two groups: etching of ground glass to obtain 2D diffusers only [8] and “engineered” diffusers that allow also to fabricate 1D diffusers. The engineered diffusers are in general based on holographic [10] or photofabricated [7,9] structures.

In this paper we propose a fabrication method that offers similar degrees of freedom as the engineered diffusers combined with the limited fabrication complexity offered by etching of ground glass. We propose a fabrication process to obtain statistical arrays of concave cylinder micro structures in fused silica that diffuse light only in one direction. For simplicity the concave microstructures are called lenses even though they do not fulfill the requirements for diffraction limited lenses. The fabrication process is based on deep isotropic etching of fused silica in hydrofluoric acid (HF). We propose design rules and fabrication parameters and show their influence on the optical properties of the device. A model for the etch process is proposed that allows to predict the properties of the final device. The devices are characterized with a custom made high precision photogoniometer. More applied characterizations were performed at the Bayerisches Laserzentrum GmbH (blz) Erlangen with an excimer laser.

2. Fabrication process

The fabrication is based on isotropic etching of fused silica in non diluted hydrofluoric acid (HF) 49% at room temperature [4,5]. The observed etch rate lies around 1 μ m/min which corresponds to literature values [5]. Wet etching with unbuffered HF is notoriously irreproducible as far as etch rate goes. It depends on many factors such as temperature, age of the solution, number of wafers already etched etc. Test patterns on the etch mask were implemented to insure that the etch depth and thus the ROC can be guaranteed even with varying etch rates. For the linear diffusers uniformity over the wafer is not an issue. The surface quality of the etched structures is very good and reproducible.

To avoid issues with the wet etch reproducibility it is possible to use a wet etched diffuser with the desired parameters as a master and reproduce it then by a transfer process. Such replication processes are well established and allow a very good reproducibility.

The circular cross section of the cylinder lenses is achieved by isotropic etching through a slit aperture in an etch stop mask. The etch mask is a layer of 600 nm low pressure chemical vapor deposited (LPCVD) poly-Silicon (p-Si). P-Si is an ideal hard mask due to its good adhesion to fused silica, negligible etch rate in HF and more important its hydrophobic surface. This reduces the risk of surface pinholes. To further minimize pinholes the layer is deposited in three steps of 200nm. The mask is patterned by photolithography and reactive ion etching (RIE). Pinholes in the back side poly-Si mask remain a problem since the etch times can be very long (up to 24h). This issue is solved by spinning an additional protective layer of ProTEK A-2 HF protection resist from Brewer Science on the back side.

Double-side polished 4” Fused Silica (Schott Lithosil Q1) wafers with a thickness of 2mm were used as a substrate. During the etch process the mask gets completely under etched and falls off resulting in a 100% fill factor (see Fig. 1). This is quite important since it makes sure that there are no flat regions at the top of the structures which would result in specular transmission of the light and thus an undesired intensity peak in the center of the angular spectrum (zero order).

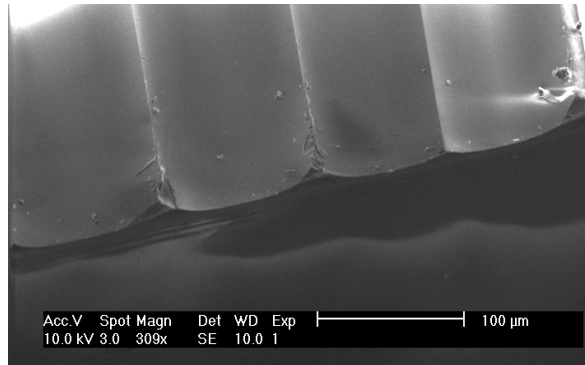


Fig. 1. SEM micrograph of a linear diffuser showing the 100% fill factor of the concave cylindrical lenses and the smooth surface.

Once the etch mask has fallen off, the etch process is continued without the mask to achieve the desired radius of curvature (ROC) of the concave lenses. The maximum etch depth achieved, which is equivalent to the ROC, was 1600 μm . To improve the wetting in the HF bath the wafer is first put 5min in a mixture of a few drops of the detergent Extran[®] (from Merck) in DI water.

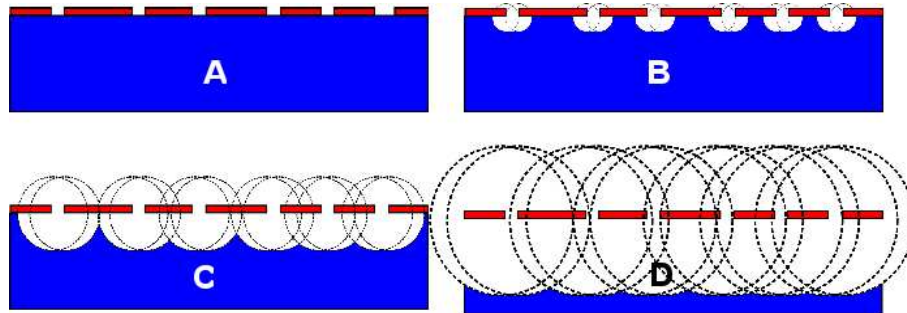


Fig. 2. Schematic representation of the HF etch process. A) Fused silica substrate with a patterned poly-Si etch stop mask. B) Start of the etch process. C) The etch stop mask is completely under etched resulting in 100% fill-factor. D) Continued mask-less etching to adjust the lens' ROC to the desired value. The dotted circles with their respective center at the edges of the mask openings illustrate how the etched surfaces propagate into the substrate.

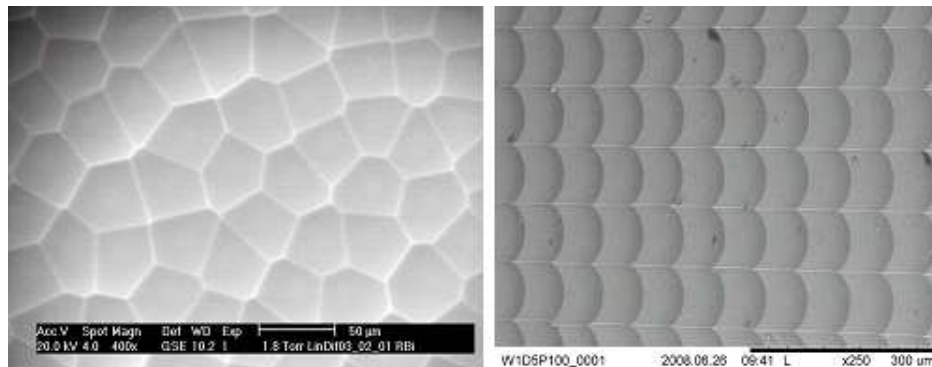


Fig. 3. SEM micrographs of a random 2D diffuser (left) and a regular square lens array (right, seen from a slight angle). The fill factor for both arrangements of concave microlenses is close to 100%.

A perfectly isotropic etch process can be modeled by two circles propagating into the material from the edges of the opening provided by the etch stop. The two circles are joined at the bottom by a flat zone with the dimensions of the etch aperture (see Fig. 2). Since flat zones at the bottom of the lens result in undesired specular transmission it is important to keep the etch opening relatively small compared to the lens width. Etch openings of 1 μ m have proved to be a good compromise for an average lens width of 100-200 μ m. They can still be structured by standard photolithography and RIE, they result in basically no zero order and the whetting in HF is still good especially when enhanced with Extran. As visualized in Fig. 2 under etching leads to fall off of the etch mask when the distance between neighbored etch openings gets equal to the etch depth. Further etching leads to larger radius of curvature without changing position or distance of each element (Fig. 2 D).

The above mentioned fabrication process can of course also be used to fabricate spherical lens arrays and 2D diffusers. The main difference to the fabrication of a linear diffuser is that the slit opening in the mask is replaced by a circular hole. The result is a concave spherical lens array with a fill factor of 100% (see Fig. 3) regardless of the arrangement of the lens array (square, hexagonal, random, etc.). It suffices to etch long enough until the poly-Si mask is completely under etched and all the lenses touch each other. Since the accessible surface for circular openings is much smaller than for slit openings, whetting, etchant transport and as a consequence uniformity are a much bigger issue for spherical than for cylindrical structures. As a consequence of this the etch openings used in literature [11] are much bigger at the cost of a less valid spherical shape.

3. Simulation and design guidelines

In order to develop a certain set of design guidelines for 1D diffusers we used a closed simulation, fabrication, characterization and optimization loop. The fabrication process model allowing to generate realistic profiles of the diffuser with a given set of fabrication and design parameters is based on the assumption of a perfectly isotropic etch process as described above and implemented in Matlab. A typical set of design parameters contains dimension of the chip, average lens width, width variation and the size of the etch opening. For the individual lens width we use a Gaussian normal distribution around a certain mean value and the variation is given as the standard deviation. There is no constraint on the upper or lower limit of the lens width.

The relevant fabrication parameters are the etch rate and etch time resulting in the etch depth which in turn is equivalent to the ROC of the lens. First the positions of the mask openings are defined according to the design parameters. The lens array profile is traced by placing circles at the edges of the mask openings and adding the flat parts where needed (see Fig. 2). The generated profile is then fed into the optical simulation tool. For the optical simulation we used coherent Gaussian ray tracing (FRED from Photon Engineering) as well as a physical optics model where the far field intensity distribution is given by the Fourier transform of the lens array's phase profile. For the physical optics model we used Fraunhofer approximation. The device profile y obtained by the mentioned fabrication model is used to calculate the phase profile with Eq. (1).

$$\phi_a = e^{\frac{2\pi \cdot i(n-1)y}{\lambda}}. \quad (1)$$

The far field intensity is then calculated by taking the Fourier transform of the phase profile. The use of a plane wave approximation is justified since we actually cut the gauss (the raw beam has a diameter of about 30mm, we only use about 8mm). The physical optics simulation resulted in an intensity distribution showing a clearly visible specular transmission peak and the diffusion angle is somewhat larger than the measured values of a real device. Best results were obtained with FRED where the simulated intensity is fairly close to the measured value at the cost of somewhat more time consuming simulation. Figure 4 shows a photo of a section of the intensity pattern generated by a 1D diffuser. The very rapid intensity

variations are clearly visible. Figure 5 shows a section of the simulation with FRED for a device with the same parameters. Clearly visible in Fig. 4 and 5 are the irregular interference pattern in both images due to statistical distributions of phases and speckles.

Figure 6 shows the complete simulated intensity distribution as a function of diffusion angle with a sample frequency of 0.01° . The diffuser parameters are $200\mu\text{m}$ mean lens width, $40\mu\text{m}$ variation and $1500\mu\text{m}$ ROC. In order to evaluate the FWHM diffusion angle and to filter out the non periodic intensity variation we calculate the envelope by convolution with a boxcar function of 100 samples. The simulation indicates that the diffusion angle is given by the ratio lens width over radius of curvature. The smaller this ratio, the smaller is the diffusion angle. There seems to be an upper limit for the diffusion angle of 30° FWHM. The lower limit of the diffusion angle is given by the maximum obtainable lens radius which is defined by technology and by the thickness of the substrate. For a substrate thickness of 2mm the maximum achievable ROC is about $1500\mu\text{m}$. According to simulation this should result in approximately 1° FWHM diffusion angle for lenses with $100\mu\text{m}$ mean width.



Fig. 4. Photo of a section of the intensity distribution for a 1D diffuser showing the non periodic intensity variations.

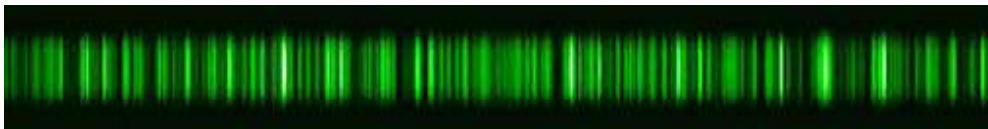


Fig. 5. Simulated intensity distribution for a 1D diffuser. The simulation was done by Gaussian ray tracing (FRED).

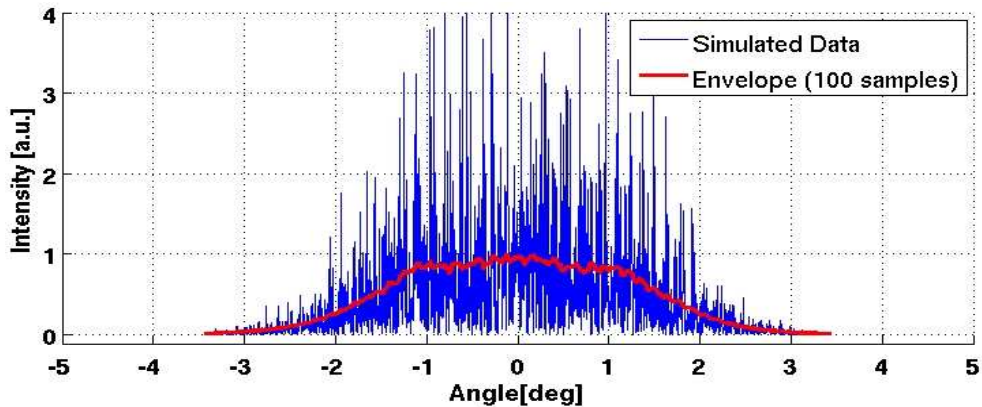


Fig. 6. Cross section of the simulated intensity distribution as seen in Fig. 5. The parameters for the diffuser are $200\mu\text{m}$ mean lens width, $40\mu\text{m}$ lens variation and 1.5mm ROC. The predicted diffusion angle is about 3° FWHM.

As a rough design guideline it is also possible to use the average numerical aperture to calculate the expected diffusion FWHM angle (Fig. 7). The following formula Eq. (2) gives the diffusion angle as a function of average lens width D , refractive index n and ROC:

$$\Theta_{diff} = 2 \arctan \left(\frac{D(n-1)}{2ROC} \right). \quad (2)$$

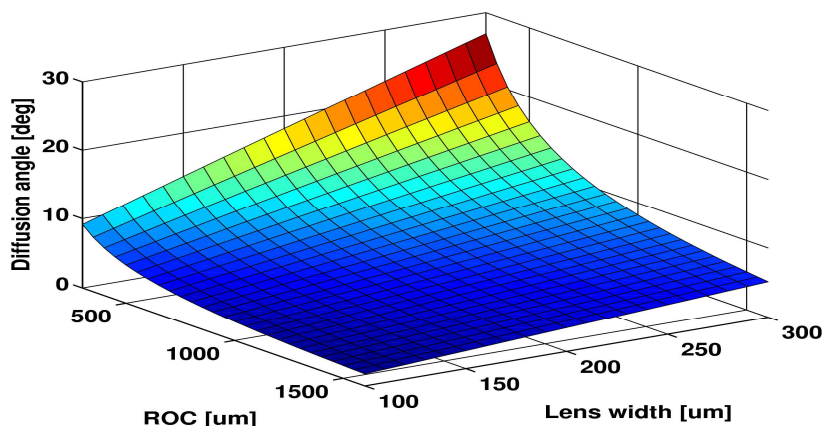


Fig. 7. Expected diffusion angle based on the lens array’s average numerical aperture as a function of lens ROC and average lens width.

4. Inspection and characterization

The surface profile of the fabricated devices was measured with a stylus alpha-step profilometer (KLA Tencor Alpha-Step IQ Surface Profiler). Figure 8 shows surface profiles for two devices with the same average lens width but with different variations. The left profile shows a standard deviation of 20 μm and the right one a standard deviation of 40 μm . As is to be expected the profile with the larger standard deviation is more irregular than the one with the smaller standard deviation.

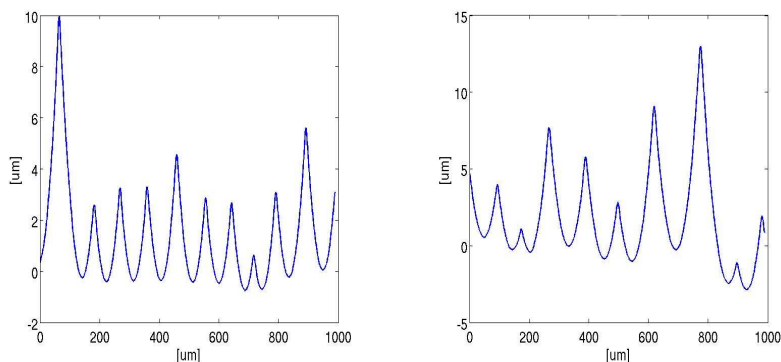


Fig. 8. Surface profiles of 1D diffusers with a mean lens width of 100 μm . The left profile is for a device with standard deviation of 20 μm and the right profile is for a standard deviation of 40 μm . The right profile shows a clear increase in irregularity compared to the left one.

We also used a Mach-Zehnder interferometer to get some information about the surface topography and the form of the lens elements. Figure 9 shows the unwrapped phase of a linear diffuser. Both stylus profilometer Mach-Zehnder interferometry confirmed the isotropic etch model we used above to calculate the profile of the cylindrical lenses (Fig. 10).

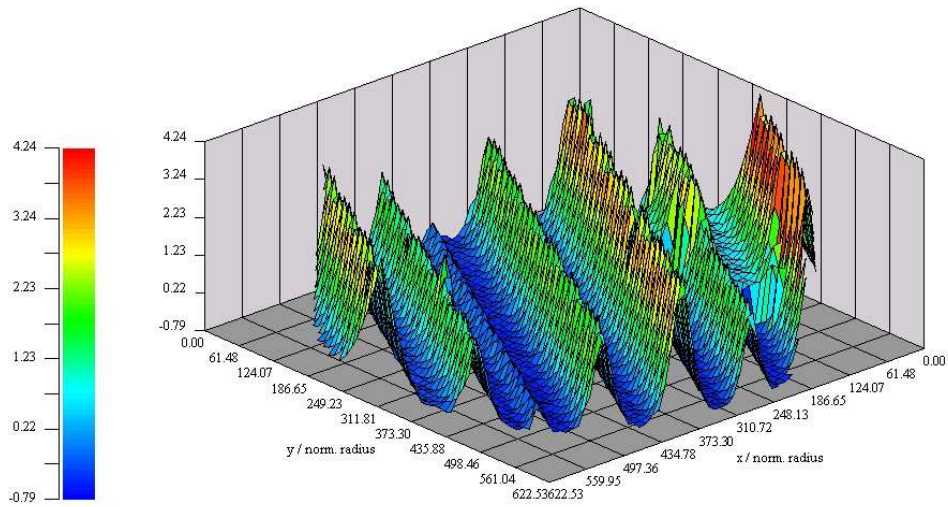


Fig. 9. Unwrapped phase obtained by Mach-Zehnder interferometry showing the surface topography of a linear diffuser.

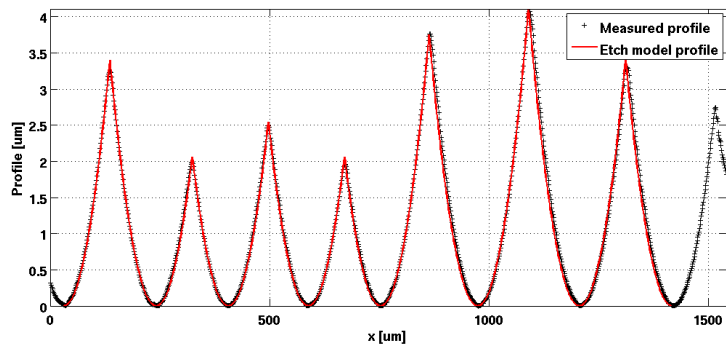


Fig. 10. Baseline corrected measured profile and the simulated profile. The two curves are nearly identical.

The optical properties were measured with a custom made photogoniometer with a particular high angular resolution ($<0.01^\circ$). The measurement system is based on a rotating platform with the laser source, the diffuser sample and a photodetector mounted at a distance of 2m (see Fig. 11). Laser and sample are rotated and the detector has a fixed position. This configuration allows for a high angular resolution at a reasonable mechanical complexity compared with the classical setup where the detector is mounted on an arm that is rotating around the sample. In front of the detector we mounted a pinhole of 0.2mm width to assure that the detector is not introducing any smoothing of the measured intensity. As a source a monomode HeNe laser at 633nm is used. The beam diameter is expanded to about 8mm which means that on average 40 lenses (for 200 μ m lens width) respectively 80 lenses (for 100 μ m lens width) are illuminated.

Angular intensity distributions are shown in Fig. 12-15 for different 1D diffusers. The measurement curve which shows strong non periodic variations (speckles) is superposed with the envelope to simplify the analysis of FWHM angles and the envelope of the simulation of the same device (dashed line). The envelopes are obtained by a linear weighted least square regression of the measured or simulated data. Figure 12 shows the intensity profile for a sample with a mean lens width of 100 μ m, a standard deviation of 20 μ m and a radius of

curvature (ROC) of 1550 μm . The FWHM diffusion angle is 1°. For the same diffuser parameter but with a ROC of 300 μm the FWHM angle is 10° (Fig. 13).

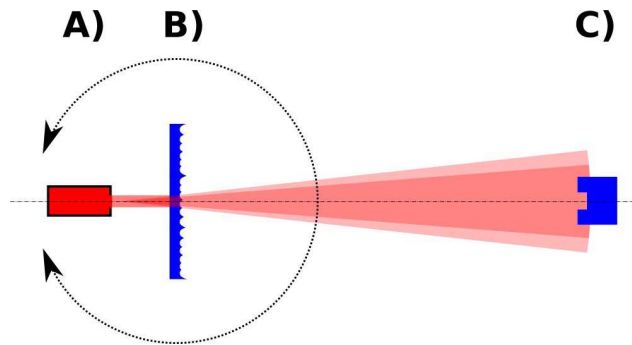


Fig. 11. Schematics of the photogoniometer setup. The Laser source together with a beam expander (A) and the sample (B) is mounted on a rotating table. The photodetector with a pinhole (C) is mounted fix at a distance of 2m.

The measurements confirm that the FWHM angle depends on the ratio of mean lens width over ROC. The steepness of the intensity profile’s flanks is influenced by the variation of the lens width. A larger standard deviation leads to a less steep flank (Fig. 14 and 15).

The comparison of measured with simulated values show that for lenses with a large ROC the simulation result in a slightly larger FWHM diffusion angle whereas for small ROC the simulated FWHM diffusion angle is slightly smaller than the measured value.

The goniophotometer measurements with a monomode laser source showed that the linear diffuser generate a non periodic far field intensity distribution that was also observed by Wippermann et al [6] for chirped fly’s eye condenser based beam homogenizers.

Efficiency measurements showed a transmission efficiency of roughly 92% regardless of diffusion angle and polarization. This is equivalent to the expected transmission efficiency of an uncoated fused silica slide and shows that the diffusing structure do not influence the efficiency. A simple anti-reflection coating for the desired wavelength could increase the efficiency even further.

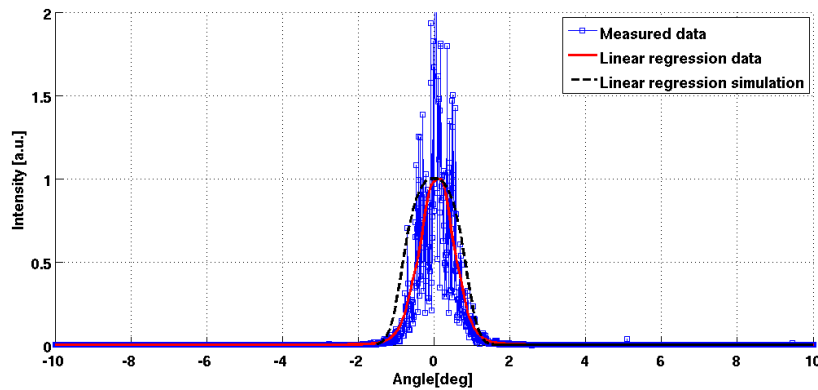


Fig. 12. Intensity distribution for a diffuser with a mean lens width of 100 μm and a variation of 20 μm . The lens ROC is 1500 μm . The measured FWHM diffusion angle is about 1° and the simulated angle is slightly larger.

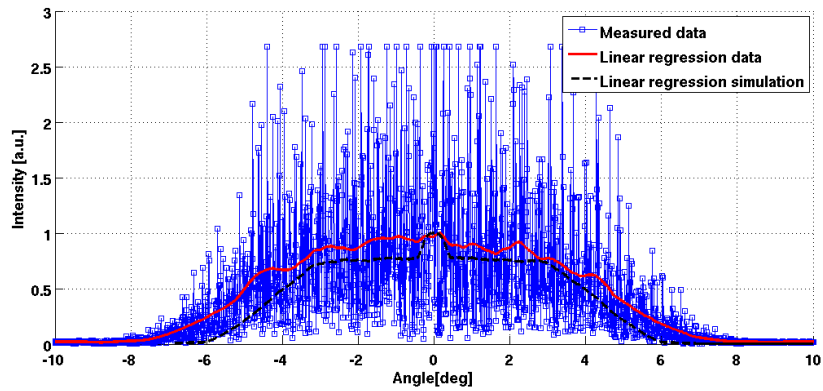


Fig. 13. Intensity distribution for a diffuser with the same parameters as in Fig. 10 but with a ROC of $300\mu\text{m}$. The measured FWHM diffusion angle is about 10° .

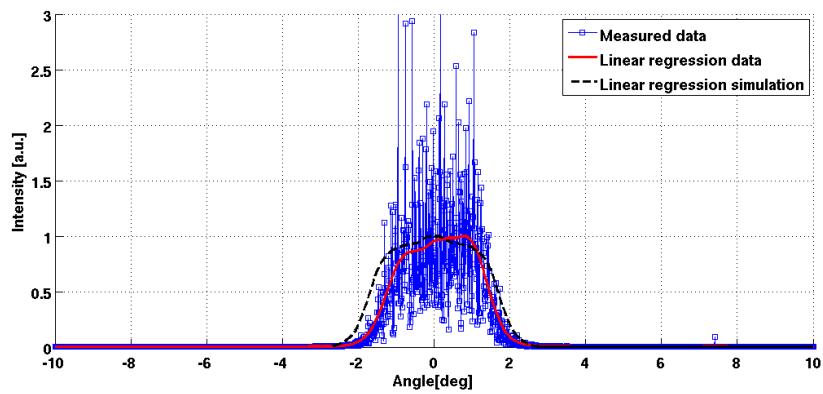


Fig. 14. Intensity distribution for a diffuser with a mean lens width of $200\mu\text{m}$ and a variation of $40\mu\text{m}$. The lens ROC is $1500\mu\text{m}$. The measured FWHM diffusion angle is about 3° which is slightly smaller than the simulated value of about 3.5° .

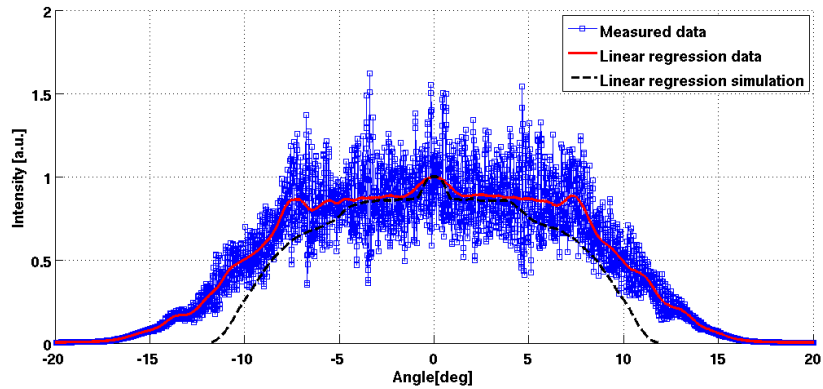


Fig. 15. Intensity distribution for a diffuser with a mean lens width of $200\mu\text{m}$ and a variation of $80\mu\text{m}$. The lens ROC is $300\mu\text{m}$. The measured FWHM diffusion angle is about 20° . The diffusion angle is close to maximum

5. Application

The homogenizing performance of the fabricated linear diffusers was also evaluated with an Excimer laser at the blz in Erlangen, Germany. 10 pulses of 28ns pulse width were applied to a PMMA sample slide. The traces were then inspected with a polarizing optical microscope equipped with Nomarski prism and used in differential interference contrast. This gives a good qualitative impression of the homogeneity of the beam profile.

The laser was a Coherent-Laser ExciStar M-100 ArF Excimer laser at 193 nm with a mean power of up to 12 W, a pulse energy of 120 mJ and a pulse width of 28 ns. The beam dimensions at the exit were 4 mm × 15 mm and the beam divergence 1 mrad × 3 mrad. The setup was composed of a fly's eye condenser based flat top element from SUSS MicroOptics, the random linear diffuser, a field lens and the PMMA slide which serves as target (see Fig. 16).

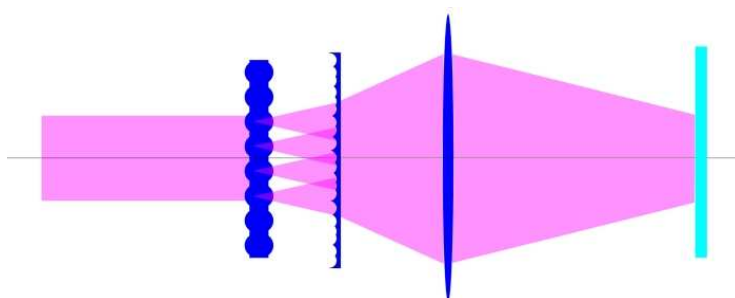


Fig. 16. Schematics of test the setup with an Excimer laser source. From left to right: raw beam, fly's eye condenser flat top element, random linear diffuser, field lens and PMMA target slide at the focus of the field lens.

Figure 17 shows the trace left in the PMMA sample if only the flat top element is used without any linear diffuser. We clearly see the regular diffraction pattern generated by this micro optical element. If we add the linear diffuser after the flat top element (Fig. 18) we see that everything gets smeared out resulting in a smooth profile.

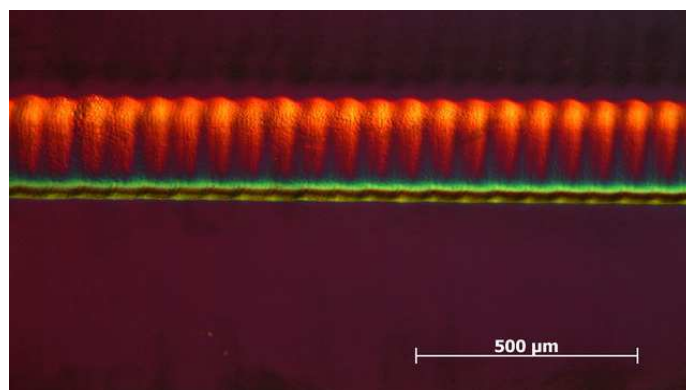


Fig. 17. Trace in a PMMA sample left by an Excimer laser after passing through a flat top element from SUSS MicroOptics. The periodic intensity peaks are clearly visible.

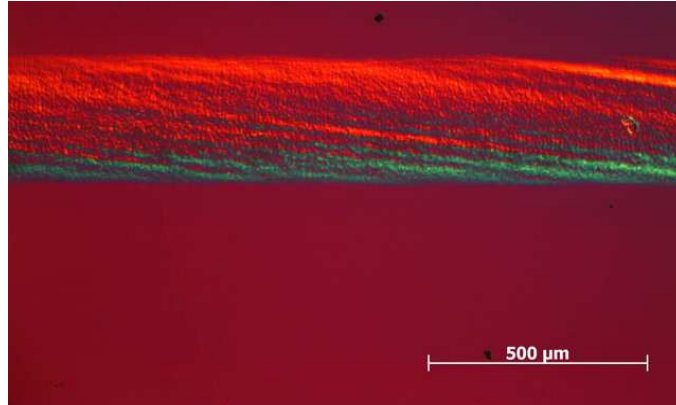


Fig. 18. Trace left in a PMMA sample slide for a fly's eye condenser flat top element combined with a linear diffuser with a diffusion angle of 1° FWHM. Compared to Fig. 17 the intensity is very smooth without any periodic intensity peaks.

6. Conclusion and outlook

In this paper we discussed fabrication, characterization and use of linear diffuser elements based on statistical arrays of concave cylindrical lenses. The linear diffuser allows homogenizing a laser beam in one direction. The choice of fused silica as a material and concave lens structures allow the use of the diffuser in high power laser applications. The diffusion angle depends mainly on the ratio mean lens width over lens ROC. The maximum FWHM angle lies at about 30° and the minimum is limited by the substrate thickness. The linear diffuser composed of a statistical cylindrical lens array generates a non periodic far field intensity distribution without specular transmission peak (zero order). This allows homogenizing the equidistant intensity peaks generated by a fly's eye condenser based flat top element under coherent laser illumination.

A larger range of statistics (type of distribution as well as variation) is currently under investigation to allow a more systematic comparison and study of the influence on the shape of the diffused intensity.

Bibliography

- [1] Mitsutoshi Miyasaka and John Stoemenos. "Excimer laser annealing of amorphous and solid-phase-crystallized silicon films". In: *Journal of Applied Physics* 86.10 (1999), p. 5556. ISSN: 00218979. DOI: 10.1063/1.371560.
- [2] T. Sameshima and S. Usul. "Pulsed laser-induced amorphization of silicon films". In: *Journal of Applied Physics* 70.May 2008 (1991), pp. 1281–1289.
- [3] Holger Muenz, Alois Herkommer, and Rafael Egger. *Optical illumination system for creating a line beam*. 2005.
- [4] Gottfried Schröder. *Technische Optik. Grundlagen und Anwendungen*. Vogel-Vlg., Würzbg., 1998, p. 206. ISBN: 3802317343.
- [5] Roland Bitterli et al. "Refractive statistical concave 1D diffusers for laser beam shaping". In: *Proceedings of SPIE* 7062 (2008), ISSN: 0277786X. DOI: 10.1117/12.793605.
- [6] M C King and D H Berry. "Small-angle diffusing screens for photolithographic camera illumination systems." In: *Applied optics* 11.11 (Nov. 1972), pp. 2460–2. ISSN: 0003-6935.
- [7] Lyle G. Shirley and Nicholas George. "Wide-angle diffuser transmission functions and far-zone speckle". In: *Journal of the Optical Society of America A* 4.4 (Apr. 1987), p. 734. ISSN: 1084-7529.
- [8] L G Shirley and N George. "Diffuser radiation patterns over a large dynamic range. 1: Strong diffusers." In: *Applied optics* 27.9 (May 1988), pp. 1850–61. ISSN: 0003-6935.
- [9] R D Saunders and H J Kostkowski. "Roughened quartz surfaces and Teflon as small angle diffusers and depolarizers between 200 and 400 nm." In: *Applied optics* 28.15 (Aug. 1989), pp. 3242–5. ISSN: 0003-6935.
- [10] Stephen Chakmakjian, G Michael Morris, and Donald J Schertler. "Light Tamers". In: *Photonics Spectra* June (2004).
- [11] N M Ganzherli, I A Maurer, and D F Chernykh. "Microlens rasters and holographic diffusers based on PFG-01 silver halide photographic". In: (2009), pp. 384–387.
- [12] Boaz Salik, Joseph Rosen, and Ammon Yariv. "One-dimensional beam shaping". In: *Journal of the Optical Society of America A* 12.8 (Aug. 1995), p. 1702. ISSN: 1084-7529. DOI: 10.1364/JOSAA.12.001702.

Bibliography

- [13] E. R. Méndez et al. “Design of one-dimensional random surfaces with specified scattering properties”. en. In: *Applied Physics Letters* 81.5 (July 2002), p. 798. ISSN: 00036951. DOI: 10.1063/1.1495900.
- [14] E R Mendez et al. “Photofabrication of random achromatic optical diffusers for uniform illumination.” In: *Applied optics* 40.7 (Mar. 2001), pp. 1098–108. ISSN: 0003-6935.
- [15] Fred M. Dickey and Scott C. Holswade. *Laser Beam Shaping: Theory and Techniques*. CRC Press, 2000, p. 428.
- [16] Fred M. Dickey, Scott C. Holswade, and David L. Shealy. *Laser Beam Shaping Applications*. CRC Press, 2005, p. 357.
- [17] Fred M. Dickey. “Laser beam shaping techniques”. In: *Proceedings of SPIE* (2000), pp. 338–348. ISSN: 0277786X. DOI: 10.1117/12.407361.
- [18] Zheng Zhenrong, Hao Xiang, and Liu Xu. “Freeform surface lens for LED uniform illumination.” In: *Applied optics* 48.35 (Dec. 2009), pp. 6627–34. ISSN: 1539-4522.
- [19] Mikhail a Moiseev, Leonid L Doskolovich, and Nikolay L Kazanskiy. “Design of high-efficient freeform LED lens for illumination of elongated rectangular regions.” In: *Optics express* 19 Suppl 3.May (May 2011), A225–33. ISSN: 1094-4087.
- [20] C Dorrer. “High-damage-threshold beam shaping using binary phase plates.” In: *Optics letters* 34.15 (Aug. 2009), pp. 2330–2. ISSN: 0146-9592.
- [21] Robert W. Cohn et al. “Fully complex diffractive optics by means of patterned diffuser arrays:encoding concept and implications for fabrication”. In: *Journal of the Optical Society of America A* 14.5 (May 1997), p. 1110. ISSN: 1084-7529. DOI: 10.1364/JOSAA.14.001110.
- [22] Cheng-Huan Chen, Chien-Chuan Chen, and Wei-Chien Liang. “Light Pipe Line Beam Shaper”. In: *Optical Review* 14.4 (July 2007), pp. 231–235. ISSN: 1340-6000. DOI: 10.1007/s10043-007-0231-x.
- [23] Norbert Lindlein et al. “Flexible beam shaping system using fly’s eye condenser.” In: *Applied optics* 49.12 (Apr. 2010), pp. 2382–90. ISSN: 1539-4522.
- [24] A. Bich et al. “Multifunctional micro-optical elements for laser beam homogenizing and beam shaping”. In: *Proceedings of SPIE* 6879 (2008), ISSN: 0277786X. DOI: 10.1117/12.762923.
- [25] Maik Zimmermann et al. “Refractive Micro-optics for Multi-spot and Multi-line Generation”. In: *Proceedings of LPM2008-the 9th International Symposium on Laser Precision Microfabrication* (2008), pp. 1–5.
- [26] Sebastian Pfadler et al. “Application of a beam homogenizer to planar laser diagnostics.” In: *Optics express* 14.22 (Oct. 2006), pp. 10171–80. ISSN: 1094-4087.
- [27] Reinhard Voelkel and Kenneth J. Weible. “Laser beam homogenizing: limitations and constraints”. In: *Proceedings of SPIE* 7102 (2008), ISSN: 0277786X. DOI: 10.1117/12.799400.

- [28] Frank Wippermann. “Chirped refractive microlens arrays Dissertation zur Erlangung des akademischen Grades”. PhD thesis. 2007.
- [29] Frank Wippermann et al. “Beam homogenizers based on chirped microlens arrays.” In: *Optics express* 15.10 (May 2007), pp. 6218–31. ISSN: 1094-4087.
- [30] F. C. Wippermann et al. “Improved homogenization of fly’s eye condenser setups under coherent illumination using chirped microlens arrays”. In: *Proceedings of SPIE* 6466 (2007), ISSN: 0277786X. DOI: 10.1117/12.700127.
- [31] Roland Bitterli et al. “Fabrication and characterization of linear diffusers based on concave micro lens arrays”. In: *Optics Express* 18.13 (June 2010), p. 14251. ISSN: 1094-4087. DOI: 10.1364/OE.18.014251.
- [32] Joseph W. Goodman. *Speckle Phenomena in Optics: Theory and Applications*. Roberts and Company Publishers, 2007, p. 387. ISBN: 0974707791.
- [33] J. Masson et al. “Tunable MEMS-based optical linear (1D) diffusers for dynamic laser beam shaping and homogenizing”. In: *2009 IEEE/LEOS International Conference on Optical MEMS and Nanophotonics*. IEEE, 2009, pp. 129–130. DOI: 10.1109/OMEMS.2009.5338551.
- [34] Jonathan Masson et al. “Tunable optical diffusers for high-power laser applications based on magnetically actuated membranes”. In: *2010 International Conference on Optical MEMS and Nanophotonics*. IEEE, Aug. 2010, pp. 61–62. ISBN: 978-1-4244-8926-8. DOI: 10.1109/OMEMS.2010.5672185.
- [35] G. A. C. M. Spierings. “Wet chemical etching of silicate glasses in hydrofluoric acid based solutions”. In: *Journal of Materials Science* 28.23 (Dec. 1993), pp. 6261–6273. ISSN: 0022-2461. DOI: 10.1007/BF01352182.
- [36] Joseph W. Goodman. *Introduction to Fourier optics*. McGraw-Hill, 1996, p. 441. ISBN: 0071142576.
- [37] Hans Peter Herzig. *Micro-Optics: Elements, Systems And Applications*. CRC Press, 1997, p. 359. ISBN: 0748404813.
- [38] Jacques Arnaud. “Representation of Gaussian beams by complex rays”. In: *Applied Optics* 24.4 (Feb. 1985), p. 538. ISSN: 0003-6935. DOI: 10.1364/AO.24.000538.
- [39] D. Dominé et al. “Modeling of light scattering from micro- and nanotextured surfaces”. In: *Journal of Applied Physics* 107.4 (2010), p. 044504. ISSN: 00218979. DOI: 10.1063/1.3295902.
- [40] Patrick Ruffieux et al. “Two step process for the fabrication of diffraction limited concave microlens arrays.” In: *Optics express* 16.24 (Nov. 2008), pp. 19541–9. ISSN: 1094-4087.
- [41] Miao He et al. “Fabrication of concave refractive microlens arrays in solgel glass by a simple proximity-effect-assisted reflow technique”. In: *Optics Letters* 29.9 (May 2004), p. 1007. ISSN: 0146-9592. DOI: 10.1364/OL.29.001007.

Bibliography

- [42] FHS Lin et al. "Fabrication of binary microlens array by excimer laser micromachining". In: *Proceedings of 3511*. September (1998), pp. 67–72.
- [43] Chunlei Du et al. "Profile control technology for high-performance microlens array". In: *Optical Engineering* 43.11 (Nov. 2004), p. 2595. ISSN: 00913286. DOI: 10.1117/1.1805563.
- [44] Feng Chen et al. "Maskless fabrication of concave microlens arrays on silica glasses by a femtosecond-laser-enhanced local wet etching method". In: *Optics Express* 18.19 (2010), pp. 467–470.
- [45] C.S. Lim et al. "Fabrication of concave micro lens array using laser patterning and isotropic etching". In: *International Journal of Machine Tools and Manufacture* 46.5 (Apr. 2006), pp. 552–558. ISSN: 08906955. DOI: 10.1016/j.ijmachtools.2005.06.004.
- [46] Xiangming Li et al. "Fabrication of concave microlens arrays using controllable dielectrophoretic force in template holes." In: *Optics letters* 36.20 (Oct. 2011), pp. 4083–5. ISSN: 1539-4794.
- [47] Changyi Lai and Vitor M Schneider. "Arbitrary shaped microlens array laser sintered on glass sheets." In: *Applied optics* 48.35 (Dec. 2009), pp. 6621–6. ISSN: 1539-4522.
- [48] D. Martin Knotter. "Etching Mechanism of Vitreous Silicon Dioxide in HF-Based Solutions". In: *Journal of the American Chemical Society* 122.18 (May 2000), pp. 4345–4351. ISSN: 0002-7863. DOI: 10.1021/ja993803z.
- [49] Haixin Zhu et al. "Characterization of deep wet etching of fused silica glass for single cell and optical sensor deposition". In: *Journal of Micromechanics and Microengineering* 19.6 (June 2009), p. 065013. ISSN: 0960-1317. DOI: 10.1088/0960-1317/19/6/065013.
- [50] K.R. Williams and R.S. Muller. "Etch rates for micromachining processing". In: *Journal of Microelectromechanical Systems* 5.4 (1996), pp. 256–269. ISSN: 10577157. DOI: 10.1109/84.546406.
- [51] M Wagner, H D Geiler, and D Wolff. "High-performance laser beam shaping and homogenization system for semiconductor processing". In: 1 (1990), pp. 1193–1201.
- [52] Eugene Hecht. *Optics*. 4th. Addison Wesley, 2002.
- [53] Shintaro Kawata et al. "Spatial coherence of KrF excimer lasers". In: *Applied Optics* 31.3 (Jan. 1992), p. 387. ISSN: 0003-6935. DOI: 10.1364/AO.31.000387.
- [54] Wolfgang Singer et al. "Diffractive beamshaping elements at the fabrication limit". In: *Optical Engineering* 35.10 (1996), pp. 2779–2787.
- [55] H. Hinterberger. "Efficient Light Coupler for Threshold Cerenkov Counters". In: *Review of Scientific Instruments* 37.8 (1966), p. 1094. ISSN: 00346748. DOI: 10.1063/1.1720428.
- [56] Roland Winston. "Light Collection within the Framework of Geometrical Optics". In: *Journal of the Optical Society of America* 60.2 (Feb. 1970), p. 245. ISSN: 0030-3941. DOI: 10.1364/JOSA.60.000245.

- [57] Roland Winston. "Principles of solar concentrators of a novel design". In: *Solar Energy* 16.2 (Oct. 1974), pp. 89–95. ISSN: 0038092X. DOI: 10.1016/0038-092X(74)90004-8.
- [58] A. Rabl, N.B. Goodman, and R. Winston. "Practical design considerations for CPC solar collectors". In: *Solar Energy* 22.4 (Jan. 1979), pp. 373–381. ISSN: 0038092X. DOI: 10.1016/0038-092X(79)90192-0.
- [59] J. H. Atwater et al. "Microphotonic parabolic light directors fabricated by two-photon lithography". In: *Applied Physics Letters* 99.15 (2011), p. 151113. ISSN: 00036951. DOI: 10.1063/1.3648115.
- [60] W. T. Welford and R. Winston. *High collection nonimaging optics*. 1st. New York: Academic Press, 1989. ISBN: 0127428852.
- [61] Roland Winston et al. *Nonimaging optics*. Academic Press, 2005, p. 497. ISBN: 0127597514.
- [62] Harald Ries and Ari Rabl. "Edge-ray principle of nonimaging optics". In: *Journal of the Optical Society of America A* 11.10 (Oct. 1994), p. 2627. ISSN: 1084-7529. DOI: 10.1364/JOSAA.11.002627.
- [63] P. a. Davies. "Edge-ray principle of nonimaging optics". In: *Journal of the Optical Society of America A* 11.4 (Apr. 1994), p. 1256. ISSN: 1084-7529. DOI: 10.1364/JOSAA.11.001256.
- [64] Julio Chaves. "Introduction to Nonimaging Optics". In: *New York. Optical Science and Engineering* 20080522 (May 2008). DOI: 10.1201/9781420054323.
- [65] N. B. Goodman et al. "Solid-dielectric compound parabolic concentrators: on their use with photovoltaic devices." In: *Applied optics* 15.10 (Oct. 1976), pp. 2434–6. ISSN: 0003-6935.
- [66] X Ning, R Winston, and J O'Gallagher. "Dielectric totally internally reflecting concentrators." In: *Applied optics* 26.2 (Jan. 1987), pp. 300–5. ISSN: 0003-6935.
- [67] Jack A Soules et al. "Design and Fabrication of a Dielectric Total Internal Reflecting Solar Concentrator and Associated Flux Extractor for Extreme High Temperature (2500K) Applications". In: November (1997).
- [68] Ari Rabl and Roland Winston. "Ideal concentrators for finite sources and restricted exit angles." In: *Applied optics* 15.11 (Nov. 1976), pp. 2880–3. ISSN: 0003-6935.
- [69] Jin-gang Liu and Mitsuru Ueda. "High refractive index polymers: fundamental research and practical applications". en. In: *Journal of Materials Chemistry* 19.47 (2009), p. 8907. ISSN: 0959-9428. DOI: 10.1039/b909690f.
- [70] R. S. Scharlack. "All-dielectric compound parabolic concentrator". In: *Applied Optics* 16.10 (Oct. 1977), p. 2601. ISSN: 0003-6935.
- [71] J.H. Lee, W. Chang, and D. Choi. "LED Light Coupler Design for a Ultra Thin Light Guide". In: *Journal of the Optical Society of Korea* 11.3 (Sept. 2007), pp. 113–117.
- [72] Donald E. Williamson. "Cone Channel Condenser Optics". In: *Journal of the Optical Society of America* 42.1949 (1952), pp. 712–715.

Bibliography

- [73] Sergey Kudaev. “Automated optimization of non-imaging optics for luminaries”. In: *Proceedings of SPIE* (2005), ISSN: 0277786X. DOI: 10.1117/12.625379.
- [74] Harald Ries and Julius Muschaweck. “Tailored freeform optical surfaces.” In: *Journal of the Optical Society of America. A, Optics, image science, and vision* 19.3 (Mar. 2002), pp. 590–5. ISSN: 1084-7529.
- [75] Silvano Donati, Giuseppe Martini, and Michele Norgia. “Microconcentrators to recover fill-factor in image photodetectors with pixel on-board processing circuits.” In: *Optics express* 15.26 (Dec. 2007), pp. 18066–75. ISSN: 1094-4087.
- [76] C. Novero. “On a nonimaging optics approach to diode lasers collimation”. In: *Conference on Precision Electromagnetic Measurements. Conference Digest. CPEM 2000 (Cat. No.00CH37031)*. IEEE, pp. 269–270. ISBN: 0-7803-5744-2. DOI: 10.1109/CPEM.2000.850980.
- [77] Dejan Grabovičkić, Pablo Benítez, and Juan C. Miñano. “TIR RXI collimator”. In: *Optics Express* 20.S1 (Dec. 2011), A51. ISSN: 1094-4087. DOI: 10.1364/OE.20.000A51.
- [78] M.a. Moiseev and L.L. Doskolovich. “Design of refractive spline surface for generating required irradiance distribution with large angular dimension”. In: *Journal of Modern Optics* 57.7 (Apr. 2010), pp. 536–544. ISSN: 0950-0340. DOI: 10.1080/09500341003764069.
- [79] Oliver Dross et al. “Review of SMS Design Methods and Real World Applications”. In: *Nonimaging Optics and Efficient Illumination Systems*. Ed. by Roland Winston and R. John Koschel. Proceedings of the SPIE, 2004, pp. 35–47.
- [80] Oliver Dross. “LED headlight architecture that creates a high quality beam pattern independent of LED shortcomings”. In: *Proceedings of SPIE* (2005), ISSN: 0277786X. DOI: 10.1117/12.624658.
- [81] Oliver Dross et al. “Non-imaging optics combine LEDs into one bright source”. In: *SPIE Newsroom* (2006), pp. 2–4. ISSN: 18182259. DOI: 10.1117/2.1200605.0197.
- [82] Sergey Kudaev and Peter Schreiber. “Parametric design of non-imaging collimators”. In: *Proceedings of SPIE* (2006), ISSN: 0277786X. DOI: 10.1117/12.692269.
- [83] Juan C. Miñano, Juan C Gonzalez, and Pablo Benítez. “A high gain, compact, non-imaging concentrator : RXI”. In: 34.34 (1995), pp. 7850–7856.
- [84] Yi Ding et al. “Freeform LED lens for uniform illumination.” In: *Optics express* 16.17 (Aug. 2008), pp. 12958–66. ISSN: 1094-4087.
- [85] Janis Spigulis. “Compact dielectric reflective radially emitted light”. In: *Applied Optics* 33.25 (1994), pp. 5970–5974.
- [86] Pablo Benítez et al. “Simultaneous multiple surface optical design method in three dimensions”. In: *Optical Engineering* 43.7 (2004), p. 1489. ISSN: 00913286. DOI: 10.1117/1.1752918.
- [87] K. Thyagarajan, Anurag Sharma, and A. K. Ghatak. “Efficient coupling of incoherent light into optical fibers and bundles”. In: *Applied optics* 18.5 (Mar. 1979), pp. 2416–2419. ISSN: 0003-6935.

- [88] F. Nakamaru, Y. Matsumoto, and a. Nakazono. "Novel high-efficiency concentrator for optical fiber communication". In: *IEEE Photonics Technology Letters* 14.7 (July 2002), pp. 953–955. ISSN: 1041-1135. DOI: 10.1109/LPT.2002.1012396.
- [89] M Hein et al. "Characterisation of a 300x photovoltaic concentrator system with one-axis tracking". In: 75 (2003), pp. 277–283.
- [90] A. Mohr et al. "Silicon concentrator cells in an one-axis tracking concentrator system with a concentration ratio of 300x". In: *Conference Record of the Thirty-first IEEE Photovoltaic Specialists Conference, 2005*. IEEE, 2005, pp. 639–642.
- [91] Seri Lee. "Thermal challenges and opportunities in concentrated photovoltaics". In: *2010 12th Electronics Packaging Technology Conference*. IEEE, Dec. 2010, pp. 608–613.
- [92] James R. Bolton. "Solar cells - A technology assessment". In: *Solar Energy* 31.5 (Jan. 1983), pp. 483–502. ISSN: 0038092X. DOI: 10.1016/0038-092X(83)90052-X.
- [93] A. Terao et al. "A mirror-less design for micro-concentrator modules". In: *Conference Record of the Twenty-Eighth IEEE Photovoltaic Specialists Conference - 2000 (Cat. No.00CH37036)*. IEEE, pp. 1416–1419.
- [94] Antonio Luque and Steven Hegedus, eds. *Handbook of Photovoltaic Science*. second edi. John Wiley and Sons, Ltd., 2011. ISBN: 9780470721698.
- [95] Kensuke Nishioka et al. "Evaluation of InGaP/InGaAs/Ge triple-junction solar cell and optimization of solar cell's structure focusing on series resistance for high-efficiency concentrator photovoltaic systems". In: *Solar Energy Materials and Solar Cells* 90.9 (May 2006), pp. 1308–1321. ISSN: 09270248. DOI: 10.1016/j.solmat.2005.08.003.
- [96] R Miles, G Zoppi, and I Forbes. "Inorganic photovoltaic cells". In: *Materials Today* 10.11 (Nov. 2007), pp. 20–27. ISSN: 13697021. DOI: 10.1016/S1369-7021(07)70275-4.
- [97] A. Zacharopoulos et al. "Linear Dielectric Non-Imaging Concentrating Covers For PV Integrated Building Facades". In: *Solar Energy* 68.5 (Jan. 2000), pp. 439–452. ISSN: 0038092X. DOI: 10.1016/S0038-092X(00)00013-X.
- [98] Tapas K. Mallick, Philip C. Eames, and Brian Norton. "Non-concentrating and asymmetric compound parabolic concentrating building facade integrated photovoltaics: An experimental comparison". In: *Solar Energy* 80.7 (July 2006), pp. 834–849. ISSN: 0038092X. DOI: 10.1016/j.solener.2005.05.011.
- [99] T Mallick and P Eames. "Design and fabrication of low concentrating second generation PRIDE concentrator". In: *Solar Energy Materials and Solar Cells* 91.7 (Apr. 2007), pp. 597–608. ISSN: 09270248. DOI: 10.1016/j.solmat.2006.11.016.
- [100] Omer Korech et al. "Dielectric microconcentrators for efficiency enhancement in concentrator solar cells." In: *Optics letters* 32.19 (Oct. 2007), pp. 2789–91. ISSN: 0146-9592.
- [101] Minkyu Park et al. "A tapered dielectric waveguide solar concentrator for a compound semiconductor photovoltaic cell." In: *Optics express* 18.2 (Jan. 2010), pp. 1777–87. ISSN: 1094-4087.

Bibliography

- [102] Roland Winston and Weiya Zhang. "Pushing concentration of stationary solar concentrators to the limit." In: *Optics express* 18.9 (Apr. 2010), A64–72. ISSN: 1094-4087.
- [103] Antoni G. Molledo and Anonio Luque. "Analysis of static and quasi-static cross compound parabolic concentrators." In: *Applied optics* 23.12 (June 1984), p. 2007. ISSN: 0003-6935.
- [104] J O'Gallagher. *Non Imaging Optics in Solar Energy*. 2008. ISBN: 9781598293302.
- [105] R. Winston and H. Hinterberger. "Principles of cylindrical concentrators for solar energy". In: *Solar Energy* 17.4 (Sept. 1975), pp. 255–258. ISSN: 0038092X. DOI: 10.1016/0038-092X(75)90007-9.
- [106] M Rönnelid and B Karlsson. "Optical acceptance function of modified compound parabolic concentrators with linear corrugated reflectors." In: *Applied optics* 37.22 (Aug. 1998), pp. 5222–6. ISSN: 0003-6935.
- [107] P Ortega et al. "Advances in a baseline process towards high efficiency c-Si solar cell fabrication". In: 00.C (2009), pp. 349–352.
- [108] Jongseung Yoon et al. "Ultrathin silicon solar microcells for semitransparent, mechanically flexible and microconcentrator module designs." In: *Nature materials* 7.11 (Nov. 2008), pp. 907–15. ISSN: 1476-1122. DOI: 10.1038/nmat2287.
- [109] Andreas Gombert et al. "A rigorous study of diffraction effects on the transmission of linear dielectric micro-reflector arrays". In: *Journal of Optics A: Pure and Applied Optics* 6.10 (Oct. 2004), pp. 952–960. ISSN: 1464-4258. DOI: 10.1088/1464-4258/6/10/005.
- [110] Florian Schneider et al. "Process and material properties of polydimethylsiloxane (PDMS) for Optical MEMS". In: *Sensors and Actuators A: Physical* 151.2 (Apr. 2009), pp. 95–99. ISSN: 09244247. DOI: 10.1016/j.sna.2009.01.026.
- [111] A. Parretta et al. "Inverse illumination method for characterization of CPC concentrators". In: *Proceedings of SPIE* 6652 (2007), ISSN: 0277786X. DOI: 10.1117/12.733605.

Acknowledgements

I would like to thank Professor Hans Peter Herzig for all the generous support and for giving me the opportunity to do my PhD studies with his group at the Optics & Photonics Technology Lab.

I would like to thank my co-director and advisor Dr. Toralf Scharf for the many hours passed on discussing the progress of my thesis (or lack thereof). I was always leaving our meetings with fresh ideas and a clear vision of how to tackle the issues at hand.

I would like to thank SUSS MicroOptics for the fruitful collaboration, the funding of the project and the scientific freedom they provided.

I would like to thank the Swiss Commission for Technology and Innovation for the project funding.

I would like to thank Professor Nico de Rooij who generously allowed me to pass most of my PhD studies as a guest and unofficial member of the Sensor and Actuator Lab (SAMLAB) and benefit from all the first class infrastructure.

I also thank Dr. Willfried Noell for integrating me into the MOEMS group and for all the support and the many FRED discussions we had.

I would like to thank all the members of the MOEMS group Caglar Ataman, Dara Bayat, Michael Canonica, Nicolas Golay, Fabio Jutzi, Sebastian Lani, Jonathan Masson, Yves Petremand, Michael Zickar, Severin Waldis and Stefan Weber for all the interesting group meetings and all the fun we had together.

I would like to thank all the other members of SAMLAB and LMTS lab for the wonderful time we passed together.

A special thank you goes to Claudio Novelli that always tried to accommodate my particular wishes when it comes to computers and for the reliable back up system that saved me several times.

I would like to thank Karin Frossard for making our life at SAMLAB easy and smooth.

Acknowledgements

I would like to thank my colleagues at the OPT Lab for having accepted me as the mostly absent member.

I would like to thank the clean room staff at ComLab CSEM where most of the fabrication.

I would like to thank Irène Phillipoussis Fernandez for her help with the micro fabrication and Marcel Groccia for the electronics.

I would like to thank my family, my brother Sebastian and Marieflore that sacrificed many weekends looking after Zuzanna so we could write.

I thank my mother and my father that were always there to help, no matter what. Without you, this thesis would not have been possible.

I would like to thank my wife Joanna that underwent the same adventure of writing her own thesis at the same time as me and my daughter Zuzanna that had to live for quite a moment with a rather absent minded and preoccupied dad.

Neuchâtel, August 3rd 2012

R. B.

List of publications

Publications related to the thesis

R. Bitterli, T. Scharf, H.-P. Herzig, W. Noell, N.F. de Rooij, A. Bich, S. Roth, K. J. Weible, R. Voelkel, M. Zimmermann, M. Schmidt, *Fabrication and characterization of linear diffusers based on concave micro lens arrays*, Opt. Express 18, 14251-14261 (2010)

R. Bitterli, M. Kim, T. Scharf and H.-P. Herzig *Fabrication and Characterization of 1-D diffusing elements* 15th Microoptics Conference (MOC), Tokyo, Japan, October 2009.

R. Bitterli, M. Kim, T. Scharf, H.-P. Herzig, A. Bich, C. Dumouchel, S. Roth, R. Völkel, K. J. Weible, *Refractive statistical concave 1D diffusers for laser beam shaping*, Proc. SPIE 7062, 70620P (2008)

R. Bitterli, M. Kim, T. Scharf, H.-P. Herzig, A. Bich, C. Dumouchel, S. Roth, R. Völkel, K. J. Weible, *Fabrication Rules and Characterization of Concave Microstructures in Fused Silica*, EOS Annual Meeting, Paris, September 2008

R. Bitterli, T. Scharf, H.-P. Herzig, A. Bich, C. Dumouchel, S. Roth, R. Völkel, K. J. Weible, *One dimensional diffuser for high power beam shaping*, Deutsche Gesellschaft für angewandte Optik, Jahrestagung, Esslingen Germany, May 2008

R. Bitterli, T. Scharf, H.-P. Herzig, A. Bich, C. Dumouchel, S. Roth, R. Völkel, K. J. Weible, *Linear diffusers with ultra small angles for high power beam shaping*, Laser Optics Berlin, Berlin, March 2008

J. Masson, R. Bitterli, W. Noell, N.F. de Rooij, A. Bich, K. J. Weible, R. Voelkel, *Dynamically deformable micromirror array for defined laser beam shaping and homogenizing*, Optical MEMS and Nanophotonics (OMN), 2011 International Conference, pp.3-4, August 2011

W. Noell, S. Weber, J. Masson, J. Extermann, L. Bonacina, A. Bich, R. Bitterli, H.-P. Herzig, D. Kiselev, T. Scharf, R. Voelkel, K.J. Weible, J.P. Wolf, N.F. de Rooij, *Shaping Light with MOEMS*, Proc. of SPIE 7930, 79300P (2011)

J. Masson, A. Bich, H. P. Herzig, R. Bitterli, W. Noell, T. Scharf, R. Voelkel, K. J. Weible, N. F. de Rooij, *Deformable silicon membrane for dynamic linear laser beam diffuser*, Proc. SPIE 7594,

Acknowledgements

75940F (2010)

A. Bich, K.J. Weible, R. Voelkel, M. Zimmermann, I. Harder, N. Lindlein, J. Masson, R. Bitterli, W. Noell, T. Scharf, *Dynamic array spot shaping for laser micro machining*, Laser Beam Shaping X, San Diego, August 2009.

A. Bich, J. Rieck, C. Dumouchel, S. Roth, K. J. Weible, M. Eisner, R. Voelkel, M. Zimmermann, M. Rank, M. Schmidt, R. Bitterli, N. Ramanan, P. Ruffieux, T. Scharf, W. Noell, H.-P. Herzig, N.F. de Rooij, *Multifunctional Micro-Optical Elements for Laser Beam Homogenizing and Beam Shaping*, Proc. of SPIE 6879, 68790Q-1 (2008)

K. J. Weible, A. Bich, S. Roth, C. Dumouchel, P. Pernet, M. Eisner, R. Völkel, R. Bitterli, T. Scharf, W. Noell, *Randomly varying micro-optical elements for the generation of uniform intensity profiles in coherent laser sources*, Laser Beam Shaping IX (Proceedings Volume) (2008)

Publications not related to the thesis

J. Charmet, H. Haquette, E. Laux, G. Gorodyska, M. Textor, G. Spinola Durante, E. Portuondo-Campa, H. Knapp, R. Bitterli, W. Noell, H. Keppner, *Liquid as template for next generation micro devices*, Journal of Physics: Conference Series, Volume 182, Issue 1, pp. 012021 (2009)

A.P. Han, G. Schurmann, G. Mondin, R. Bitterli, N.G. Hegelbach, N.F. de Rooij, U. Staufer, *Sensing protein molecules using nanofabricated pores*, APPLIED PHYSICS LETTERS Volume: 88 Issue: 9 Article Number: 093901 (2006)

Patents

R. Bitterli, W. Noell, F. Blondeau, L. Paratte, T. Scharf, P.A. Meister, A. Zanetta, *Assembly element including fork shaped elastic structures and timepiece including the same*, ETA Manufacture Horlogere Suisse (2008)

R. Bitterli, W. Noell, F. Blondeau, L. Paratte, T. Scharf, P.A. Meister, A. Zanetta, *Assembly element including two series of elastic structures and timepiece fitted with the same*, ETA Manufacture Horlogere Suisse (2008)

R. Bitterli, W. Noell, F. Blondeau, L. Paratte, T. Scharf, P.A. Meister, A. Zanetta, *Assembly element including two superposed strip shaped elastic structures and timepiece fitted with the same*, ETA Manufacture Horlogere Suisse (2008)

Curriculum Vitae

Roland Bitterli

Born 19.05.1980 in Lausen, Switzerland

Swiss citizenship

Education

- | | |
|-----------|--|
| 2006-2012 | PhD in micro optics
Optics & Photonics Technology Laboratory
École Polytechnique Fédérale de Lausanne, Switzerland |
| 2004-2006 | MSc in micro and nano technology
Université de Neuchâtel, Switzerland |
| 2001-2004 | BSc in micro and nano science
Université de Neuchâtel |

Past positions

- | | |
|-----------------|--|
| 06.2001-09.2001 | Application programmer
Interpro GmbH
4144 Arlesheim, Switzerland |
|-----------------|--|

Qualifications

Design of micro optical systems, simulation of optical systems (ray tracing), simulation of mechanical properties (FEM), micro fabrication of glass, silicon and polymers, photo mask design, programming in matlab, Python, Basic

Languages

- | | |
|---------|---------------|
| German | native tongue |
| French | fluent |
| English | fluent |